

SEARCH FOR CHARGINO AND NEUTRALINO  
AT  
RUNII OF THE TEVATRON COLLIDER

A Preliminary Report  
Submitted to the Faculty  
of  
Purdue University  
by  
Anadi Canepa

In Partial Fulfillment of the  
Requirements for the Degree  
of  
Doctor of Philosophy

January 2004

# TABLE OF CONTENTS

	Page
LIST OF TABLES . . . . .	v
LIST OF FIGURES . . . . .	vi
ABSTRACT . . . . .	ix
1 A look to the Standard Model . . . . .	1
1.1 The SM particle content . . . . .	1
1.2 The SM interactions . . . . .	2
1.3 EW Symmetry breaking . . . . .	4
1.4 Why beyond the SM . . . . .	6
2 SuperSymmetry . . . . .	11
2.1 Why do we choose Supersymmetry as a theory beyond the SM? . . .	11
2.2 A supersymmetric theory . . . . .	12
2.2.1 Chiral superfield . . . . .	15
2.2.2 Vector superfields . . . . .	16
2.3 Supersymmetric lagrangian . . . . .	16
2.3.1 Kinetic contributions for the free <i>superfields</i> . . . . .	17
2.3.2 Interaction terms . . . . .	18
2.3.3 The gauge terms . . . . .	18
2.3.4 The Globally Supersymmetric Lagrangian . . . . .	19
2.3.5 Symmetry Breaking . . . . .	20
3 Minimal Supersymmetric Standard Model . . . . .	23
3.1 Particle content . . . . .	23
3.1.1 Chiral content . . . . .	23
3.1.2 Gauge content . . . . .	25
3.2 Superpotential . . . . .	25

	Page
3.3 EW breaking in the contest of the MSSM . . . . .	26
3.3.1 Mass eigenstates in the contest of MSSM . . . . .	28
3.4 Supersymmetry breaking in the contest of the MSSM . . . . .	29
3.5 Minimal SUPERGRAVITY . . . . .	30
4 The Experiment . . . . .	33
4.1 The Fermilab Tevatron . . . . .	33
4.1.1 Production of Protons and Boosting . . . . .	35
4.1.2 The Main Injector . . . . .	36
4.1.3 Antiproton Production and Cooling . . . . .	37
4.1.4 The Tevatron . . . . .	38
4.2 The Collider Detector at Fermilab . . . . .	38
4.2.1 The Central Tracking System . . . . .	40
4.2.2 The Time of Flight Detector . . . . .	47
4.2.3 The Calorimetry System . . . . .	49
4.2.4 Muon Detection . . . . .	52
4.2.5 The Trigger and Data Acquisition System . . . . .	53
5 SUSY Signature and Current limits . . . . .	57
5.1 Current Limit . . . . .	57
5.2 Signature of the event . . . . .	60
6 Investigation of the parameter space . . . . .	65
7 Trilepton Sensitivity at Tevatron Run II . . . . .	81
7.1 Low energy constraints . . . . .	81
7.2 Collider phenomenology . . . . .	82
8 Conclusion . . . . .	91
9 AppendixA . . . . .	93
9.1 Scan: $A_0=0$ $\mu > 0$ . . . . .	93
10 AppendixB . . . . .	99
10.1 Scan: $A_0=250$ $\mu > 0$ . . . . .	99

LIST OF REFERENCES . . . . .	105
------------------------------	-----

# LIST OF TABLES

Table		Page
1.1	Gauge transformations of the SM particles; the symbols $\alpha$ , $\beta$ and $\gamma$ stay for the infinitesimal parameters; $L_{l,q}$ ( $R_{l,q}$ ) indicates the left (right) handed lepton or quark. . . . .	3
3.1	Chiral multiplets in the MSSM . . . . .	24
3.2	Vector multiplets in the MSSM . . . . .	25
4.1	Resolution on various track parameters as obtained by the COT and by the COT + SVXII + ISL. . . . .	46
4.2	Characteristic of the CDF II calorimeter. . . . .	50

# LIST OF FIGURES

Figure	Page
1.1 Schematic view of the Higgs potential with $\mu^2 < 0$ and $\lambda > 0$ . . . . .	5
1.2 Scalar, fermion and vector boson loop corrections to the Higgs mass. . . . .	7
2.1 Running of gauge coupling constants in the SM and in the SUSY framework . . . . .	13
4.1 A schematic drawing of the Fermilab accelerator complex. . . . .	34
4.2 Average number of interactions per bunch crossing as a function of the instantaneous luminosity for different beam conditions. . . . .	36
4.3 Schematic diagram which illustrates the antiproton production and selection chain. . . . .	37
4.4 CDF Run II detector view. . . . .	39
4.5 CDF Run II detector view. . . . .	39
4.6 Longitudinal view of half of the CDF Run II detector. . . . .	40
4.7 Schematic drawing of the $r - z$ section of the CDF Run II detector. . . . .	41
4.8 Schematic $r - \phi$ (left) and $r - z$ (right) views the Run II CDF silicon detector. . . . .	44
4.9 . . . . .	45
4.10 Intermediate Silicon Layer . . . . .	45
4.11 Perspective view of a CEM module. . . . .	48
4.12 $r - z$ view of the plug calorimeter (left), and the SMD module (right). . . . .	52
4.13 CDF pipelines and buffers trigger architecture (left). Block diagram of the Run II trigger system. . . . .	53
5.1 X.Tata, hep-ph/9706307: Total cross section for various <i>sparticle</i> production processes by $p\bar{p}$ collisions at $\sqrt{s} = 2$ TeV . . . . .	58
5.2 LEP-SUSY working group:lower limit on the lightest neutralino mass . . . . .	60
5.3 LEP-SUSY working group:excluded region in the $m_0$ - $m_{\frac{1}{2}}$ planes for fixed $\tan\beta \operatorname{sgn}\mu$ and $A_0$ . . . . .	61

Figure	Page
5.4 Chargino-Neutralino associated production at $p\bar{p}$ collider . . . . .	61
6.1 ISAJET: $\tilde{\chi}_1^\pm, \tilde{\chi}_2^0$ and SM Higgs mass vs $m_{\frac{1}{2}}$ . . . . .	66
6.2 ISAJET: <i>sleptons</i> mass vs $m_{\frac{1}{2}}$ . . . . .	67
6.3 ISAJET: <i>sneutrinos</i> mass vs $m_{\frac{1}{2}}$ . . . . .	67
6.4 PYTHIA: <i>sneutrinos</i> mass vs $m_{\frac{1}{2}}$ . . . . .	68
6.5 ISAJET: Production cross sections at $E_{CDM} = 2$ TeV . . . . .	69
6.6 ISAJET: Production cross sections at $E_{CDM} = 2$ TeV . . . . .	69
6.7 ISAJET: Decay channel $\tilde{\chi}_1^\pm \rightarrow \tilde{\tau}_1 \nu_\tau$ . . . . .	70
6.8 ISAJET: Decay channel $\tilde{\chi}_1^\pm \rightarrow f \bar{f}' \tilde{\chi}_1^0$ . . . . .	70
6.9 ISAJET: Decay channel $\tilde{\chi}_1^\pm \rightarrow W \tilde{\chi}_1^0$ . . . . .	71
6.10 ISAJET: Decay channel $\tilde{\chi}_1^\pm \rightarrow l \tilde{\nu}_l$ . . . . .	72
6.11 PYTHIA: Decay channel $\tilde{\chi}_1^\pm \rightarrow l \tilde{\nu}_l$ . . . . .	72
6.12 ISAJET: Decay channel $\tilde{\chi}_2^0 \rightarrow \tilde{\tau}_1 \tau$ . . . . .	73
6.13 ISAJET: Decay channel $\tilde{\chi}_2^0 \rightarrow l \tilde{l}$ . . . . .	73
6.14 ISAJET: Decay channel $\tilde{\chi}_2^0 \rightarrow ll \tilde{\chi}_1^0$ . . . . .	74
6.15 ISAJET: Decay channel $\tilde{\chi}_2^0 \rightarrow W \tilde{\chi}_1^0$ . . . . .	74
6.16 ISAJET: Decay channel $\tilde{\chi}_2^0 \rightarrow \nu \tilde{\nu}$ . . . . .	75
6.17 ISAJET: Decay channel $\tilde{\nu} \rightarrow \nu \tilde{\chi}_1^0$ . . . . .	76
6.18 ISAJET: Effective production Cross section at $\sqrt{s} = 2$ Gev . . . . .	77
6.19 ISAJET: Effective production Cross section $\sqrt{s} = 2$ Gev . . . . .	77
6.20 ISAJET: Number of generated trilepton events $\sqrt{s} = 2$ Gev for 500 pb <sup>-1</sup> . . . . .	78
6.21 ISAJET: Number of generated lepton-ditau events $\sqrt{s} = 2$ Gev for 500 pb <sup>-1</sup> . . . . .	78
6.22 ISAJET: Number of generated dilepton-tau events $\sqrt{s} = 2$ Gev for 500 pb <sup>-1</sup> . . . . .	79
6.23 ISAJET: Number of generated tritau events $\sqrt{s} = 2$ Gev for 500 pb <sup>-1</sup>	79
7.1 $A_0 = 0, \mu > 0, \tan\beta = 10$ . . . . .	84
7.2 $A_0 = 0, \mu > 0, \tan\beta = 30$ . . . . .	85

7.3	J.Ellis <i>et al.</i> , hep-ph/0303043; The strips display the regions of the $m_0$ - $m_{\frac{1}{2}}$ plane that are compatible with the $0.094 < \Omega_\chi h^2 < 0.129$ and the laboratory constraints for $\mu > 0$ and different values of $\tan\beta$ . . .	87
7.4	H.Baer <i>et al.</i> , hep-ph/0304303; reach of LHC assuming 100 fb <sup>-1</sup> of integrated luminosity and excluded regions . . . . .	88
7.5	H.Baer <i>et al.</i> , hep-ph/0304303; reach of LHC assuming 100 fb <sup>-1</sup> of integrated luminosity and excluded regions . . . . .	88
7.6	$A_0 = 0, \mu > 0, \tan\beta = 30$ . . . . .	90
9.1	$A_0 = 0, \mu > 0, \tan\beta = 10$ . . . . .	93
9.2	$A_0 = 0, \mu > 0, \tan\beta = 10$ . . . . .	94
9.3	$A_0 = 0, \mu > 0, \tan\beta = 30$ . . . . .	95
9.4	$A_0 = 0, \mu > 0, \tan\beta = 30$ . . . . .	96
9.5	$A_0 = 0, \mu > 0, \tan\beta = 50$ . . . . .	97
9.6	$A_0 = 0, \mu > 0, \tan\beta = 50$ . . . . .	98
10.1	$A_0 = 20, \mu > 0, \tan\beta = 10$ . . . . .	99
10.2	$A_0 = 20, \mu > 0, \tan\beta = 10$ . . . . .	100
10.3	$A_0 = 20, \mu > 0, \tan\beta = 30$ . . . . .	101
10.4	$A_0 = 20, \mu > 0, \tan\beta = 30$ . . . . .	102
10.5	$A_0 = 20, \mu > 0, \tan\beta = 50$ . . . . .	103
10.6	$A_0 = 20, \mu > 0, \tan\beta = 50$ . . . . .	104



## ABSTRACT

Canepa, Anadi. Ph.D., Purdue University, January, 2004. Search for Chargino and Neutralino at RUNII of the Tevatron Collider. Major Professor: D.Bortoletto.

One of the most promising signature for SUSY search at a hadron collider is the 'jet clean' trilepton channel deriving from the associated production of chargino and neutralino. This event topology is chosen here to assess the sensitivity for SUSY matter at the current Run II of the Tevatron. A detail analysis of the parameter space in the mSUGRA scenario will be performed to map out the regions at highest sensitivity. The results will be then compared to the collider and low energy constraints and to the range favoured by the new WMAP data.



# 1. A look to the Standard Model

In the '70 the Standard Model (SM) for particle physics emerged: it is a non abelian gauge theory, based on the gauge group  $SU(3)_C \times SU(2)_L \times U(1)_Y$ , which describes the properties and the interactions of fundamental particles. It includes the electromagnetic EM, the weak and the strong interactions. It is further assumed that the  $SU(2)_L \times U(1)_Y$  symmetry is spontaneously broken to provide particles with mass. All confirmed experimental data completely agree with the predictions of this model but there are still unanswered questions that stimulate the search for physics beyond. The Standard Model is briefly reviewed here as an introduction to the MSSM: the Minimal Supersymmetric Standard Model, one of the most promising extension of the SM.

## 1.1 The SM particle content

The particle content of the SM can be separated into matter and gauge sector. The matter sector includes spin  $\frac{1}{2}$  particles, grouped into 3 lepton and 3 quark generations, distinguished by the mass scale of the particles they contain:

$$1^{\text{st}} \text{ family : } L_e = \begin{pmatrix} \nu_e \\ e \end{pmatrix}_L, R_e = e_R, L_u = \begin{pmatrix} u \\ d' \end{pmatrix}_L, R_u = u_R, R_d = d_R \quad (1.1)$$

$$2^{\text{nd}} \text{ family : } L_\mu = \begin{pmatrix} \nu_\mu \\ \mu \end{pmatrix}_L, R_\mu = \mu_R, L_c = \begin{pmatrix} c \\ s' \end{pmatrix}_L, R_c = c_R, R_s = s_R \quad (1.2)$$

$$3^{\text{rd}} \text{ family : } L_\tau = \begin{pmatrix} \nu_\tau \\ \tau \end{pmatrix}_L, R_\tau = \tau_R, L_t = \begin{pmatrix} t \\ b' \end{pmatrix}_L, R_t = t_R, R_b = b_R. \quad (1.3)$$

where  $d'_i = \sum_j V_{ij} d_j$  and  $V_{ij}$  stands for the Cabibbo-Kobayashi-Maskawa matrix. As mentioned later (Tab. 1.1) leptons are only subjected to the EM and weak interactions, whereas quarks to the strong only. The other ingredient of the SM matter sector is a complex spin-0  $SU(2)$  doublet, the so called Higgs field, which is responsible for the particles mass:

$$\phi = \begin{pmatrix} \varphi^+ \\ \varphi^- \end{pmatrix} \quad (1.4)$$

Each interaction is associated to a carrier which mediates the interaction between the matter fields; the so called gauge sector contains spin-1 particles identified as the carriers:

- the gluons  $B_\mu^A$  (with  $A=1,\dots,8$ ), associated to the strong interaction and characterized by the coupling constant  $\alpha_S$
- the bosons  $b_\mu^a$  (with  $a=1,2,3$ ) and  $A_\mu$ , associated to the electroweak interaction with the coupling constants  $g$  and  $g'$

The mass eigenstates of the electroweak bosons will be the photon  $\gamma$  and the boson  $W^\pm$  and  $Z^0$ .

## 1.2 The SM interactions

Relativistic quantum field theories are described by a Lagrangian  $\mathcal{L}(\phi, \partial_\mu \phi)$  which contains all information about the interactions and the properties of the fields considered. In the SM, the gauge invariance of the SM Lagrangian under  $SU(3)_C \times SU(2)_L \times U(1)_Y$  completely determines the interactions between fermions and gauge bosons and the self interactions of the gauge bosons themselves, as follows. The local invariance is claimed: namely, the derivative of the fermions field (matter field) is replaced by the covariant derivative which contains the fermion-gauge boson interaction vertexes; therefore free terms for the gauge fields just introduced (in one

to one correspondance with the group generator) have to be added to the Lagrangian. The free terms include the cubic and quartic self interaction (Yang-Mills contribution). The covariant derivative can be written as:

$$D_\mu = \partial_\mu - i\alpha_S B_\mu^A \lambda^A - ig b_\mu^a \frac{\tau^a}{2} - ig' A_\mu Y \quad (1.5)$$

where the symbols  $Y$ ,  $\frac{\tau^a}{2}$  and  $\lambda^A$  stand for the generators of the transformations  $U(1)_Y$ ,  $SU(2)_L$  and  $SU(3)_C$ . As indicated in Tab.1.1, both right and left handed fermions transform as singlet under  $U(1)_Y$ , whereas the behavior depends on the handness in the case of  $SU(2)_L$  transformations: indeed right handed fermions are  $SU(2)_L$  singlets while left handed are  $SU(2)_L$  doublets. For what concerns  $SU(3)_C$  transformations, these only act on quarks meaning that quarks form  $SU(3)_C$  triplets. The Yang-Mill SM Lagrangian can be written as the addition of the fermion-gauge

$U(1)_Y$	$L_{l,q} \rightarrow (1 - ig'Y\alpha(x))L_{l,q}$
	$R_{l,q} \rightarrow (1 - ig'Y\alpha(x))R_{l,q}$
$SU(2)_L$	$L_{l,q} \rightarrow (1 - \frac{1}{2}ig\vec{\tau}\vec{\beta}(x))L_{l,q}$
	$R_{l,q} \rightarrow R_{l,q}$
$SU(3)_C$	$L_l \rightarrow L_l$
	$R_l \rightarrow R_l$
	$L_q \rightarrow (1 - i\alpha_s\vec{\lambda}\vec{\gamma}(x))L_q$
	$R_q \rightarrow (1 - i\alpha_s\vec{\lambda}\vec{\gamma}(x))R_q$

Table 1.1

Gauge transformations of the SM particles; the symbols  $\alpha$ ,  $\beta$  and  $\gamma$  stay for the infinitesimal parameters;  $L_{l,q}$  ( $R_{l,q}$ ) indicates the left (right) handed lepton or quark.

boson interaction term  $\mathcal{L}_F$  and the free gauge fields components  $\mathcal{L}_{YM}$ :

$$\mathcal{L} = \mathcal{L}_F + \mathcal{L}_{YM} = i\bar{\Psi}\gamma^\mu D_\mu \Psi - \frac{1}{4}B_A^{\mu\nu}B_{\mu\nu}^A - \frac{1}{4}b_a^{\mu\nu}b_{\mu\nu}^a - \frac{1}{4}F^{\mu\nu}F_{\mu\nu} \quad (1.6)$$

with

- $B_{\mu\nu}^A = \partial_\mu B_\nu^A - \partial_\nu B_\mu^A + g_S f_{ABC} B_\mu^B B_\nu^C$  for the strong interaction
- $b_{\mu\nu}^a = \partial_\mu b_\nu^a - \partial_\nu b_\mu^a + g f_{ajk} b_\mu^j b_\nu^k$  for the weak interaction
- $F_{\mu\nu} = \partial_\mu A_\nu - \partial_\nu A_\mu$  for the electromagnetic interaction

where  $f_{ABC}$  and  $f_{ajk}$  are the structure constants for  $SU(3)$  and  $SU(2)$ , and  $\Psi$  is a fermionic field. The bilinear term in the EM kinetic energy disappears since the self interaction of the vector fields (photon) is not allowed.

### 1.3 EW Symmetry breaking

The symmetry  $SU(2)_L \times U(1)_Y$  is known to be broken to the observed  $U(1)_Q$  symmetry since the gauge bosons and the fermions (but neutrinos) are massive particles; only those gauge fields that correspond to an unbroken symmetry will remain massless. Under  $SU(2)_L$ , the fermionic left and the right components behave differently. This means that the two chiral components cannot interact with each other and mass term for fermions, such as  $\bar{\Psi}_L \Psi_R$ , are forbidden. To give mass to the fermions and to the gauge bosons, the EW theory is realized with a vacuum state invariant under  $U(1)_Q$ . This allows the introduction of mass terms for the fermions also. The mechanism by which starting from a degenerate vacuum state, mass terms are constructed is known as the Higgs mechanism. The basic idea is to introduce a new scalar field (the Higgs field) whose Lagrangian is instrumental to the symmetry breaking. The most general Lagrangian for a scalar field is:

$$\mathcal{L} = (D_\mu \phi)^\dagger (D_\mu \phi) - V \quad (1.7)$$

$$V = \mu^2 \phi^\dagger \phi + \lambda (\phi^\dagger \phi)^2 \quad (1.8)$$

where  $\lambda$  represents the coupling of the four-boson vertex. This Lagrangian is invariant under  $SU(2)_L \times U(1)_Y$  and it can be added to the EW SM Lagrangian. To have a vacuum state (minimum of potential) degenerate,  $\mu^2$  should be  $<0$  whereas the coefficient  $\lambda > 0$  to guarantee the potential to be bounded from below (Fig.1.1).

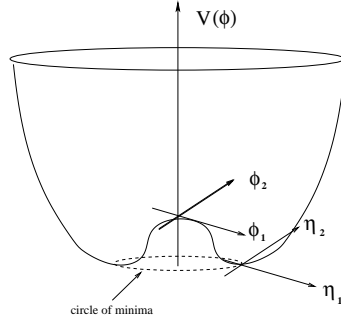


Figure 1.1. Schematic view of the Higgs potential with  $\mu^2 < 0$  and  $\lambda > 0$

The field  $\phi$  can be expanded about one of the ground states; in choosing a particular ground state, Eq.(1.9), the symmetry is broken:

$$\langle \phi \rangle = \frac{1}{\sqrt{2}} \begin{pmatrix} 0 \\ v \end{pmatrix} \quad (1.9)$$

$$v = \sqrt{\frac{-\mu^2}{\lambda}} \quad (1.10)$$

The favoured solution acquires a non zero vacuum expectation value  $VEV = v$ . The mass terms for the gauge bosons come from the kinetic part of the Higgs Lagrangian once it is expanded around the vacuum. When rearranged into appropriate linear combinations, the gauge bosons acquire mass, corresponding to the eigenstates  $W^\pm$  and  $Z^0$ :

$$m_W^2 = \frac{g^2 v^2}{4} \quad m_Z^2 = \frac{(g^2 + g'^2) v^2}{4} \quad (1.11)$$

while  $\gamma$  remains massless. Starting from the same doublet, which gives masses to the gauge bosons it is possible to introduce mass terms for the fermion fields. These

impose constraints on the Higgs field: to get fermionic term of the form  $-\bar{\Psi}_L \Gamma \Psi_R \phi$ , the Higgs field should have isospin equal  $\frac{1}{2}$ . If this requirement is satisfied, then the so called Yukawa terms:

$$\mathcal{L}_{Yukawa} = - \left( \lambda_u \bar{R}_u \bar{\phi}^\dagger \cdot L_u + \lambda_d \bar{R}_d \phi^\dagger \cdot L_u + \lambda_e \bar{R}_e \phi^\dagger \cdot L_e + \text{h.c.} \right), \quad (1.12)$$

provide the vertex for the interaction of fermions and Higgs boson as well as the fermion mass by expansion around  $VEV$ . The constants  $\lambda_u$ ,  $\lambda_d$  and  $\lambda_e$  are the Yukawa coupling constants. In the particular case of electron, the Yukawa contribution can be rewritten as:

$$\mathcal{L}_{Yukawa}^{electron} = -m_e \bar{\psi}_e \psi_e - \frac{\lambda_e}{\sqrt{2}} H \bar{\psi}_e \psi_e, \quad (1.13)$$

From measurements of the the properties of the weak interactions,  $v = 250$  GeV implying a mass  $M_H^2 \sim (-100 \text{ GeV})^2$ . All particles owe their mass to the Higgs boson, therefore the entire spectrum of the SM is directly or indirectly sensitive to the value of its mass.

#### 1.4 Why beyond the SM

The HEP experiments have explored an energy range up to TeV and the SM has been proven to be extremely successfully since no deviations from its predictions have been observed; currently, hadronic colliders are searching for the last ingredient of such a model, the Higgs boson which has escaped detection so far. Nevertheless, it is striking that the SM is regarded as the low energy effective theory of a more fundamental theory since there are several issues that are not resolved in the SM. The major of these concerns the extension of its validity up to the Planck mass ( $\sim 2.4 \cdot 10^{18}$ ) GeV/c<sup>2</sup>. Actually, the SM does not include the gravity and the Planck energy is indeed one of the candidate for a fundamental mass scale where gravity becomes as strong as the other interactions. This point raises further questions, the so called *hierarchy* and *naturalness* problems. Why is the weak scale so much smaller than the Planck scale? Besides, attempts have been made to unify the electroweak



and the strong interactions in a new symmetry (Grand Unification Theory or GUT) which might manifest at high energy (the GUT scale is believed to be  $\sim 10^{16} \text{GeV}/c^2$ ); the question now is why the EW is also lower than the GUT scale? This is referred to as *hierachy* problem. But the crucial question is the *naturalness* problem. The SM doesn't provide any explanation to the low value of the EW scale that is, in turn, fixed by the VEV of the Higgs boson. Actually, as for all spin 0 particle in the SM, the Higgs boson mass receives quantum corrections that increase quadratically with an energy cutoff  $\Lambda$ :

$$\delta m_H^2 = \mathcal{O}\left(\frac{g^2}{16\pi^2}\right) \int^\Lambda d^4k \frac{1}{k^2} = \mathcal{O}\left(\frac{\alpha}{\pi}\right) \Lambda^2 \quad (1.14)$$

where the cutoff represents the scale up to which the SM remains valid. This holds for each of the one-loop diagram in Fig.(1.2).

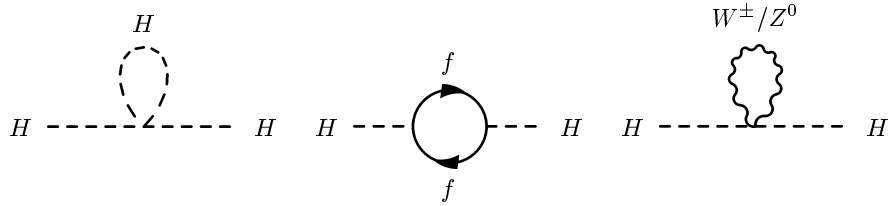


Figure 1.2. Scalar, fermion and vector boson loop corrections to the Higgs mass.

If the cutoff is chosen to be  $\Lambda \approx M_P$ , the radiative corrections to the Higgs boson mass can be 30 order of magnitude larger than the physical value of  $m_H^2$ . If the SM is therefore the correct theory to the Planck scale, this would require a “fine tuning” to make it possible for the physical mass to belong to the predicted range. On the other hand, to constraint the Higgs mass in a range suitable to the EW measurements, it is necessary to claim the SM valid up to a maximum energy of 1 TeV; therefore, new physics might appear at  $E > 1 \text{ TeV}$ . It has to be remarked that the instability of the mass to radiative corrections is endemic to spin-0 fields; chiral and gauge symmetries protect fermions and gauge bosons from large corrections. For

instance, in the case of a fermion, the corrections are just logarithmically divergent in  $\Lambda$  and proportional to the mass:

$$\delta m_f = \mathcal{O}\left(\frac{g^2}{16\pi^2}\right) \int^\Lambda d^4k \frac{1}{k^2} = \mathcal{O}\left(\frac{\alpha}{\pi}\right) m_f \ln\left(\frac{\Lambda}{m_f}\right) \quad (1.15)$$

Massless fermions therefore remain massless due to the chiral symmetry likewise the photon does not acquire mass thanks to the gauge symmetry. Nevertheless, the masses are generated by the Higgs mechanism, so a  $\text{VEV} \neq 250 \text{ GeV}$  would affect the whole spectrum.

The SM shows other theoretically unsatisfactory aspects that can be grouped as follows:

- **quantum number assignment:** the quantum numbers of the fermions are associated to under  $SU(3)_C \times SU(2)_L \times U(1)_Y$  are crucial for the gauge invariance but are not explained in the SM;
- **number of parameters:** the SM contains at least 19 free parameters (3 gauge coupling constants, 6 quark and 3 lepton masses; 3 weak mixing angles and 1 CP violating phase; 2 parameters for the Higgs sector ( $\lambda, \mu$ ), 1 CP violating vacuum angle  $\theta_3$ ); this fact highlight the SM as an effective theory;
- **masses:** the mass generation mechanism is still unknown: do they really originate from a Higgs boson? why do the fermions have a mass spectrum stretched over six order of magnitude from the electron to the top quark? Is there any other physics involved?
- **flavour content:** there is no explanation to the repetition of generations: what's the origin of the six flavours for quarks and leptons?
- **unification:** there is no unification of the interactions into a single gauge group: can all interactions be unified and all the coupling constants related to each other? Can gravity be included?

The most striking experimental result that cries out for the overcoming of the SM is the recent evidence of neutrino oscillations. All the issues just raised claim for a more fundamental theory: the supersymmetric model is one of the most promising extension of the SM as described in the next chapter.



## 2. SuperSymmetry

Supersymmetry (SUSY) is a proposed new symmetry of nature. It introduces a partner for every SM particle with the same quantum numbers but the spin. Every SM fermion should have a SUSY partner that is a boson and viceversa. As will be shown later, the introduction of such a symmetry naturally cancels the quadratic divergencies in the corrections to the mass of the SM Higgs boson; it also provides a good candidate for astrophysical cold dark matter [1].

### 2.1 Why do we choose Supersymmetry as a theory beyond the SM?

As pointed out in Sec.(1.4), the theoretically preferred value for the Higgs mass should to be closer to the Planck than to the EW scale due to its mass corrections. This is the reason why, if the Higgs is an elementary particle, it is necessary to invoke a new symmetry which protects from divergences. The basic feature of the symmetry mentioned above, SUSY, is the equal number of fermions and bosons with identical coupling strenghts; in doubling the degrees of freedom, each supersymmetric partner (in general called *sparticle*, in particular *gaugino* for the gauge boson) provides another contribution to the Higgs self energy so that the residual one loop correction to the mass becomes:

$$\delta m_{H,W}^2 \simeq \mathcal{O}\left(\frac{\alpha}{\pi}\right)(m_B^2 - m_f^2) \quad (2.1)$$

that is not divergent with the crucial assumption  $(m_B^2 - m_f^2) \leq 1 \text{ TeV}^2$ , where  $m_B$  and  $m_F$  are the masses of the partners (SM fermion and SUSY boson, or *viceversa*). This yields a solution to the *naturalness* problem but it also implies the existence of supersymmetric particles with mass within the TeV scale: SUSY can be looked for at relatively low energy.

Beside the cancellation of these divergences in the mass corrections, there are other experimental hints to SUSY. From the phenomenological point of view, SUSY is supported by the precision measurements performed at LEP. It turns out that the gauge coupling constants don't unify in a SM framework; on the other hand, the coupling constants become equal at  $E \approx 10^{16}$  GeV if SUSY is assumed (Fig.2.1) [2]. Moreover, the precision EW data prefer a relatively light Higgs boson with  $m_H < 200$  GeV, consistent with the calculation in the supersymmetric standard model (see Sec.3.3) where the lightest Higgs has mass  $< 130$  GeV. However, the strongest experimental support comes from the astrophysical necessity of cold dark matter (CDM). Recent measurements of the power structure of the cosmic microwave background and measurements of the distant supernovae point to a cold dark matter density:  $0.1 < \Omega < 0.3$ . The LSP (Lightest Supersymmetric Particle) is a good candidate for the CDM being a neutral, weakly interacting particle with mass  $< 1$  TeV. For more experimental hints to SUSY, namely  $b \rightarrow s\gamma$ , anomalous magnetic moment and  $B_S \rightarrow \mu^+\mu^-$ , see [3].

In the following sections, [4], [5], [6], [7], [8] and [9] are followed to give an overview of Supersymmetry.

## 2.2 A supersymmetric theory

Given that supersymmetry links fermions to bosons,  $Q$ , the generator of the Supersymmetry, turns a bosonic state into a fermionic one and viceversa; this implies that the generator itself carries half integer spin (fermionic generator). The simplest choice is a 2-component Weyl spinor with anticommuting relations:

$$\{Q_\alpha, Q_\beta\} = 0 \quad (2.2)$$

$$\{\bar{Q}_{\dot{\alpha}}, \bar{Q}_{\dot{\beta}}\} = 0 \quad (2.3)$$

$$\{Q_\alpha, \bar{Q}_{\dot{\beta}}\} = 2\sigma_{\alpha\dot{\beta}}^m P_m \quad (2.4)$$

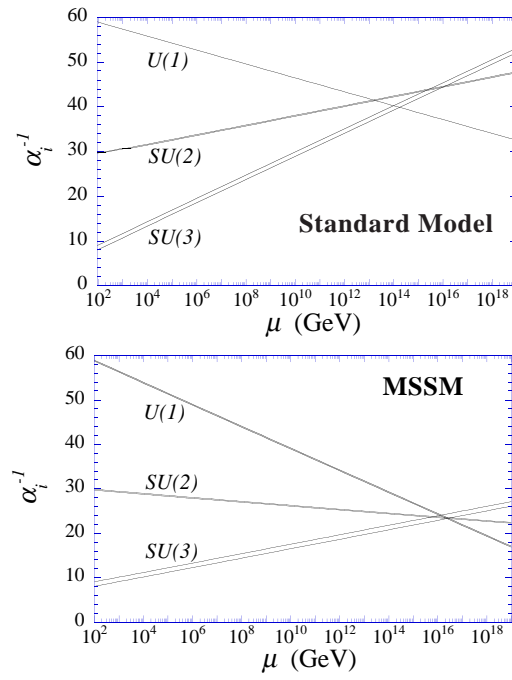


Figure 2.1. Running of gauge coupling constants in the SM and in the SUSY framework

where  $P_m$  is the generator of the translations in the ordinary space and  $\sigma^m$  is the four-vector of the Pauli matrices<sup>1</sup>. In the supersymmetric theory all single particles fall into an irreducible representation which is called *supermultiplet* in the same way that the proton and the neutron belong to a doublet for the isospin; each *supermultiplet* contains the SM particle  $|p\rangle$  and its supersymmetric partner, *sparticle*  $|\tilde{p}\rangle$ , found by applying a combination of  $Q$  and  $\bar{Q}$  to  $|p\rangle$ . It can be proved [10] that the fermionic degree of freedom equals the bosonic one. SUSY acts independently of any internal symmetry, namely the generator  $Q$  commutes with the gauge generators and the operator  $P$ ; in other words, particles and *sparticles* in a given *supermultiplet* have the same charge, weak isospin, color and mass.

It is usually convenient to introduce “fermionic coordinates” as *superpartners* of the standard space-time coordinates; these coordinates are anticommuting (Grassmann) variables,  $\theta$  and  $\bar{\theta}$  satisfying:

$$\{\theta^\alpha, \theta^\beta\} = \{\bar{\theta}_{\dot{\alpha}}, \bar{\theta}_{\dot{\beta}}\} = \{\theta^\alpha, \bar{\theta}_{\dot{\beta}}\} = 0. \quad (2.5)$$

A *finite* SUSY transformation can be written in terms of  $\theta$  and  $\bar{\theta}$  as follows:

$$\Omega(x, \theta, \bar{\theta}, \omega) = e^{i[-x^m P_m + \theta Q + \bar{\theta} \bar{Q}]} e^{-\frac{i}{2} \omega^{mn} M_{mn}} \quad (2.6)$$

with  $M_{mn}$  as generator of the ordinary rotations. In the chiral representation, where  $\theta$  and  $\bar{\theta}$  are treated independently, we define:

$$\Phi(x, \theta, \bar{\theta}) = \Phi_L(x_\mu + i\theta\sigma_\mu\bar{\theta}, \theta, \bar{\theta}) = \Phi_R(x_\mu - i\theta\sigma_\mu\bar{\theta}, \theta, \bar{\theta}) \quad (2.7)$$

L-representation

$$D_L = \partial_\theta + 2i\sigma^\mu\bar{\theta}\partial_\mu \quad (2.8)$$

$$\bar{D}_L = -\partial_{\bar{\theta}} \quad (2.9)$$

---

<sup>1</sup>The indices  $\alpha, \beta$  for  $Q$  and  $\dot{\alpha}, \dot{\beta}$  for  $\bar{Q}$  take values 1, 2.



## R-representation

$$\overline{D}_R = -\partial_{\overline{\theta}} - 2i\sigma^\mu\theta\partial_\mu \quad (2.10)$$

$$D_R = \partial_\theta \quad (2.11)$$

In the following section, two special kinds of *supermultiplets* are presented with the formalism of *superfields*, *i.e* as functions of the Grassmann variables just introduced.

### 2.2.1 Chiral superfield

The first type of *superfield* is the chiral (also called matter) *superfield*. It contains a single Weyl fermion (with 2 helicity states) and two real scalars; since the lowest spin component of the *supermultiplet* has spin  $S = 0$ . The simplest form of  $\Phi$  is constructed by the constraint:

$$\bar{D}_L\Phi_L \equiv 0 \quad (2.12)$$

$$D_R\Phi_R \equiv 0 \quad (2.13)$$

that gives:

$$\Phi_L(x, \theta) = \phi(x) + \sqrt{2}\theta\psi(x) + \theta\theta F(x) \quad (2.14)$$

where  $\phi$  and  $F$  are complex scalar fields and  $\psi$  is a left handed Weyl spinor. They can be identified with the bosonic SUSY partner ( $\phi$ ) of the SM fermion ( $\psi$ ); the field  $F$  is an auxiliary field that will be integrated out from the Lagrangian density and that does not correspond to any physical degree of freedom (see 3.3.4); this way, the number of fermionic degrees of freedom equals the bosonic one as required.

The Lagrangian density will depend upon transformations of the fields; it is therefore important to investigate how the *superfield* behaves under a SUSY transformation. It can be shown that:

$$\delta_S\phi = \sqrt{2}\alpha\psi \quad (\text{boson} \rightarrow \text{fermion}) \quad (2.15)$$

$$\delta_S\psi = \sqrt{2}\alpha F + i\sqrt{2}\sigma^\mu\bar{\alpha}\partial_\mu\phi \quad (\text{fermion} \rightarrow \text{boson}) \quad (2.16)$$

$$\delta_SF = -i\sqrt{2}\partial_\mu\psi\sigma^\mu\bar{\alpha} \quad (F \rightarrow \text{total derivative}) \quad (2.17)$$

The transformation mixes boson and fermionic components; the invariance of the equation of motion is though a result of SUSY. It is worth noticing that  $\int d^4x F(x)$  is invariant since it changes by a total derivative and it can be regarded as a good candidate for constructing the Lagrangian density, see Sec.(2.3).

### 2.2.2 Vector superfields

As in the SM, in order to write a local gauge invariant supersymmetric Lagrangian, a set of massless vector fields has to be introduced; in a supersymmetric theory, however, this cannot be accomplished without including the fermions that are the partners of the SM gauge fields. A vector *superfield* will be composed by a massless spin 1 vector boson (2 helicity states) and a spin  $\frac{1}{2}$  Weyl fermion (2 helicity states), being the generalization of the gauge field. By assuming the so called Wess-Zumino gauge we require:

$$V(x, \theta, \bar{\theta}) \equiv V^\dagger(x, \theta, \bar{\theta}). \quad (2.18)$$

the vector *superfield* can explicitly be written as:

$$V = -\theta\sigma_m\bar{\theta}A^m + i(\theta\theta)\bar{\theta}\bar{\lambda} - i(\bar{\theta}\bar{\theta})\theta\lambda + \frac{1}{2}(\theta\theta)(\bar{\theta}\bar{\theta})D. \quad (2.19)$$

where  $A^m$  is a vector field (it describes SM Yang-Mills potential),  $\lambda$  is a spinor (SUSY partner of the gauge boson, *gaugino*) and  $D$  is a real, scalar, non propagating field that can be eliminated from the Lagrangian by the Euler-Lagrange equations. Applying a SUSY transformation,  $D$  transforms into a total derivative:

$$\delta_S D = -\alpha\sigma^\mu\partial_\mu\bar{\lambda} + \bar{\alpha}\sigma^\mu\partial_\mu\lambda, \quad (2.20)$$

## 2.3 Supersymmetric lagrangian

In the previous section, the building blocks of the supersymmetric theory and their properties have been presented; to construct the Lagrangian, the kinetic contributions and the interactions of the fields must be defined. The following requirement

is the guiding principle in accomplishing this task: the action of a SUSY theory is SUSY invariant therefore,

$$\delta_S \int d^4x \mathcal{L}(x) = 0. \quad (2.21)$$

If the Lagrangian density changes by a total derivative, the action changes by a surface term and the equation of motions are left invariant. As already remarked in Sec.(2.2.2), the fields  $F$  and  $D$ , the highest component of the chiral and vector *superfields* in that they contain the largest number of  $\theta$  factors, satisfy this constraint transforming as total derivative; it's natural then to take advantage of such a feature by writing:

$$S = \int d^4x \left( \int d^2\theta \mathcal{L}_{\mathcal{F}} + \int d^2\theta d^2\bar{\theta} \mathcal{L}_{\mathcal{D}} \right), \quad (2.22)$$

where  $\mathcal{L}_{\mathcal{F}}$  and  $\mathcal{L}_{\mathcal{D}}$  stand for general chiral and vector *superfields* giving raise to the terms  $F$  and  $D$ . Next, the Lagrangian for the chiral *supermultiplets*, consisting of kinetic and of the so called *superpotential* terms, is described.

### 2.3.1 Kinetic contributions for the free *superfields*

The Hermitian conjugate of a left handed chiral *superfield* is right handed [10]; as a result, the product of a left handed and of a right handed chiral *superfield*,  $\Phi_L \Phi_L^\dagger$ , is a vector *superfield*, which can be identified with the  $D$  term in (2.22)). By substitution into Eq.(2.22) and Grassmann integration:

$$\mathcal{L}_{kin,chiral} \sim \int d^2\theta d^2\bar{\theta} \Phi_L \Phi_L^\dagger = F F^* - \phi \partial_\mu \partial^\mu \phi^* - i \bar{\psi} \sigma_\mu \partial^\mu \psi. \quad (2.23)$$

The term just built can be regarded as the kinetic contribution of the chiral *superfield* in that it contains kinetic term for the SM Weyl spinor  $\psi$  and that associated to  $\phi$ , the SUSY counterpart scalar field. It should be noticed that the field  $F$  is not associated to any kinetic contribution, meaning that it is a non-propagating (physical) field but it is just an auxiliary field.

### 2.3.2 Interaction terms

Any product of left chiral *superfields* is a left chiral *superfield*, implying that any analitical function of left chiral *superfield* satisfies this property. This leads to the introduction of an holomorphic function  $f(\Phi_i)$  called *superpotential* needed to describe the interaction between the chiral components. The general expression for that is:

$$f(\Phi_i) = \sum_i k_i \Phi_i + \frac{1}{2} \sum_{i,j} m_{ij} \Phi_i \Phi_j + \frac{1}{3} \sum_{i,j,k} g_{ijk} \Phi_i \Phi_j \Phi_k, \quad (2.24)$$

The  $F$  component of the new *superfield* has the property required for a Lagrangian density being invariant up to a total derivative under SUSY transformations so that, after calculations referred to in [6]:

$$\mathcal{L}_{int,chiral} \sim \int d^2\theta f(\phi) = -\frac{1}{2} \frac{\partial^2 f(\Phi_i)}{\partial \Phi_j \partial \Phi_k} + \frac{\partial f(\Phi_i)}{\partial \Phi_j} F_i \quad (2.25)$$

The first term describes the Yukawa coupling between fermionic and bosonic components of the chiral *superfield*; the second is the scala potential.

The quantities described so far contribute to the most general globally supersymmetric Lagrangian for a non-gauge interacting theory; a step further is needed to determine the Lagrangian for a gauge theory.

### 2.3.3 The gauge terms

First, the kinetic term for the vector *superfields*  $V$  have to be built. This is achieved by the help of a new *superfield* which, for abelian symmetries, reduces to:

$$W_\alpha = (\bar{D}_{\dot{\alpha}} \bar{D}_{\dot{\beta}} \epsilon^{\dot{\alpha}\dot{\beta}}) D_\alpha V \quad (2.26)$$

where  $D$  and  $\bar{D}$  are the SUSY covariant derivatives. Noticing that  $W_\alpha W^\alpha$  is invariant under abelian transformations, it can be written:

$$\begin{aligned} \mathcal{L}_{kin,gauge} \sim \int d^2\theta W_\alpha W^\alpha &= -\frac{1}{4} F_{\mu\nu}^a F_a^{\mu\nu} + \frac{1}{2} D_a D^a \\ &+ \left( -\frac{i}{2} \lambda^a \sigma_\mu \partial^\mu \bar{\lambda}_a + \frac{1}{2} g f^{abc} \lambda_a \sigma_\mu A_b^\mu \bar{\lambda}_c + h.c. \right) \end{aligned} \quad (2.27)$$

In addition to the kinetic energy for the SM gauge fields,  $\mathcal{L}_{kin,gauge}$  contains the kinetic term of the *gauginos* and the coupling of gauge to *gauginos* determined by the structure constants  $f^{abc}$ . Note that in Eq.(2.27) the field  $D$  does not have any kinetic term as it is just an auxiliary field.

Since the vector *supermultiplets* contain gauge fields, chiral *supermultiplets* that transform non trivially under the gauge group should couple to the vector *supermultiplets* to keep the Lagrangian invariant. This requires a modification of the kinetic lagrangian  $\mathcal{L}_{kin,chiral}$ :

$$\begin{aligned} \int d^2\theta d^2\bar{\theta} \Phi^\dagger \Phi &\longrightarrow \int d^2\theta d^2\bar{\theta} \Phi^\dagger e^{2gV} \Phi \\ &= |D_\mu \phi|^2 - i\bar{\psi} \sigma_\mu D^\mu \psi + g\phi^* D\phi + \\ &\quad ig\sqrt{2}(\phi^* \lambda \psi - \bar{\lambda} \bar{\psi} \phi) + |F|^2. \end{aligned} \quad (2.28)$$

Eq. (2.28) not only describes the interactions of the matter fields (both fermion and boson) with the gauge field but also contains the gauge-strenght Yukawa interaction between fermion  $\psi$ , boson  $\phi$  and the spinor  $\lambda$ , *gaugino*.

### 2.3.4 The Globally Supersymmetric Lagrangian

It is now possible to combine all contributions build so far to construct the globally supersymmetric Lagrangian. By the help of the *superpotential* Eq.(2.24) and the expression of the kinetic terms, the field  $F$  and  $D$  can be integrated out of the theory so that the Lagrangian looks like:

$$\begin{aligned} \mathcal{L} &= |D_\mu \phi|^2 - i\bar{\psi} \sigma_\mu D^\mu \psi - \frac{1}{4} F_{\mu\nu}^a F_a^{\mu\nu} + \\ &+ \frac{i}{2} \sum_A \bar{\lambda}_A \gamma^\mu D_\mu \lambda_A + ig'\sqrt{2}(\phi^* \lambda \psi - \bar{\lambda} \bar{\psi} \phi) - \frac{1}{2} \sum_a \left| \sum_{i,j} g' \phi_i^* T_{ij}^a \phi_j \right|^2 + \\ &- \left[ \sum_{j,k} \left( \frac{\partial^2 f(\Phi_i)}{\partial \Phi_j \partial \Phi_k} \right)_{\Phi_i=\phi_i, \Phi_j=\phi_j} \psi_j \psi_k + h.c. \right] - \left| \frac{\partial f(\Phi_i)}{\partial \Phi_j} \right|_{\Phi_j=\phi_j}^2 \end{aligned} \quad (2.29)$$

As already mentioned, the SM particles ( $\psi$ ) belong to the chiral *supermultiplet* together with their SUSY partners ( $\phi$ ), likewise the SM gauge bosons (corresponding

to the field  $A_m$ ) and the *gauginos*  $\lambda$  inhabit the vector *supermultiplet*. The first four terms in Eq.(2.29) are the kinetic energies of the chiral and vector *supermultiplets*; the derivatives are associated to the particular transformation. In other words, if dealing with SUSY QCD, the covariant derivative contains SU(3) matrices, *i.e.*  $D_\mu = \partial_\mu + ig_s \frac{\lambda_A}{s} V_A^\mu$  while the covariant derivative for the *gauginos* contain the octet matrices. These four terms describe how all particles interact with the gauge bosons. The next term is the interaction of the *gauginos* with the matter *supermultiplet*. Note that these interaction are determined by the gauge coupling. The sixth contribution represents the quartic coupling of the matter components associated to the coupling  $g'$ . This term comes from the elimination of the  $D$  field. What is left is the *superpotential* that represents the non-gauge interactions of the matter fields, such as the Yukawa interaction

### 2.3.5 Symmetry Breaking

As previously emphasized, the supersymmetric Lagrangian is built such that the Standard Model particles have the same mass as their supersymmetric partners; this is clearly not realistic since, for example, no supersymmetric electron with a mass of 511 MeV has been observed. Searches at LEP  $e^+e^-$  implied that charged *sparticles* must be heavier than 60-80 GeV, likewise searches at Tevatron  $p\bar{p}$  bound the mass of *squark* and *gluinos* to  $>150$  GeV. Hence SUSY must be a broken symmetry. In the low energy effective theory, the breaking mechanism is parametrized by inserting so called *soft* terms into the Lagrangian. *Soft* means that the cancellation of the quadratic divergences is still preserved. In a theory with a *superpotential* as in Eq.2.24 the possible soft breaking terms have the form:

- scalar mass terms  $-m_{\phi_i}^2 |\phi^2|$ , explicit masses for the scalar member of the chiral *multiplets*

- gaugino mass terms  $-\frac{1}{2}m_l\bar{\lambda}_l\lambda_l$  where  $l$  labels the group factor, an independent gaugino mass for each factor of a direct product gauge group (for instance,  $M_1, M_2, M_3$  for  $U(1)_Y \times SU(2)_L \times SU(3)_C$ )
- trilinear scalar interactions  $-A_{ijk}\phi_i\phi_j\phi_k + h.c.$ , so called A terms
- bilinear terms  $-B_{ij}\phi_i\phi_j + h.c.$ , so called B terms
- linear terms  $-C_i\phi_i$

The scalar and gaugino masses obviously break the degeneracy between the masses of particle and sparticles.

This completes the discussion about the SUSY Lagrangian. These results will be applied to the simplest model, the supersymmetrization of the SM, the so called MSSM (Minimal Supersymmetric Standard Model).





### 3. Minimal Supersymmetric Standard Model

The Minimal Supersymmetric Standard Model, MSSM, is the supersymmetrization of the SM where *minimal* means that the number of *superfields* and interactions is kept as small as possible. As already explained, the SUSY formalism requires two types of *supermultiplets*, the chiral and the vector *supermultiplets*. We correlate here the particle content of the MSSM and the *superfields* introduced earlier.

#### 3.1 Particle content

The nomenclature of all particles in the MSSM follows simple rules. All quarks, leptons are called in the same way as in the SM while the *superpartners* are named with an “s” at the beginning standing for scalar. In general fermionic *superpartners* of SM bosons have an “ino” at the end of the name; in particular *gluino* for gluon, *wino* for W and *bino* for B.

##### 3.1.1 Chiral content

The chiral *supermultiplets* contains the SM fermion and the bosonic partner; the *supermultiplet* itself is referred to with the capital letter, see Tab.3.1.1. Next, the correlation between the *superfield* and the MSSM content is clarified:

- superfield  $\Phi_i \in \{Q, \bar{U}, \bar{D}, L, \bar{E} + \text{other families}\};$
- spinor  $\psi_i \in \left\{ \begin{pmatrix} u \\ d \end{pmatrix}_L, u_R, d_R, \begin{pmatrix} \nu \\ e \end{pmatrix}_L, e_R + \text{other families} \right\};$
- complex scalar  $\phi_i \in \left\{ \begin{pmatrix} \tilde{u}_L \\ \tilde{d}_L \end{pmatrix}, \tilde{u}_R, \tilde{d}_R, \begin{pmatrix} \tilde{\nu}_L \\ \tilde{e}_L \end{pmatrix}, \tilde{e}_R + \text{other families} \right\}.$

multiplet		spin 0	spin 1/2	$SU_C(3), SU_L(2), U_Y(1)$
squarks, quarks (3 families)	$Q$	$(\tilde{u}_L, \tilde{d}_L)$	$(u_L, d_L)$	$(\mathbf{3}, \mathbf{2}, 1/6)$
	$\bar{U}$	$\tilde{u}_R^*$	$\bar{u}_R$	$(\bar{\mathbf{3}}, \mathbf{1}, -2/3)$
	$\bar{D}$	$\tilde{d}_R^*$	$\bar{d}_R$	$(\bar{\mathbf{3}}, \mathbf{1}, 1/3)$
sleptons, leptons (3 families)	$L$	$(\tilde{\nu}_L, \tilde{e}_L)$	$(\nu_L, e_L)$	$(\mathbf{1}, \mathbf{1}, -1/2)$
	$\bar{E}$	$\tilde{e}_R^*$	$\bar{e}_R$	$(\mathbf{1}, \mathbf{1}, 1)$
Higgs, Higgsino	$H_u$	$(H_u^+, H_u^0)$	$(\tilde{H}_u^+, \tilde{H}_u^0)$	$(\mathbf{1}, \mathbf{2}, 1/2)$
	$H_d$	$(H_d^0, H_d^-)$	$(\tilde{H}_d^0, \tilde{H}_d^-)$	$(\mathbf{1}, \mathbf{2}, -1/2)$

Table 3.1  
Chiral multiplets in the MSSM

Coming to the electroweak symmetry breaking sector, in the SM the symmetry is broken by a single Higgs doublet which acquires a non vanishing value in the ground state. Moreover, the same field gives mass to the fermions by the Yukawa interactions. This is possible since the doublet couples to the  $T_3 = +\frac{1}{2}$  or the  $T_3 = -\frac{1}{2}$  fermions. In a supersymmetric theory however, the Yukawa interactions come from a *superpotential* that cannot depend on a field and its conjugate at the same time. As a result, any doublet can give mass either to  $T_3 = +\frac{1}{2}$  or to  $T_3 = -\frac{1}{2}$ . Thus, in order to give mass to all *sfermions*, two doublets must be introduced. These are the two Higgs doublet chiral *superfields* formed by the Higgs and the Higgsino. The analogy between the formalism introduced earlier and the field content of MSSM is here shown for the Higgs sector:

- superfield  $\Phi_i \in \{H_u, H_d\}$ ;
- spinor  $\psi_i \in \left\{ \begin{pmatrix} \widetilde{H}_u^+ \\ \widetilde{H}_u^0 \end{pmatrix}, \begin{pmatrix} \widetilde{H}_d^0 \\ \widetilde{H}_d^- \end{pmatrix} \right\}$ ;
- complex scalar  $\phi_i \in \left\{ \begin{pmatrix} H_u^+ \\ H_u^0 \end{pmatrix}, \begin{pmatrix} H_d^0 \\ H_d^- \end{pmatrix} \right\}$

### 3.1.2 Gauge content

In the gauge sector, there is a gauge or vector *supermultiplets* for each factor of the gauge group: eight *gluinos*  $\tilde{g}$  as partners of the QCD gluons, three *winos*  $\tilde{W}$  for the  $SU(2)_L$  gauge bosons, a *bino*  $\tilde{B}$  for  $U(1)_Y$ . Since the  $SU(2)_L \times U(1)_Y$  symmetry is broken in nature, the *winos* and the *bino* are not mass eigenstates; they mix with fields with the same electric charge but different  $SU(2)_L \times U(1)_Y$  quantum numbers (see Sec.(3.3.1)).

multiplet	spin 1/2	spin 1	$SU_C(3), SU_L(2), U_Y(1)$
<i>gluinos</i> , gluons	$\tilde{g}$	$g$	$(\mathbf{8}, \mathbf{1}, 0)$
<i>winos</i> , W bosons	$\tilde{W}^\pm \tilde{W}^0$	$W^\pm W^0$	$(\mathbf{1}, \mathbf{3}, 0)$
<i>binos</i> , B bosons	$\tilde{B}^0$	$B^0$	$(\mathbf{1}, \mathbf{1}, 0)$

Table 3.2  
Vector multiplets in the MSSM

### 3.2 Superpotential

Being the particle content defined, the next step is to identify the interactions, namely the form acquired by the *superpotential* in the framework of the MSSM. The gauge interactions are determined by the choice of the gauge group but they are not completely fixed so that they can be chosen according to the principle of “minimality”: only the terms that are needed are introduced. This approach leads to the following choice for the *superpotential*:

$$f_{\text{MSSM}} = \overline{U} \mathbf{y}_u Q H_u - \overline{D} \mathbf{y}_d Q H_d - \overline{E} \mathbf{y}_e L H_d + \mu H_u H_d, \quad (3.1)$$

where the  $\mathbf{y}_u, \mathbf{y}_d, \mathbf{y}_e$  are the Yukawa couplings.

The first three terms correspond to the Yukawa coupling in the SM; the parameter  $\mu$  in the Higgs contribution gives mass to fermionic and bosonic component of the

chiral *supermultiplets*  $\hat{H}_u$  and  $\hat{H}_d$ . The choice of this *superpotential* is associated to the concept of R parity ( $R_P$ ) conservation <sup>1</sup> This is a discrete  $U(1)$  symmetry given by:

$$R = (-1)^{3B+L+2j} \quad (3.2)$$

where  $B$  is the baryon number,  $L$  is the lepton number and  $j$  is the spin. Under  $R_P$ , all SM particles carry even parity ( $R_P = 1$ ) while the *sparticles* odd ( $R_P = -1$ ). Once this new symmetry is imposed, the only terms allowed are the one listed in Eq.2.24. One of the consequence of R-parity conservation is that the lightest supersymmetric particle is stable implying that the LSP is the best candidate for the cold dark matter [11] [12]. As far as collider experiments are concerned, an LSP will then look like a heavy neutrino which escaped detection. Moreover, as a result of R parity conservation, *sparticle* could be only produced in pair at colliders.

### 3.3 EW breaking in the contest of the MSSM

It is convenient to re-write the *superpotential* and the soft term related to the Higgs boson altogether as follows:

$$V = \frac{g'^2}{2} \left( H_u^\dagger \frac{1}{2} H_u + H_d^\dagger \frac{-1}{2} H_d \right)^2 + \frac{g^2}{2} \left( H_u^\dagger \frac{\vec{\tau}}{2} H_u + H_d^\dagger \frac{\vec{\tau}}{2} H_d \right)^2 \\ + \mu^2 (|H_u|^2 + |H_d|^2) + m_{H_u}^2 |H_u|^2 + m_{H_d}^2 |H_d|^2 - (B\mu H_u H_d + c.c.) \quad (3.3)$$

By using  $SU(2)_L$  gauge transformations, the Higgs boson can be gauge-rotated such that:

$$\langle H_u \rangle = \begin{pmatrix} 0 \\ v_u \end{pmatrix}, \quad \langle H_d \rangle = \begin{pmatrix} v_d \\ 0 \end{pmatrix}, \quad (3.4)$$

---

<sup>1</sup>Terms of the form  $UDD, QDL, LEL$  could be added to the Lagrangian; but these would allow for lepton and baryon number violation and proton decay. To avoid this, the previous choice of *superpotential* is done and related to the conservation of a new quantum number

It is convenient to write the ratio of the expectation values as  $\tan\beta = \frac{v_u}{v_d}$ . If Eq.(3.4) is substituted into the expression for the potential, the latest can be rewritten as:

$$V = \frac{g_Z^2}{8}(v_u^2 - v_d^2)^2 + (v_u \ v_d) \begin{pmatrix} \mu^2 + m_{H_u}^2 & -B\mu \\ -B\mu & \mu^2 + m_{H_d}^2 \end{pmatrix} \begin{pmatrix} v_u \\ v_d \end{pmatrix}, \quad (3.5)$$

where  $g_Z^2 = g^2 + g'^2$ . To prevent the quartic term from vanishing, the potential has to satisfy:  $\mu^2 + m_{H_u}^2 + \mu^2 + m_{H_d}^2 > 2\mu B$ ; whereas, to reproduce the mass of the  $Z$ -boson:  $v_u = \frac{v}{\sqrt{2}} \sin \beta$ ,  $v_d = \frac{v}{\sqrt{2}} \cos \beta$ ,  $v = 250$  GeV.

Because there are two Higgs doublets, each of which with four real scalar fields, the number of degrees of freedom is eight before the symmetry breaking. However three of them are eaten by  $W^+$ ,  $W^-$  and  $Z$  bosons, and five physical scalar particles are left. There are two CP-even scalars  $h^0$ ,  $H^0$ , one CP-odd scalar  $A^0$ , and two charged scalars  $H^+$  and  $H^-$ . Their masses can be related to each other by using Eq.(3.5):

$$m_A^2 = 2\mu^2 + m_{H_u}^2 + m_{H_d}^2, \quad m_{H^\pm}^2 = m_W^2 + m_A^2, \quad (3.6)$$

$$m_{h^0}^2, m_{H^0}^2 = \frac{1}{2} \left( m_A^2 + m_Z^2 \pm \sqrt{(m_A^2 + m_Z^2)^2 - 4m_Z^2 m_A^2 \cos^2 2\beta} \right). \quad (3.7)$$

As a result, the lighter CP-even Higgs mass  $m_{h^0}^2$  is maximized when  $\cos^2 2\beta = 1$ :  $m_{h^0}^2 = (m_A^2 + m_Z^2 - |m_A^2 - m_Z^2|)/2$ . When  $m_A < m_Z$ , we obtain  $m_{h^0}^2 = m_A^2 < m_Z^2$ , while when  $m_A > m_Z$ ,  $m_{h^0}^2 = m_Z^2$ . Therefore:

$$m_{h^0} \leq m_Z. \quad (3.8)$$

This is a crucial prediction in the MSSM. However, this prediction must be modified due to the quantum corrections to the mass, namely:

$$\Delta(m_{h^0}^2) \sim v^2 \sin^4 \beta \log \left( \frac{m_{\tilde{t}_1} m_{\tilde{t}_2}}{m_t^2} \right). \quad (3.9)$$

where  $\tilde{t}_1$  and  $\tilde{t}_2$  are the mass eigenstates of the *stop*, the scalar partner of the SM top quark. If their mass is fixed to the scale 1 TeV and the top mass is 175 GeV, then

the lightest Higgs mass is about 130 GeV. Indeed most of the *sparticle* interactions are set by the corresponding interactions of their SM partners; this implies that the *stop* corrections to the mass are most relevant, as for the top quark in the SM.

### 3.3.1 Mass eigenstates in the contest of MSSM

The SUSY mixing in the scalar sector is described in details in [9] while a more detailed description is presented here for the mixing of SUSY fermions. The gauginos and higgsinos are the only spin  $\frac{1}{2}$  fermions. Of these, the *gluinos*, being a color octet, are unmixed and have a mass  $m_{\tilde{g}} = |M_3|$  while the electroweak gauginos and higgsinos of the same electric charge can mix once the EW symmetry is broken. The physical charginos ( $\tilde{\chi}_i^\pm$ ) are therefore mixtures of the electrically charged  $SU(2)_L$  gauginos and the electrically charged higgsinos. Their mass matrix [in the basis  $(\tilde{W}^\pm, H^\pm)$ ] can be written as:

$$\mathcal{M}_\pm = \begin{pmatrix} M_2 & \sqrt{2}M_W \sin\beta \\ \sqrt{2}M_W \cos\beta & \mu \end{pmatrix}. \quad (3.10)$$

In Eq.(3.10), the  $\mu$  entry is the Higgs mixing term coming from the *superpotential*, while  $M_2$  is the mass term for  $SU(2)$  gaugino.  $\tan\beta$  is the ratio of the vacuum expectation values for the up and the down Higgs fields. The neutralinos ( $\tilde{\chi}_i^0$ ) are instead mixtures of the  $\tilde{B}$ , the neutral  $\tilde{W}$ , and the two neutral higgsinos. These states form four distinct Majorana fermions, which are eigenstates of the symmetric mass matrix [in the basis  $(\tilde{B}, \tilde{W}, \tilde{h}^0, \tilde{\bar{h}}^0)$ ]:

$$\mathcal{M}_0 = \begin{pmatrix} M_1 & 0 & -M_Z \cos\beta \sin\theta_W & M_Z \sin\beta \sin\theta_W \\ 0 & M_2 & M_Z \cos\beta \cos\theta_W & -M_Z \sin\beta \cos\theta_W \\ -M_Z \cos\beta \sin\theta_W & M_Z \cos\beta \cos\theta_W & 0 & -\mu \\ M_Z \sin\beta \sin\theta_W & -M_Z \sin\beta \cos\theta_W & -\mu & 0 \end{pmatrix} \quad (3.11)$$

The masses and mixing angles of the charginos and neutralinos are therefore completely determined by the values of the four parameters the mass of the  $U(1)$  gaugino  $M_1$ ,  $M_2$ ,  $\mu$  and  $\tan\beta$ . One further assumption to reduce the dimensionality of the

parameter space is to unify the gaugino masses at the GUT scale. This could be motivated by the observation that in the MSSM the three gauge couplings tend to meet at this scale. In the gaugino mass unification assumption, since the gaugino masses  $M_i$  run in the same way as the corresponding squared gauge couplings  $g_i^2$ , the following relation holds:

$$M_1(M_Z) = \frac{5}{3} \tan\beta^2 \theta_W M_2(M_Z) \simeq \frac{1}{2} M_2(M_Z), \quad (3.12)$$

Within this assumption, the constraints from the charginos alone can be translated into constraints on the neutralino sector. If  $|\mu| > |M_2| \geq M_Z$ , the two lightest neutralino states will be dominated by the gaugino components, with low neutralino being mostly  $\tilde{B}$  and heavier neutralino being mostly  $\tilde{W}^0$ ; similarly, the light chargino will be mostly a charged *wino*. In this case:  $m_{\tilde{\chi}_i^\pm} \simeq m_{\tilde{\chi}_2^0} \simeq 2m_{\tilde{\chi}_1^0}$ . In the opposite limit,  $|\mu| < |M_1|$ , the two lighter neutralinos and the lighter chargino are all mostly higgsinos, with masses close to  $|\mu|$ . Finally, if  $|\mu| \simeq |M_2|$ , some of the states will be mixed. The size of the mixing depends also on  $\tan\beta$ . If  $\tan\beta$  is not large, there will be considerably more mixing if  $M_2 \cdot \mu \cdot \tan\beta > 0$  than for the opposite choice of sign. Such mixing decreases the mass of the light eigenstates, and increases that of the heavy ones. Depending on the higgsino and gaugino components, the coupling to the gauge bosons and to the left-right handed *sfermions* differ radically and the production therefore decay processes will strongly depend on that composition.

### 3.4 Supersymmetry breaking in the context of the MSSM

In addition to the interaction arising from the *superpotential* (Eq.2.24), *soft* breaking terms have to be added to the Lagrangian in the assumption of R parity conservation. By following the prescriptions of Sec.(2.3.5), the *soft* lagrangian contribution becomes:

$$\begin{aligned} \mathcal{L}_{\text{soft}} = & -\frac{1}{2} \left( M_3 \tilde{g} \tilde{g} + M_2 \tilde{W} \tilde{W} + M_1 \tilde{B} \tilde{B} \right) + h.c. \\ & - \left( \tilde{u} \mathbf{a}_u \tilde{Q} H_u - \tilde{d} \mathbf{a}_d \tilde{Q} H_d - \tilde{e} \mathbf{a}_e \tilde{Q} H_d \right) + h.c. \end{aligned}$$

$$\begin{aligned}
& -\tilde{Q}^\dagger \mathbf{m}_Q^2 \tilde{Q} - \tilde{L}^\dagger \mathbf{m}_L^2 \tilde{L} - \tilde{u} \mathbf{m}_u^2 \tilde{u}^\dagger - \tilde{d} \mathbf{m}_d^2 \tilde{d}^\dagger - \tilde{e} \mathbf{m}_e^2 \tilde{e}^\dagger \\
& - m_{H_u}^2 H_u^* H_u - m_{H_d}^2 H_d^* H_d - (B\mu H_u H_d + h.c.) .
\end{aligned} \tag{3.13}$$

where

- $M_i$  are the masses of gauginos (*gluino, winos, bino*)
- $\mathbf{a}$  are the trilinear couplings
- $\mathbf{m}$  are the squarks and sleptons masses (3x3 matrices in the family space)
- $m_{H_u}^2, m_{H_d}^2$  and  $B\mu$  are 2x2 isospin matrices

As a result, the theory now depends upon almost 100 free parameters: it is clear that crucial assumptions are necessary to decrease the number of free parameters. First, it can be assumed that SUSY does not distinguish between flavor, giving so diagonal matrices in the family space:

$$\mathbf{m}_Q^2 = m_Q^2 \mathbf{1}; \quad \mathbf{m}_u^2 = m_u^2 \mathbf{1}; \quad \mathbf{m}_d^2 = m_d^2 \mathbf{1}; \quad \mathbf{m}_L^2 = m_L^2 \mathbf{1}; \quad \mathbf{m}_e^2 = m_e^2 \mathbf{1}. \tag{3.14}$$

Another simplification regarding the third family can be done:

$$\mathbf{a}_u = A_{u0} \mathbf{y}_u; \quad \mathbf{a}_d = A_{d0} \mathbf{y}_d; \quad \mathbf{a}_e = A_{e0} \mathbf{y}_e. \tag{3.15}$$

This way, the third family, associated to the largest Yukawa contribution, gets the largest soft term.

### 3.5 Minimal SUPERGRAVITY

As explained earlier (Sec. 3.4), the symmetry breaking is parametrized by adding the *soft* terms to the low energy effective lagrangian. Nevertheless, several are the theoretical models proposed to explain *how* SUSY breaks, the oldest one being the minimal supergravity or mSUGRA. This model is based on promoting SUSY to local symmetry which requires the introduction of additional *superfields*. Indeed



mSUGRA assumes the existence of extrafields populating a so called *hidden sector*, which will couple to the MSSM fields only through gravitational interactions. The coupling will be proportional to  $M_{Pl}^{-1}$  which protects the *soft* sector from divergences. Given these assumptions, the simplest way to break supersymmetry is to adopt the Higgs mechanism in the *hidden sector*: namely, some of the components of the *hidden sector* acquire expectation values by minimization of the *superpotential*. The symmetry is spontaneously broken with the gravitino developing a mass of  $\mathcal{O}(\frac{1}{M_{Pl}})$  and the graviton remaining massless. The interaction between the *superfields* in the *hidden sector* and the MSSM *superfields* gives rise to *soft* SUSY breaking terms in the MSSM Lagrangian at which turn out to be the same as in Eq. 3.13 when run down to the EW scale. However, the number of free parameters in the theory would be still over 100.

mSUGRA reduces that in assuming a universal coupling of the *sparticles* to the *hidden sector*, namely:

- all scalars (sleptons, squarks) have a common mass  $m_0$ ,
- all gauginos (bino, wino, gluino) have a common mass  $m_{\frac{1}{2}}$ ,
- the trilinear coupling unify to  $A_0$

at the GUT scale. Additional parameters are:

- $\tan(\beta)$ , the ratio of the Higgs expectation values,
- $sgn(\mu)$ , the sign of the Higgs mixing term.

Even if the supersymmetric particle masses are unify at the GUT scale, this universality does not imply though that the masses are the same at the electroweak scale; the Lagrangian parameters have to be evolved down to the EW scale. The evolution is performed by the Renormalization Group Equations ([10]) and leads to a definite pattern of *sparticles* masses with values strongly dependent on the choice of the GUT

parameters. The gaugino masses  $M_i$  evaluated at the EW scale are related to the gauge couplings as follows:

$$M_i = m_{\frac{1}{2}} \frac{\alpha_i}{\alpha_G} \quad (3.16)$$

In the mSUGRA scenario it can be shown that the Higgsino term  $\mu$  is greater than the Bino and Wino mass; as a result the lightest neutralino and chargino tend to be gaugino-like where the mass hierarchy is approximately:

$$m_{\tilde{\chi}_2^0} \sim 2m_{\tilde{\chi}_1^0} \sim m_{\tilde{\chi}_{\pm}^1} \sim m_{\frac{1}{2}} \quad (3.17)$$

The squark mass parameters evolve mainly through the strong coupling to the gluino so the dependance on that is greater than for sleptons; for the first and second generations:

$$m_{q_{1,2}}^2 \sim m_0^2 + (5 \div 6)m_{\frac{1}{2}}^2 \quad (3.18)$$

whereas slepton masses satisfy:

$$m_{l_{1,2}}^2 \sim m_0^2 + (0.5 \div 0.15)m_{\frac{1}{2}}^2 \quad (3.19)$$

The difference in the coefficient of  $m_{\frac{1}{2}}$  reflects the mentioned difference between the strong-EW and EW only interaction for squarks and sleptons. Moreover, right-handed sleptons are lighter than left-handed being subjected to the hypercharge interaction only. For what concerns the third generation, the Yukawa term plays a crucial role and the spectra could dramatically change. The Yukawa interaction tend to reduce the scalar mass so that  $\tilde{t}_L$  and  $\tilde{t}_R$  tend to be lighter than the other squarks; the Yukawa terms induces also mixing between left and right component reducing further the lightest mass ( $\tilde{t}_1$ ). The behavior of the  $\tilde{\tau}$  is similar.

## 4. The Experiment

Located about 35 miles west of Chicago, Illinois, the Fermi National Accelerator Laboratory (**Fermilab**) is one of the main particle physics facilities in the world. It was built in the late sixties, funded by the Department Of Energy of the United States. During these forty years several experiments took place, giving important contribution to the understanding of the Standard Model of Fundamental Particles and Forces. In 1977, the Fermilab experiment E288 observed a new particle, the Upsilon, composed of a new kind of quark and its antimatter partner, giving the first evidence for the existence of the bottom quark. In 1995 the CDF and D0 experiments at the Tevatron proton-antiproton Collider completed the quark sector of the SM with the observation of the top quark. In July 2000, the DONUT experiment announced the first direct observation of the tau neutrino, filling the final slot in the lepton sector of the Standard Model. The tau neutrino set the stage for new discoveries and new physics with the inauguration of Collider Run II of the Tevatron in March 2001. The Run II, designed to meet the goals of the new particle physics frontiers, involved a complete upgrade of the full Fermilab accelerator complex. Now that the Run II phase has started, the Tevatron is the highest-energy particle accelerator currently operational ever developed. A complete description of the CDF detector can be found in [13].

### 4.1 The Fermilab Tevatron

The Fermilab accelerator complex, as shown in Figure 4.1, is composed of five different accelerators - the Cockcroft-Walton, the Linac, the Booster, the Main Injector, and the Tevatron - which, working in cascade, accelerate in opposite directions bunches of protons and antiprotons to the energy of 980 GeV. The total energy

# FERMILAB'S ACCELERATOR CHAIN

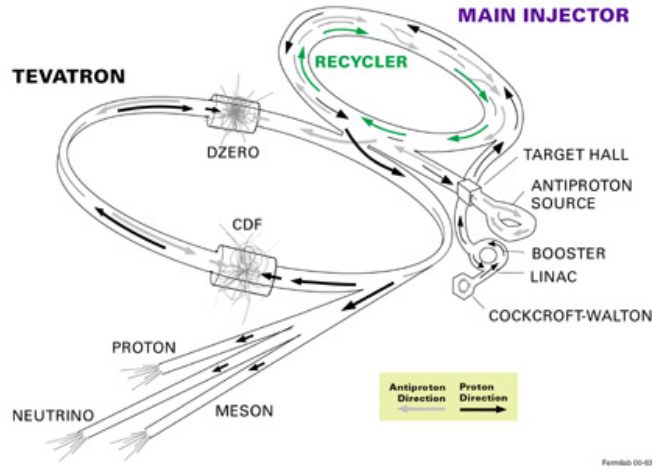


Figure 4.1. A schematic drawing of the Fermilab accelerator complex.

available in any proton-antiproton collision is then 1.96 TeV. The cross section will depend on this value which also sets the upper threshold to the mass of particles which can be produced.

Another key parameter in collider experiments is the luminosity, which determines the number of collisions per unit time. For a certain process with a cross section  $\sigma$  the number of events in a time interval  $\Delta T$  is given by the relation

$$N = \sigma \cdot \int_{\Delta T} L dt = \sigma \mathcal{L} \quad (4.1)$$

where  $\mathcal{L}$  is the “integrated luminosity” collected in the time interval  $\Delta T$ . This quantity is actually measured by counting the number of total proton-antiproton collisions per second and it is expressed in  $\text{cm}^{-2}\text{s}^{-1}$ .

The Run II upgrades on both the accelerator and the detector, were driven by the above equation. In order to improve the potential discovery and reach a better sensitivity for high precision measurement, the number of events collected by the Tevatron experiments had to be increased.

To achieve this goal the Tevatron was redesigned to provide an higher luminosity. Moreover, the center of mass energy of the proton-antiproton system has been

increased by 10%, which translates into a higher interaction cross section for most physical processes.

The higher Tevatron instantaneous luminosity due to the increase of the number of bunches in each beam as well as to the greater number of protons and antiprotons per bunch. In fact the instantaneous luminosity  $\mathcal{L}$  is given by:

$$\mathcal{L} \sim \frac{fBN_pN_{\bar{p}}}{2\pi(\sigma_p^2 + \sigma_{\bar{p}}^2)} \quad (4.2)$$

where  $f$  is the revolution frequency,  $B$  the number of bunches in each beam,  $N_p$  and  $N_{\bar{p}}$  the number of protons and antiprotons per bunch,  $\sigma_p$  and  $\sigma_{\bar{p}}$  the transverse beam size at the interaction point. Although the instantaneous luminosity is proportional to the number of particles per bunch, its value is limited from above by the number of interactions per bunch crossing, which is also related to the number of particles. This limitation is due to the superposition of several  $p - \bar{p}$  interactions within the same bunch crossing, resulting in an increase of the event complexity.

The average number of interaction per bunch crossing is shown in figure 4.2 as a function of the instantaneous luminosity for different number of bunches.

From the plot it is evident that, at a fixed instantaneous luminosity, to keep the number of interactions per bunch reasonably small, the number of bunches in each beam has to be increased. More bunches results in a shorter interval between each interactions. This time interval is the clock of the whole apparatus: accelerator and detectors. Presently the Tevatron is running with  $36 \times 36$  bunches.

#### 4.1.1 Production of Protons and Boosting

Protons are extracted from negative ionized Hydrogen gas. Hydrogen molecules are passed through a magnetron, which extracts ions, consisting of two electrons and one proton, and accelerates them to the energy of 25 KeV. These ions are then accelerated using the potential difference supplied by the Cockroft-Walton preaccelerator, which produces a beam of 750 keV  $H^-$  ions. The  $H^-$  ions subsequently enter the second stage of the accelerator process, the Linac.

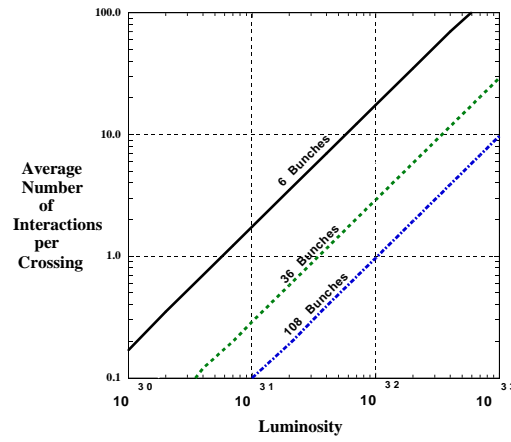


Figure 4.2. Average number of interactions per bunch crossing as a function of the instantaneous luminosity for different beam conditions.

The Linac is a linear accelerator about 150 m long, which increases the energy of the  $H^-$  to 400 MeV, by means of radio frequency cavities. The beam of ions is then injected in the Booster, a small synchrotron having 150 m of diameter, where ions are merged with the already circulating protons. Then this combined beam is focused on a thin carbon sheet, which strips the  $H^-$  of their two electrons. The resulting protons, using radio frequency cavities, are here packed into bunches and accelerated to 8 GeV. Protons are now ready to be transferred into the Main Injector.

#### 4.1.2 The Main Injector

The Main Injector substitutes the old Main Ring, and it was designed to fulfill the new operational requirements needed by the Tevatron Run II.

The Main Injector is a synchrotron of 3 Km of circumference, where protons and antiprotons are accelerated to 150 GeV before they enter the adjacent Tevatron. The main feature of this new synchrotron, compared to the Main Ring, is the larger particle acceptance to accommodate bunches from the Booster. Another important capability of the Main Injector consists in the possibility of decelerating antiprotons,

when the Tevatron is not in a collide mode. With this functionality antiprotons can be recovered and stored until a new run starts.

#### 4.1.3 Antiproton Production and Cooling

Antiprotons are produced by dumping onto a nickel target a 120 GeV proton bunch extracted from the Main Injector. Among the variety of particles generated in the collision, antiprotons of about 8 GeV energy are produced and collected through lithium lenses and dedicated magnetic field. Antiprotons are then injected into the Debuncher Ring, where, by means of the “stochastic cooling” technique, their momentum spread is reduced, while they are collected as a continuous beam. Subsequently antiprotons are sent to the Accumulator, where they are further cooled and stacked into bunches. The stacking rate, thanks to the Run II upgrades, has been increased by a factor of 3 with respect to Run I, which finally results in higher luminosity. When a sufficient number of antiprotons is available, they are accelerated to 150 GeV and, together with the protons, transferred to the Tevatron for the ultimate acceleration stage before the collisions.

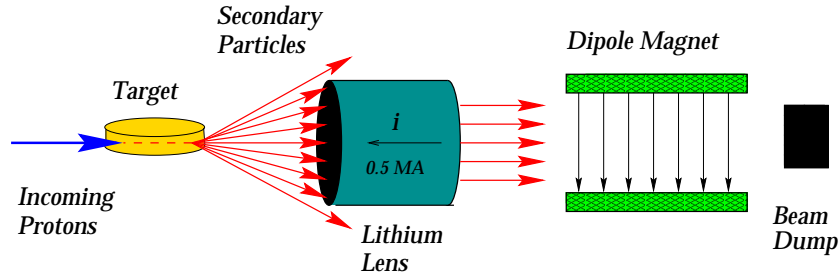


Figure 4.3. Schematic diagram which illustrates the antiproton production and selection chain.

#### 4.1.4 The Tevatron

The Tevatron is a proton-antiproton synchrotron collider. It is situated a few meters underground and its circumference is about 6 km. The Tevatron receives the protons and the antiprotons in the same beam pipe, where the two beams circulate in opposite directions. The Tevatron makes use of superconducting dipole magnets and quadrupole focusing magnets to provide a stable circular orbit for the protons and antiprotons.

Once 36 bunches of protons and 36 of antiprotons (“a store”) are circulating in the Tevatron the beam energies are ramped up together 0.98 TeV. The two beam, kept spatially separated during the acceleration stage, are then forced to collide in two regions around the ring. In these regions, where the two experiment D0 and CDF are located, a collision takes place every 396 ns.

The luminous region in CDF has a dispersion of about 30 cm in the directions of the beams ( $\sigma_z \sim 30$  cm) due to the geometrical configuration of the bunches. The transverse section of the beams is approximately circular and has a gaussian dispersion  $\sigma_t^{beam} \sim 30 \mu\text{m}$ . At present the Tevatron is reaching an instantaneous luminosity of about  $10^{31} \text{ cm}^{-2}\text{s}^{-1}$ .

#### 4.2 The Collider Detector at Fermilab

The CDF II detector, located at one of the six nominal interaction regions of Tevatron, is a general purpose detector which combines precision charged particle tracking with fast projective calorimetry and fine grained muon detection. A schematic view of one quadrant of the CDF II detector is given in Figure 4.5. It measures approximately 27 m from end-to-end, is about 10 m high, and weighs over 5000 tons. The right-handed coordinate system is defined with respect to the proton beam direction which gives the z-axis, the y-axis points vertically upward, and the x-axis lies on the plane defined by the Tevatron ring. The origin of the coordinate system is placed at the nominal interaction point that coincides with the center of



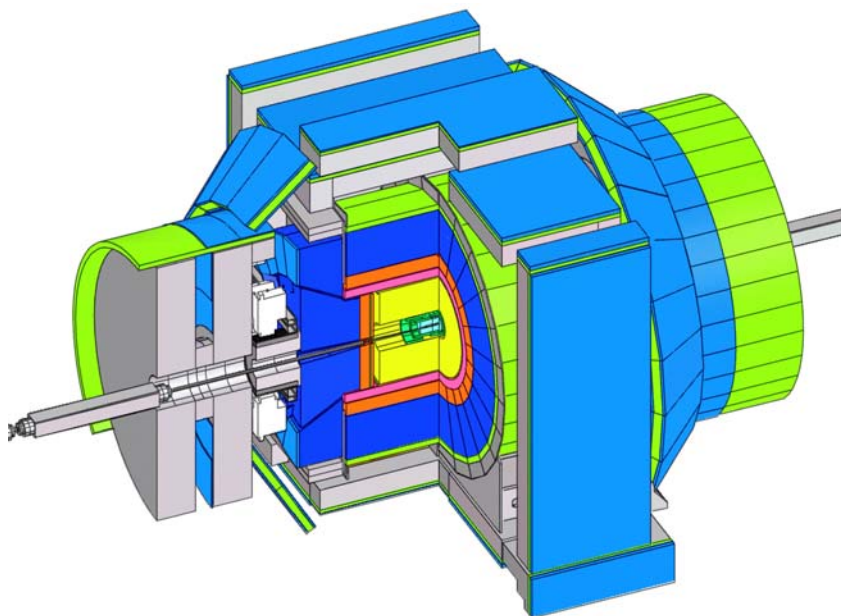


Figure 4.4. CDF Run II detector view.

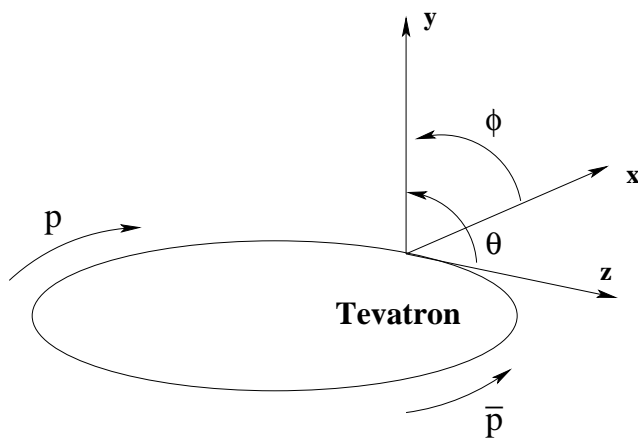


Figure 4.5. CDF Run II detector view.

the detector. The azimuthal angle ( $\phi$ ) is measured counterclockwise from the Tevatron plane, the polar angle ( $\theta$ ) is defined with respect to the positive z-axis, and the pseudo-rapidity ( $\eta$ ), is defined as:

$$\eta = -\ln \left[ \tan \beta \left( \frac{\theta}{2} \right) \right]. \quad (4.3)$$

To work with the new high luminosity and therefore with the high collision rate of Run II the CDF experiment underwent significant upgrades with many new features. In the following sections a description of the various subdetectors involved in this analysis is given as well as an overview of the major changes in the trigger and in the data acquisition system.

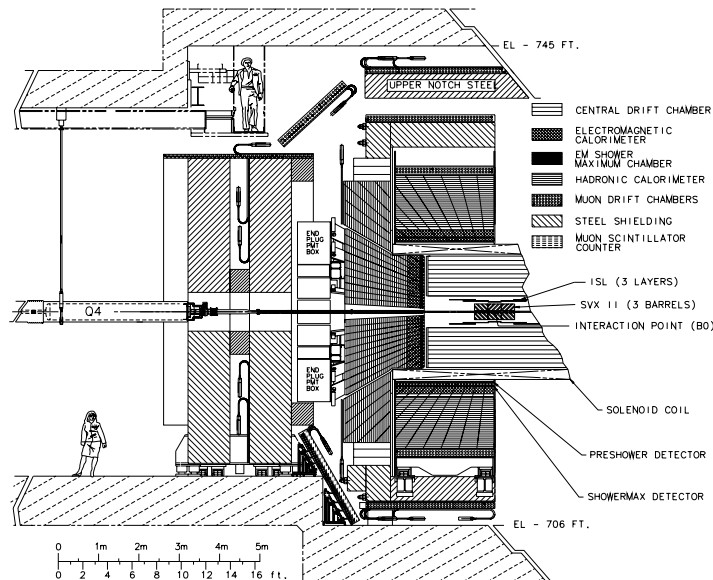


Figure 4.6. Longitudinal view of half of the CDF Run II detector.

#### 4.2.1 The Central Tracking System

The Central Tracking System is designed to reconstruct the trajectories of charged particles coming from the interaction vertex. The whole system is composed of four

subsystems that, coming from the nearest to the beam pipe, are the Layer 00 (**L00**), the Silicon Vertex Detector (**SVXII**), the Intermediate Silicon Layers (**ISL**) and the Central Outer Tracker (**COT**). The two innermost Silicon detectors provide an excellent 3D vertex measure inside  $|\eta| < 2$ , ISL allows forward tracking in a wider  $\eta$  range than the COT, and the COT completes the tracking in the central region ( $|\eta| < 1$ ) before the particles hit the calorimeter. All these devices are placed inside a solenoidal magnetic field of 1.41 Tesla parallel to the beam line. The field is uniform to 0.1% in the region  $|z| < 150$  cm and  $r < 150$  cm. The solenoid and the cryogenic equipment represent 0.85 radiation length ( $X_0$ ).

The curvature of the charged particles interacting with the magnetic field allows the extraction of precise information on the particle momentum as well as the sign of the charge. Starting from the Lorentz force, the transverse momentum of a reconstructed track is given by:

$$p_T = B \cdot |q| \cdot e \cdot \rho \quad (4.4)$$

where  $q$  is the particle charge,  $e$  is electron charge,  $B$  the magnetic field and  $\rho$  the radius of the helicoidal trajectory. The resolution of the whole tracking system on the track curvature has been estimated to be  $0.68 \times 10^{-4} \text{ cm}^{-1}$ , which translates into a momentum resolution of  $\sigma_{p_T}/P_T^2 \sim 6 \times 10^{-3} [\text{GeV}/c]^{-1}$ .

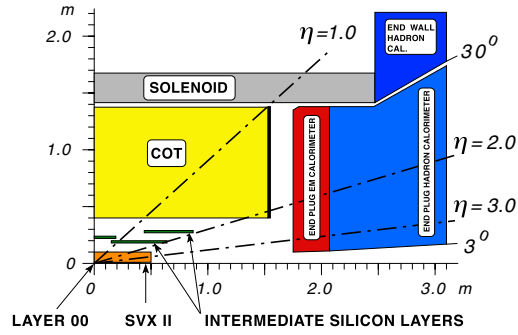


Figure 4.7. Schematic drawing of the  $r - z$  section of the CDF Run II detector.

## Silicon Vertex Detector (SVXII)

In Run I, for the first time in a hadronic machine, a silicon detector was used for the vertex reconstruction and tracking. This device, was crucial for heavy flavor detection and made possible the observation of the top quark and the measurement of its mass, as well as a wealth of  $b$  physics studies previously unfeasible in hadron colliders.

In Run II the overall vertex detector was redesigned to deal with the higher luminosity and the shorter bunch crossing with respect to Run I. This upgrade was also intended to allow the determination of precise 3D track impact parameters over a wider acceptance range. This capability is crucial to provide  $b$ -tagging for studies of top production, supersymmetry searches and the search for the Higgs boson. SVX II and the associated trigger upgrades are also of great benefit to the CDF  $B$  physics program. Other features of SVX II are the improvement of the purity and efficiency of the tracking, in particular stereo tracking, and of the angular acceptance.

The SVX II is a silicon microstrip detector, made by thin silicon wafers. On the wafer surface several narrow lines of impurity atoms are implanted to form closely spaced strips. Diode junctions are thus created between the wafer and the strips. Applying a voltage with the proper polarity to the diode increases the depletion depth. The depletion junction, a free charges zone with strong electric field, is the actual sensitive region of the microstrip detector. When an ionizing particle passes through this region electrons are promoted to the conduction band which generates an electrical signal on few strips. The strips are then read out by fast electronics revealing, to within a fraction of the strip spacing, where the particle intercepted the wafer along one dimension.

The whole detector coverage along  $z$  is driven by the spread of the primary interaction along this axis. The interactions are distributed approximately as a gaussian along the beam ( $z$ ) direction, with an average standard deviation of  $\sim 30$  cm. To provide a geometrical acceptance greater than 70% the length of SVX II is

$\sim 45$  cm on both side of the nominal interaction point. The pseudorapidity coverage is  $|\eta| < 2$ . SVXII is characterized by 12-fold symmetry in  $\phi$  and consists of three 32 cm long cylindrical barrels, with 5 layers each. These layers consist of double side silicon wafers (ladders) mounted with staggered radii to provide some overlap between adjacent ladders. The innermost layer is placed at a radius of 2.4 cm, while the outermost is at a radius of  $\sim 10.7$  cm. Three of the 5 layers have on one side the microstrips aligned to the beam while on the other side orthogonal, the remaining two have instead the strips on the two side with a small-angle stereo. These strips are spaced in  $r\phi$  by approximately 60 to 65 microns, depending on layer, and have implant widths of 14 to 15 microns. The stereo strips of the SVX II are spaced by (141, 125.5, 60, 141, 65) microns, and have implant widths of 20 microns for the  $90^\circ$  strips and 15 microns for the small-angle stereo layers. This design allows both a good resolution on the z-position of secondary vertices and an enhanced 3D pattern recognition. The length of each ladder is 29 cm, each divided into two half-ladders that are read out independently. The readout electronics consists of hybrid chips that are mounted directly to the silicon surface at each end of the half-ladder. The choice of electronics located on the silicon sensors was made to fulfill the requirement of a fast response and low occupancy detector. The electronics inside the detector implied the addition of material within the active sensitive volume like cables and cooling tubes. This increases the multiple scattering of a particle worsening the pattern recognition capability. To partially mitigate this effect another layer of silicon at small radius (Layer 00) was added to SVX II.

### **Layer 00 (L00)**

L00 is a radiation tolerant, single-side axial-strip silicon layer, placed immediately outside the beam pipe at  $R \sim 1.5$  cm. Being so close to the interaction region L00 is expected to improve noticeably the impact parameter resolution from  $50\mu\text{m}$

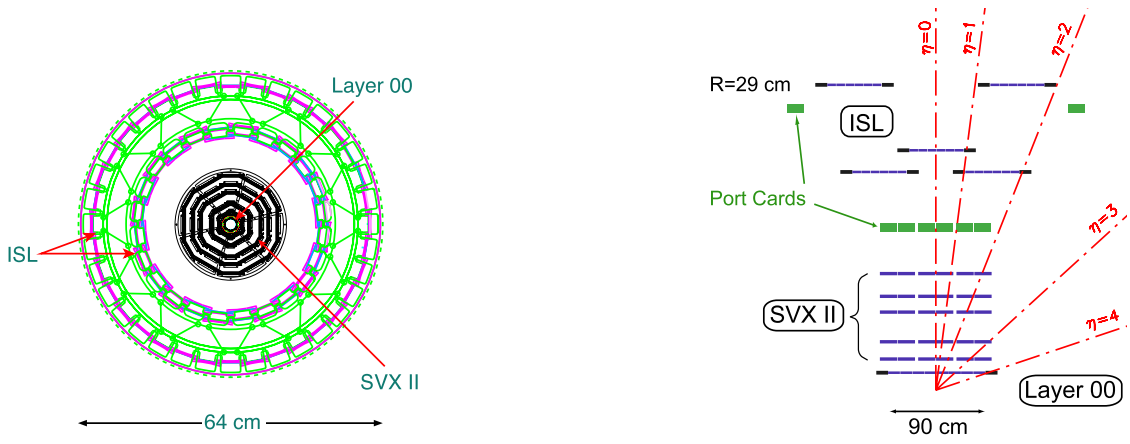


Figure 4.8. Schematic  $r - \phi$  (left) and  $r - z$  (right) views the Run II CDF silicon detector.

to roughly  $25\mu\text{m}$ . The improvement of impact parameter resolution leads to a substantial improvement in  $b$ -tagging performance.

### Intermediate Silicon Layers (ISL)

The Intermediate Silicon Layers were designed both to improve the tracking capabilities in the region  $|\eta| < 1$  where tracks are based on the SVX II and on the COT, and to allow silicon stand alone tracking outside the COT  $\eta$  coverage. In the central  $\eta$  region the ISL consists of a single layer of silicon placed at a radius of 22 cm, while in the forward one ( $1.0 < |\eta| < 2.0$ ), where the COT coverage is incomplete or missing, it has two layers of silicon at radii of 20 cm and 28 cm.

The ISL was developed using many features already studied for the SVX II. For example the data acquisition, power supplies and cooling system are nearly the same for these two detectors. Nevertheless the large surface area of silicon needed by the ISL required some simplification of the SVX II technology to minimize the subdetector cost. The lower occupancy and the lower radiation damage, allowed the use of longer strips and wider readout pitch. This directly reflects in a smaller

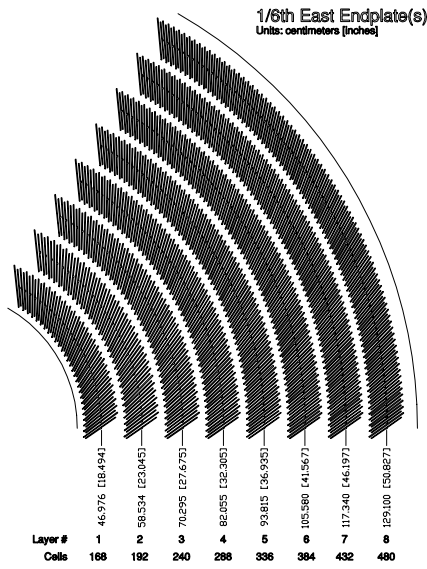


Figure 4.9.

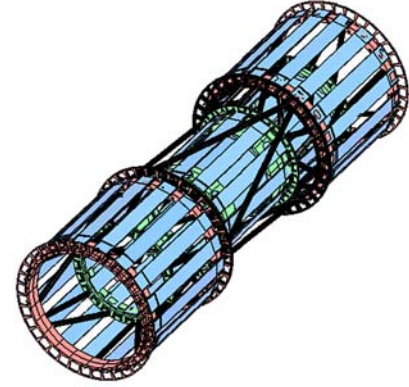


Figure 4.10. Intermediate Silicon Layer

number of readout channels and chips reducing the cost of the frontend electronics and data acquisition.

The basic ISL unit is the ladder. Each ladder is made of three silicon detectors bonded together to form a single electrical unit. The readout hybrids are not mounted on silicon like SVX II, but they are glued onto the edge of the mechanical support. Two ladders are paired to form a module  $\sim 55$  cm long. A silicon sensor consists of double-sided microstrip detectors with axial strips on one side and small angle stereo strips on the other. To reduce the number of channels the readout pitch is twice the strip pitch. The intermediate strips are not read out but they still contribute to the resolution through charge sharing.

## Central Outer Tracker (COT)

The COT detector is an open cell drift chamber, placed immediately after ISL in a region between the radii of 40 and 138 cm from the beam pipe. It consists of

Resolution	COT	COT + SVXII + ISL
$\delta p_T/p_T^2[(GeV/c)^{-1}]$	$3 \times 10^{-3}$	$1 \times 10^{-3}$
$\delta d[\mu\text{m}]$	600	30
$\delta z_0[\mu\text{m}]$	$5 \times 10^3$	30
$\delta \cot\theta$	$6 \times 10^{-3}$	$4 \times 10^{-3}$

Table 4.1

Resolution on various track parameters as obtained by the COT and by the COT + SVXII + ISL.



eight superlayers which cover the  $|\eta| < 1$  region. Each superlayer groups 12 planes of sense wires alternated with layers of potential wires. To reconstruct tracks in three dimensions, four of the eight superlayers (axial) have wires along the axial direction, while the remaining four (stereo) have wires tilted of  $\pm 3^\circ$  with respect to the axial direction; the superlayers are alternated starting with a stereo superlayer.

To cope with the high luminosity and the event pile-up keeping the device occupancy to reasonable values, the cell size was reduced by a factor of four with respect to Run I. Moreover the chamber is filled with a mixture of Argon and Ethane in proportions of 50:50, which, with a drift velocity of  $\sim 100\mu m/ns$ , ensure a faster response of the COT.

#### **4.2.2 The Time of Flight Detector**

The CDF II detector has been equipped with a Time Of Flight(TOF) detector dedicated to particle identification. It is placed immediately outside the tracking system, and it consists of scintillator bars 3 meters long which cover the COT active volume. The thickness of these bars (4 cm) is constrained by the limited space between the COT and the solenoid, while the width (4 cm) has been determined by resolution and occupancy studies.

A particle reaching the TOF detector produces scintillation light which is collected by photomultiplier tubes attached to both sides of each bar. The pulse-height signal collected, is used in coincidence with the  $T_0$  of the event, to determine the time interval between the production and the detection of the particle. Moreover this signal gives a measurement of the  $z$  coordinate of the particle on the TOF detector.

This device is of particular importance in B physics, for which it is used to discriminate between protons, kaons and pions.

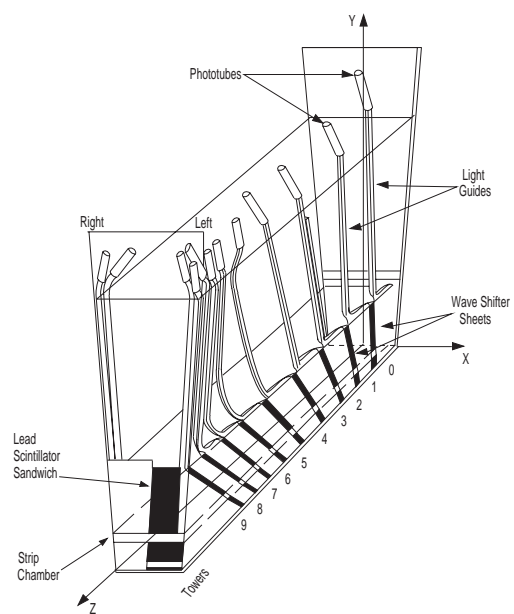


Figure 4.11. Perspective view of a CEM module.

### 4.2.3 The Calorimetry System

The CDF calorimetry system, located immediately outside the solenoid, is devoted to measure the energy and the direction of neutral and charged particle escaping the tracking region.

The calorimetry is designed to absorb these particles degrading their energy through electromagnetic and hadronic interactions. It is organized into two subsystems: the inner electromagnetic and the outer hadronic section, optimized to better react, respectively, to electromagnetic and hadronic interacting particles. Both the subsystems are segmented in towers, which, projecting toward the centre of the detector, providing spatial information on the particle direction. Each tower consists of layers of passive material alternated with scintillator tiles. Particles, gradually absorbed by the passive material, leave a signal in the scintillators which is read by means of wavelength shifters (WLS) and carried through light guide to photomultiplier tubes. The CDF calorimetry systems, divided in central ( $|\eta| < 1.1$ ) and forward ( $1.1 < |\eta| < 3.64$ ) regions, is described in the following sections.

#### Central Calorimeter

The Central Calorimeter, apart from some upgrades on the readout electronics to match the time requirements imposed by Run II, has been recycled from Run I.

It consists of two halves joined at  $\eta = 0$ , which cover the central region  $|\eta| < 1.1$ .

The Central ElectroMagnetic (CEM) subsystem is a sampling calorimeter made of lead sheets separated by polystyrene scintillator. Each half is organized in 24 wedges in  $\phi$ , subtending an angle of  $15^\circ$ . Each wedge is segmented with steps of  $\Delta\eta = 0.11$  in 10 projective towers.

Behind the CEM are placed the Central and the End Wall Hadronic calorimeters (respectively CHA and WHA). The last subsystem is intended to cover the gap between the central and the plug hadronic sections. The transverse segmentation of the hadronic calorimeter is designed to match the geometry of the CEM. Towers,

<b>Electromagnetic Calorimeter</b>		
	Central	Plug
Thickness	$19 X_0, 1\lambda$	$21 X_0, 1\lambda$
– per sample(abs.)	$0.6 X_0$	$0.8 X_0$
– per sample(scint.)	5 mm	4.5 mm
Light yield	160 p.e. / GeV	300 p.e. / GeV
Stochastic resolution	$11.6 \% / \sqrt{E[GeV]}$	$14 \% / \sqrt{E[GeV]}$
Sampling resolution	$14 \% / \sqrt{E[GeV]}$	$16 \% / \sqrt{E[GeV]}$
<b>Hadronic Calorimeter</b>		
	Central	Plug
Thickness	$4.5 \lambda$	$7 \lambda$
– per sample(abs.)	1 in (central) 2 in (end wall)	2 in
– per sample(scint.)	6 mm	6 mm
Light yield	40 p.e. / GeV	39 p.e. / GeV
Resolution	$75\% / \sqrt{E[GeV]} \oplus 3\%$	$80\% / \sqrt{E[GeV]} \oplus 5\%$

Table 4.2  
Characteristic of the CDF II calorimeter.

made of acrylic scintillator sandwiched between iron sheets, use a readout scheme similar to the one used in CEM.

To increase the spatial resolution of the calorimeter two proportional chambers are embedded in each wedge of CEM. The Central Electromagnetic Strip chamber (CES), placed 5.9 radiation lengths ( $X_0$ ) deep in the EM towers, consists of wires in the  $r - \phi$  plane and cathode strips in the  $z$  direction. It measures the charge deposition in correspondence of the maximum electromagnetic shower development. The pulse-height and the tridimensional spatial position of this signal allow a better reconstruction of electromagnetic objects.

The Central Pre Radiator (CPR) wire chamber, occupying the interspace between the magnetic coil and CEM, acts as a shower presampler. This detector is a very useful tool in the pion-photon discrimination.

Although the signal coming from both these wire chambers has to be integrated over several beam crossing, this turns out not to be a problem thanks to the low occupancy of this devices ensured by their granularity.

## **Plug Calorimeter**

The plug calorimeter, which extends from  $|\eta| > 1.1$  to  $|\eta| < 3.64$ , substitutes the Run I gas calorimeters. The new calorimeter, based on similar design as the central one, consists of a lead-scintillator electromagnetic section followed by an iron-scintillator hadronic section.

The electromagnetic calorimeter contains an embedded Shower Maximum Detector (SMD) placed at a radial depth of  $\sim 6X_0$ . This device consists of 16 detector sectors each covering  $45^\circ$  in  $\phi$ , with two layer of strips per sector. To keep the occupancy acceptable each sector is divided in two segments in pseudorapidity.

In addition the first layer of the electromagnetic calorimeters can be read out separately acting as a pre-shower detector.

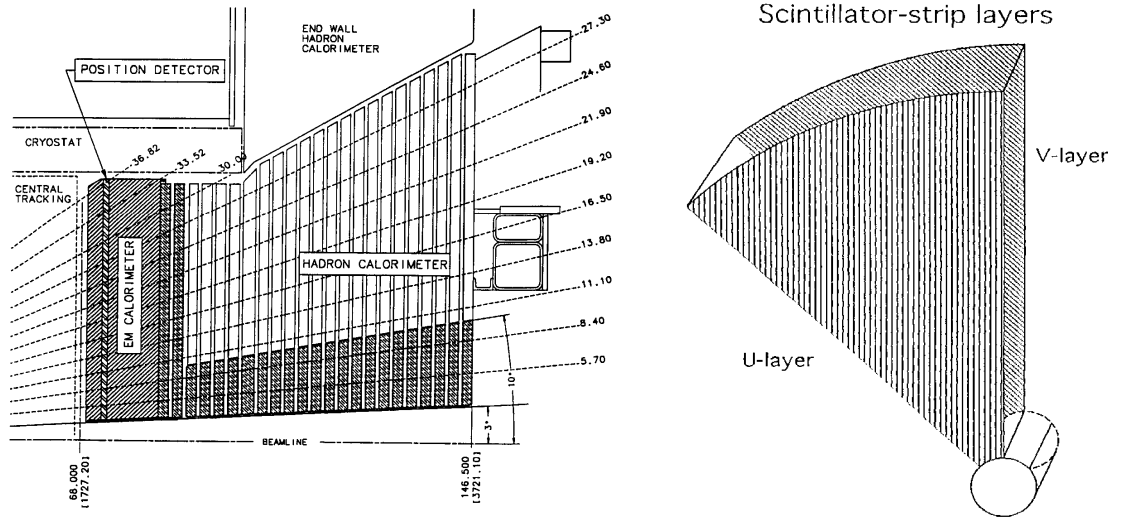


Figure 4.12.  $r - z$  view of the plug calorimeter (left), and the SMD module (right).

The active elements of both the calorimeters are scintillating tiles, which are arranged in projective towers. Groups of 48 or 28 towers (for  $|\eta| < 2.11$  and  $|\eta| > 2.11$ ) are organized in 12 concentric  $\eta$  sectors, with  $\eta$  ranging from 0.1 to 0.64 according to the increasing pseudorapidity.

As in the central calorimeter the active elements are read out using wavelength shifter, optical cables then route the light from the tiles to the photomultiplier tubes. Each photomultiplier collects the light from the whole tower

#### 4.2.4 Muon Detection

The last device surrounding the whole CDF II detector is the muon system. Thanks to their high penetration power muons can escape the calorimeter reaching the muon chambers, while all the other particles are absorbed in the inner detectors.

The muon system is organized into 4 subsystems which cover different  $\eta$  regions, allowing triggering and identification of muons up to  $|\eta| < 1.5$ . Each subdetector consists of several layers of active material where the muon signal is collected. In two of the four subdetectors the active region is made of drift tubes, while the remaining two are equipped with scintillator bars.

#### 4.2.5 The Trigger and Data Acquisition System

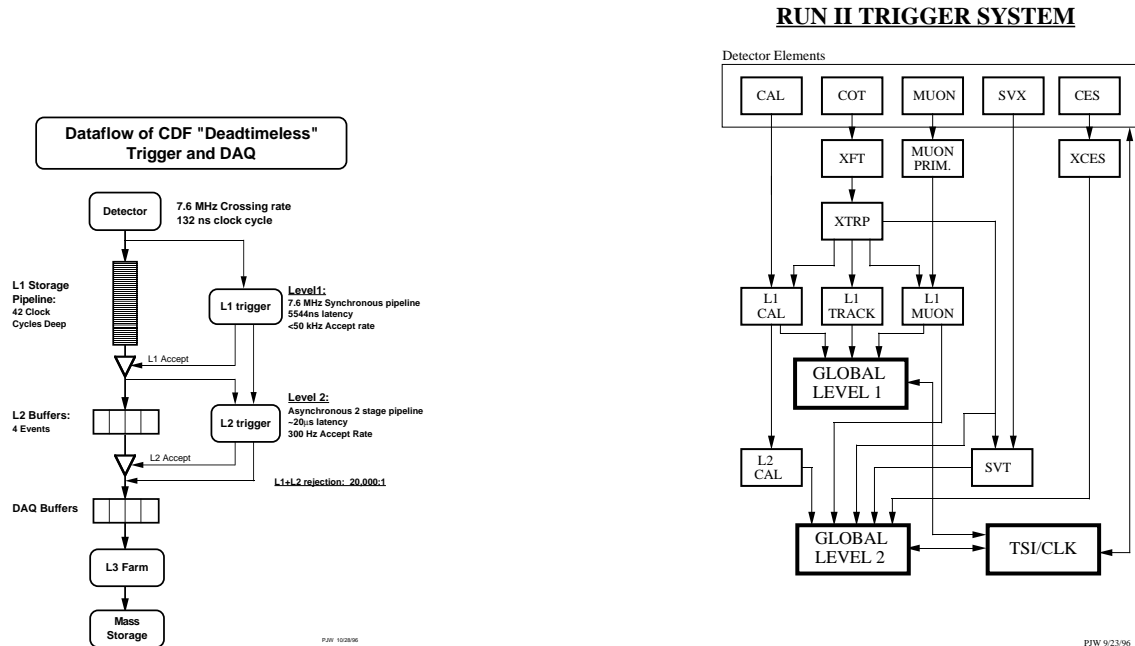


Figure 4.13. CDF pipelines and buffers trigger architecture (left).  
Block diagram of the Run II trigger system.

Trigger systems have crucial importance in hadron collider experiments. The collision rate, proportional to the huge  $p\bar{p}$  inclusive cross section, is in fact much higher than the rate data can be stored on tape. At CDF Run II the collision rate is of the order of 7 MHz, while the tape writing speed is limited to less than 70 events per second. The role of the trigger selection system is to effectively filter the physics events among the large amount of “minimum bias” background. As discussed in the

section 4.1.4 the clocking of the whole experiment has changed since Run I, and thus the trigger system had to be redesigned.

The CDF trigger system has an architecture based on three decision level. The rejection rate at each level is such that more sophisticated event processing is allowed at the next level with a minimum deadtime. In figure ?? .... is shown.... the main characteristics of the three trigger levels are detailed in the following.

## Level 1

The Level 1 trigger (L1) selection is based on a number of physics object (primitives) constructed from the raw detector signals. To guarantee enough time for transmission and processing of the informations coming from the various subdetectors, a L1 latency time of  $5.5 \mu\text{s}$  has been chosen. Each subdetector is equipped with a local data buffering system able to accommodate the 42 events expected during such a period. L1 primitives are constructed by means of dedicated hardware, designed to analyze signals from the calorimeters, tracking chambers and muon detectors.

The most significant upgrade with respect to Run I is the new hardwired algorithm of track finding named eXtremely Fast Tracker (XFT). XFT analyzes the COT signals, returning track  $p_T$  and  $\phi_0$  by means of  $r - \phi$  pattern recognition. This quantities are then used to better identify electron and muons, extrapolating and matching XFT tracks to calorimeter towers and to muon chambers. This task is performed by the designed unit XFTP.

The calorimeter informations used at level one, are the calorimeter towers grouped in pairs along  $\eta$  (trigger tower). Using the electromagnetic and the total transverse energy of these trigger towers, electron/photon and jets primitives are defined. Moreover using all the energy deposited in the trigger towers above 1 GeV the  $\cancel{E}_T$  is computed.

The maximum L1 accepted rate is  $\sim 20$  KHz, while the typical one is about 12 KHz.



## Level 2

Event accepted by L1 are then processed by the Level 2 trigger (L2). At this level event informations are collected into one of the four L2 buffers. When L2 is processing an event, the buffer where the event is stored is not accessible by L1; if all the four buffers are full the experiment incurs in downtime. To overcome this problem each separate L2 buffer is connected to a two-step pipeline each taking approximatively  $10\ \mu\text{s}$ . In the first step single detector informations are processed, which are subsequently combined at the second stage to take a trigger decision. In this way the downtime is less than 10% even at full L1 accepted rate.

At L2 all the L1 primitives are recalculated with higher precision. Moreover, to further reduce the accepted rate, the outcome of the trigger tower clustering is available, as well as the information on the impact parameter provided by the Silicon Vertex Tracker (SVT). SVT is an hardwired algorithm, implemented into dedicated processors, which for the first time in hadron collider experiment, allows to trigger on long living particles.

The typical L2 accepted rate is between 100 and 300 Hz, depending on the luminosity.

## Level 3

The Level 3 (L3) trigger is structured in two steps. First, for the events selected by L2, the informations from all the subdetectors are structured in one data block. This is then passed to the L3 Linux farm, where the whole event is reconstructed almost at the offline analysis level. Some variables like global event observables, might not be calculated due to the long processing time required. Then a trigger decision to whether or not store permanently the event is taken. Finally a trigger path is defined by making unique combination of L1, L2 and L3 requirements.



## 5. SUSY Signature and Current limits

In the mSUGRA scenario, the production cross section of chargino-neutralino,  $\sigma_{\tilde{\chi}_1^\pm \tilde{\chi}_2^0}$ , is dominant throughout most of the parameter space; this signal therefore would lead to the maximum reach of the Tevatron Collider experiments for SUSY. In particular, the fully leptonic decay mode of  $\tilde{\chi}_1^\pm$  and  $\tilde{\chi}_2^0$  is regarded as the most promising channel in the hadronic environment. The current mass limits of  $\tilde{\chi}_1^\pm$  and  $\tilde{\chi}_1^0$  are given here, together with a brief description of the event signature.

### 5.1 Current Limit

The Tevatron collider has been the high energy frontier since the first data taking in 1987; it is therefore the prime location to search for the missing constituent of the SM, the Higgs boson, and the evidence of new physics. Both experiments at the Tevatron, CDF and D0, did not discover any supersymmetric signal during the so called Run I (data taking from 1992 to 1995). However, the center of mass energy ( $\sqrt{s}$ ) of the machine is now increased (from Run I  $\sqrt{s} = 1.8$  TeV to Run II  $\sqrt{s} = 1.96$  TeV) leading to an enhancement in the cross section for producing heavy particles. The integrated luminosity is already twice as much as the total luminosity of Run I and the detector has undergone crucial upgrades (mainly improvement of the tracking capability and of the muon acceptance). The search for SUSY with the new Run II data is therefore promising. The question that arises is, which is the highest sensitivity channel.

As far as the the analysis is concerned, a signature based approach could be regarded as the appropriate one; it requires a good understanding of the building blocks of the SUSY event (usually, high  $p_T$  isolated leptons, photons,  $b$  and  $c$ -quarks and

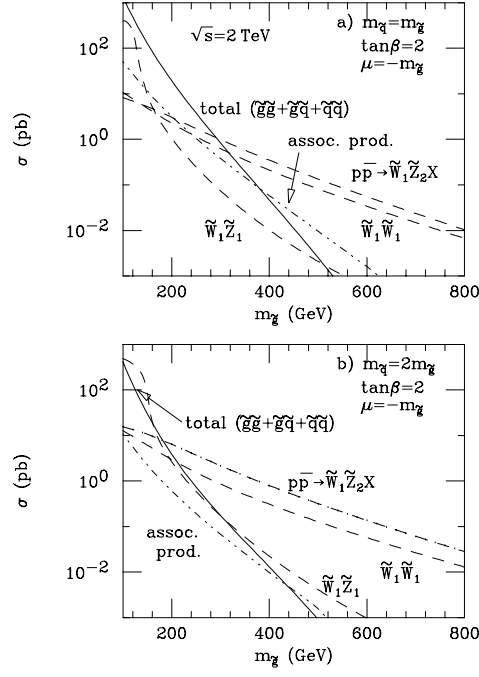


Figure 5.1. X.Tata, hep-ph/9706307: Total cross section for various *sparticle* production processes by  $p\bar{p}$  collisions at  $\sqrt{s} = 2$  TeV

missing transverse energy) and it provides an absolute limit or evidence. However, in setting the limits, it is usually necessary to select a model to reduce the number of free parameters; any limit will be model dependent. At a hadron collider the reference model is usually mSUGRA. In this scenario, *sleptons*,  $\tilde{\chi}_1^\pm$  and  $\tilde{\chi}_2^0$  are typically less massive than  $\tilde{g}$  and  $\tilde{q}$ ; therefore the cross section for producing chargino-neutralino dominates the strongly produced  $\tilde{q}\tilde{q}$ ,  $\tilde{g}\tilde{g}$  cross sections (Fig.(5.1)). Therefore the attention will be focused on any of the signals  $\tilde{\chi}_1^\pm \tilde{\chi}_1^0$ ,  $\tilde{\chi}_1^\pm \tilde{\chi}_1^\pm$ ,  $\tilde{\chi}_1^\pm \tilde{\chi}_2^0$  with a subsequent leptonic decay.  $W$  pair production, with a  $\sigma \sim 10$  pb at Tevatron, is the main background to  $\tilde{\chi}_1^\pm \tilde{\chi}_1^\pm$  event whereas  $\tilde{\chi}_1^\pm \tilde{\chi}_1^0$  is affected by  $W$  decaying into lepton-neutrino. The  $WZ$  production, with a  $\sigma \sim 1$  pb, is instead a possible source of background for the trilepton signature of  $\tilde{\chi}_1^\pm \tilde{\chi}_2^0$ . But these events should be distinguishable from the SUSY trilepton in that one lepton pair must reconstruct the  $Z$  mass (unless

the neutralino decays into the real  $Z$ ). SM trilepton events can also result from  $c\bar{c}$ ,  $b\bar{b}$ ,  $t\bar{t}$  followed by decays of heavy flavour; however, leptons from heavy quarks will be associated to hadronic activity and therefore they will be different from isolated trileptons. Hence, the isolated trilepton events associated to the chargino-neutralino production should be relatively background free without any high energetic jets. As a consequence, this mode is regarded as the “golden” channel at the Tevatron [14]. The status of the collider search for chargino and neutralino is dominated by the latest LEP2 results. No evidence of *superpartners* yields a lower limits for the mass of chargino and neutralino:

- $m_{\tilde{\chi}_1^\pm} > 103.5 \text{ GeV}$ ;
- $m_{\tilde{\chi}_1^0} > 59.5 \text{ GeV}$ ;

The lower limit on the neutralino is derived from the mass bound on the chargino within the mSUGRA Scenario. In Fig.(5.2) the exclusion region is indicated as a function of  $\tan\beta$  for different values of  $A_0$  and  $m_0 \leq 1 \text{ TeV}$ .

Within the mSUGRA scenario, the parameters  $m_0$  and  $m_{\frac{1}{2}}$  are the most important ones for fixing the scale of the *particle* masses. The  $m_0$ - $m_{\frac{1}{2}}$  plane, for fixed values of the other parameters, is therefore suited for a display of the constraints and of the parameter space region in agreement with the experimental data. Fig.5.3 shows the excluded region as a result of the LEP measurements with the parameter set:  $A_0 = 0$ ,  $\tan\beta = 10$ ,  $\text{sgn}(\mu) > 0$  [15]. The region at the left edge (yellow) is excluded because either the EWS is not properly broken or  $\tilde{\tau}_1$  is the LSP; the region at the right corner (yellow) is excluded because radiative EWSB does not occur. In the central bottom region (light blue), the values are inconsistent with the EW parameters of LEP1. The central area (green) is excluded by chargino searches, whereas the region above is not allowed by searches for  $h_0 Z$ . The left margin (magenta or brown) sets of parameters are excluded by search for heavy stable charged particles and neutralino, respectively. A wide  $m_0 - m_{\frac{1}{2}}$  region has still to be investigated and might lead to the discovery of SUSY. The current run of the Tevatron could set the

capability to set more stringent limits on the mass of chargino and neutralino and therefore crucial bounds on the mSUGRA parameter  $m_{\frac{1}{2}}$ .

## 5.2 Signature of the event

At a hadron collider only a fraction of the total center of mass energy is used in *sparticle* production; this means that the hard scattering partonic cross section has to be convoluted with the parton distribution function. As far as chargino and neutralino are concerned, they are produced through the electroweak coupling to *squarks* and to vector bosons  $W$  and  $Z$ . In the assumption of R-parity conservation, there are three contributions to  $\tilde{\chi}_1^\pm \tilde{\chi}_2^0$  production:

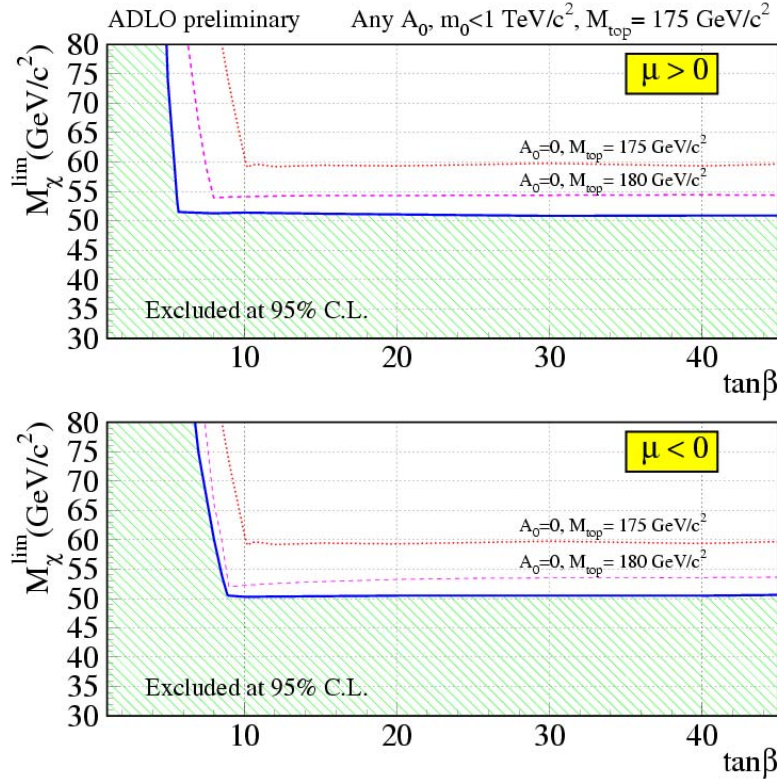


Figure 5.2. LEP-SUSY working group: lower limit on the lightest neutralino mass

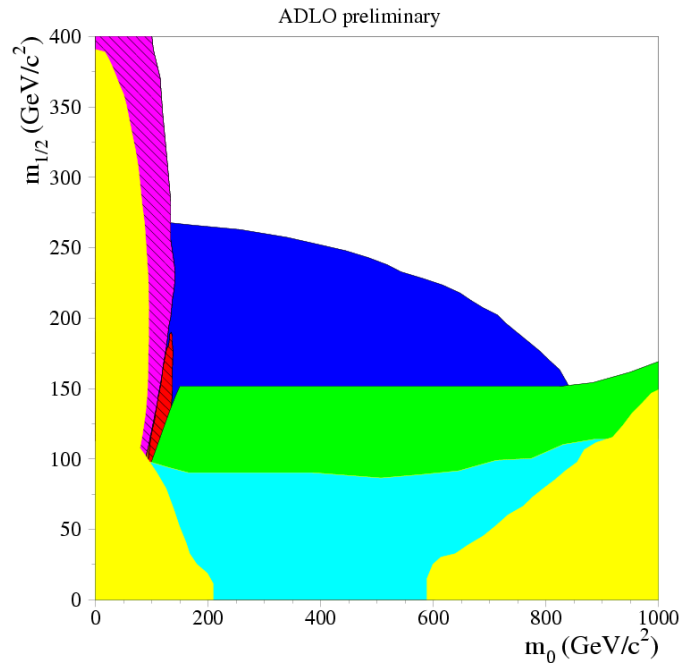


Figure 5.3. LEP-SUSY working group:excluded region in the  $m_0$ - $m_{\frac{1}{2}}$  planes for fixed  $\tan\beta \operatorname{sgn}\mu$  and  $A_0$

- s-channel gauge boson production
- t-channel *squark* exchange
- interference

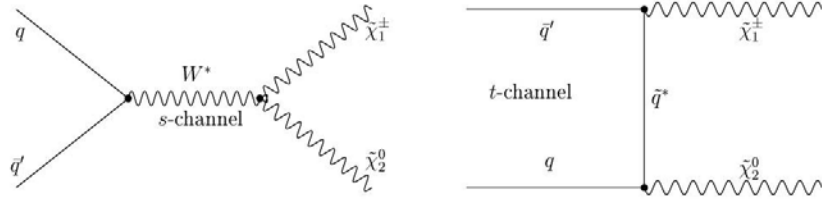


Figure 5.4. Chargino-Neutralino associated production at  $p\bar{p}$  collider

In the first case, the reaction  $q\bar{q}' \rightarrow W^* \rightarrow \tilde{\chi}_1^\pm \tilde{\chi}_2^0$  occurs through the wino and higgsino components of the neutralino and chargino respectively. In the second

production mode, the right-handed *squark* couples only to the bino components of neutralinos while the left-handed *squark* couples to both the bino and wino components of neutralino and chargino. Any left or right handed *squark* coupling to the higgsino component is proportional to the corresponding quark mass and it can be discarded for chargino neutralino pair production. Since the higgsino and gaugino components of both chargino and neutralino are model dependent, the production cross section will be affected by the mSUGRA parameters.

Similarly to the production cross sections, the decay patterns for the charginos and neutralinos are also model dependent. If the masses of the decaying particles are high, the 2-body mode is allowed and kinematically preferred since the 3-body decay has an extra factor  $g^2/(4\pi^2)$  in the decay rate. The dominant 2 body decay modes for the chargino  $\tilde{\chi}_1^\pm$  are:

- $\tilde{\chi}_1^\pm \rightarrow W^\pm \tilde{\chi}_1^0$
- $\tilde{\chi}_1^\pm \rightarrow l\tilde{\nu}$
- $\tilde{\chi}_1^\pm \rightarrow \tilde{l}\nu$
- $\tilde{\chi}_1^\pm \rightarrow q\tilde{q}'$

When the 2 body mode is not kinematically allowed, the chargino decays to a 3 body final state with contributions similar to those for 2 body chargino decay: (i) virtual gauge boson decay, (ii) virtual *sfermion* decay, and (iii) interference. The final state for a 3 body decay is therefore:

- $\tilde{\chi}_1^\pm \rightarrow f\bar{f}'\tilde{\chi}_1^0$

where  $f$  and  $f'$  are fermions from the same  $SU(2)$  doublet. If *sfermions* are much heavier than the chargino, then (i) dominates, and the decays proceed through  $W^*$  with branching ratios similar to those of the on-shell  $W$  boson.

Similarly to the case of  $\tilde{\chi}_1^\pm$ , the  $\tilde{\chi}_2^0$  decay modes are dominated by the 2-body mode if kinematically allowed:



- $\tilde{\chi}_2^0 \rightarrow Z\tilde{\chi}_1^0$
- $\tilde{\chi}_2^0 \rightarrow \tilde{l}l$
- $\tilde{\chi}_2^0 \rightarrow \nu\tilde{\nu}$
- $\tilde{\chi}_2^0 \rightarrow q\tilde{q}$
- $\tilde{\chi}_2^0 \rightarrow h_0\tilde{\chi}_1^0$

while the 3 body decays, through virtual  $Z$ , virtual *slepton* or virtual *squark* gives:

- $\tilde{\chi}_1^0 \rightarrow f\bar{f}\tilde{\chi}_1^0$ .

Unlike the chargino and the  $W$ , the decay pattern of the neutralino is not similar to the real  $Z$ . The reason is that the  $Z$  couples only to the Higgsino component of the neutralino; as a result if the neutralinos in the decay  $\tilde{\chi}_2^0 \rightarrow \tilde{\chi}_1^0 f\bar{f}$  has a small Higgsino component, the  $Z$  contribution is strongly suppressed and the one of the *sfermions* is comparable in size.



## 6. Investigation of the parameter space

The overall efficiency of the  $\tilde{\chi}_1^\pm \tilde{\chi}_2^0$  production followed by the decay into leptons is set by the production cross section,  $\sigma_{\tilde{\chi}_1^\pm \tilde{\chi}_2^0}$ , and the branching ratio,  $BR(\tilde{\chi}_1^\pm \tilde{\chi}_2^0 \rightarrow ll + \cancel{E}_T)$ , which are both highly model dependent. For a given model, they dramatically depend upon the set of parameters. Having assumed the mSUGRA as the reference scenario at the hadron collider, we must determine which set of parameters yields the highest sensitivity. Such a question leads to the investigation<sup>1</sup> of the parameter space, namely the study of so called “slopes”<sup>2</sup> or points.

The SPS (Slopes and Points which arose at 2001 “Snowmass Workshop on the Future of Particle Physics”) are a set of benchmark scenarios regarded as the recommended slopes for future studies in SUSY [16]. In particular, “Slope 1a” is defined by the following values at the GUT scale:  $m_{\frac{1}{2}}$  free parameter,  $m_0 = 0.4 \cdot m_{\frac{1}{2}} = -A_0$ ,  $\tan\beta = 10$  and  $\mu > 0$  within the mSUGRA model. Fig. 6.1 shows the behavior of the  $\tilde{\chi}_1^\pm$ ,  $\tilde{\chi}_2^0$  and SM Higgs mass versus  $m_{\frac{1}{2}}$ ; as expected from the GUT assumptions,  $\tilde{\chi}_1^\pm$  mass is almost the same as the mass of  $\tilde{\chi}_2^0$  and all masses are proportional to  $m_{\frac{1}{2}}$  (Eq. (3.17)). According to Eq. (3.19), the right handed *sleptons*,  $\tilde{e}_R$  and  $\tilde{\mu}_R$ , are usually heavier than the chargino  $\tilde{\chi}_1^\pm$  but lighter than the corresponding left handed *slepton* since they only interact by hypercharge  $Y$  whereas the left handed *sleptons* are also affected by the  $SU(2)_L$  interaction. As far as the third family is concerned, the mass is decreased due to the Yukawa interaction which also mixes the left and

---

<sup>1</sup>The investigation of the parameter space is performed by a package developed in the CDF environment; this tool, which has been validated and improved, translates the physical hypothesis into mass spectra and coordinates the generators that are used to evaluate the production cross sections and the branching ratio of the processes of interest. Namely, ISAJET version 7.51 and PYTHIA version 6.203.

<sup>2</sup>Slope means simulation of the parameter space while one of the parameters is free and the others are either fixed or proportional to the free one

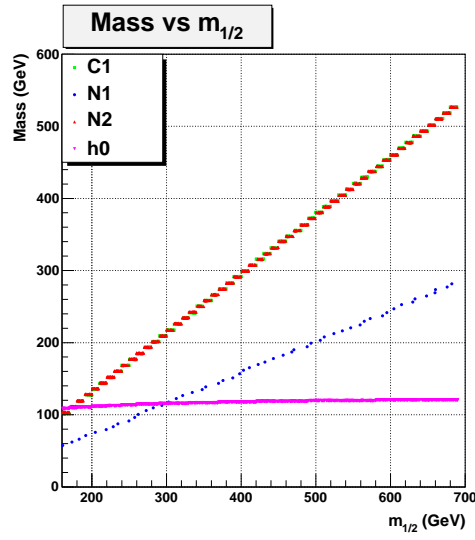


Figure 6.1. ISAJET:  $\tilde{\chi}_1^\pm$ ,  $\tilde{\chi}_2^0$  and SM Higgs mass vs  $m_{1/2}$

right components: being the mixing proportional to the mass of the corresponding fermion, it is usually neglected in the case of the first two families (almost degenerate) but it reduces the mass of lightest  $\tilde{\tau}$  ( $\tilde{\tau}_1$ )<sup>3</sup>.

All results have been cross checked by generating the same “events” within PYTHIA and no major differences are observed between the two generators. Actually, ISAJET and PYTHIA have been modified to call the same routine, SUGRA, to calculate all masses but the *sneutrinos* mass. This explains why the *sneutrino* sectors is slightly different between the two generators<sup>4</sup>, as shown in Fig. (6.3) and Fig. (6.4).

The cross sections for chargino neutralino associated production at  $\sqrt{s} = 2$  TeV have been calculated at LO using PYTHIA since PROSPINO doesn not include this

<sup>3</sup>Similarly for the third family of *squarks*:  $\tilde{t}_R$  receives top quark Yukawa corrections from both the charged and the neutral Higgs (while the corresponding  $\tilde{t}_L$  from the neutral Higgs only) moreover the mixing of the left  $\tilde{t}_R$  and right  $\tilde{t}_L$  makes the  $\tilde{t}_1$  the highest *sfermion*

<sup>4</sup>In PYTHIA, the three families are degenerate and the common value of the mass is the same as the  $\tilde{\nu}_\tau$  mass as calculated by ISAJET; on the other hand, just the first and the second family are degenerate in ISAJET and they are usually heavier than the third family

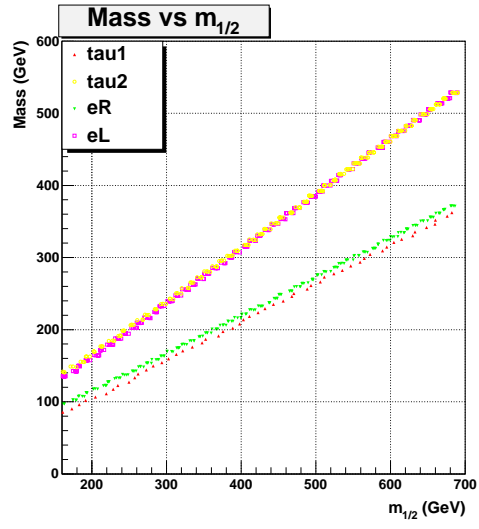


Figure 6.2. ISAJET: *sleptons* mass vs  $m_{\frac{1}{2}}$

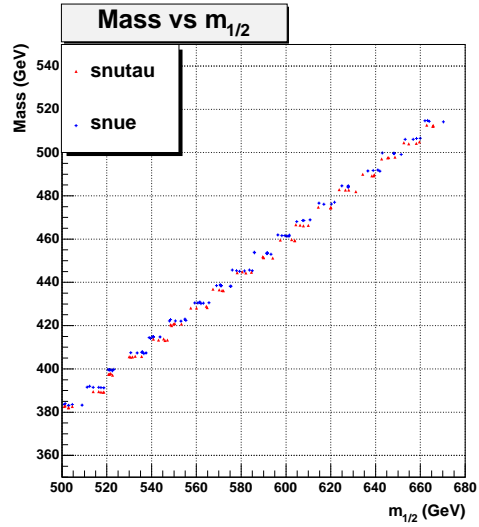


Figure 6.3. ISAJET: *sneutrinos* mass vs  $m_{\frac{1}{2}}$

process<sup>5</sup>. However, the corrections would enhance the production cross section by about 10-40 ( [17]), therefore the trilepton rate that will be calculated at the end

---

<sup>5</sup>A newer version of PROSPINO FORTRAN program including the NLO calculations for  $\sigma_{\tilde{\chi}_1^\pm \tilde{\chi}_2^0}$  will be released in few months by the author

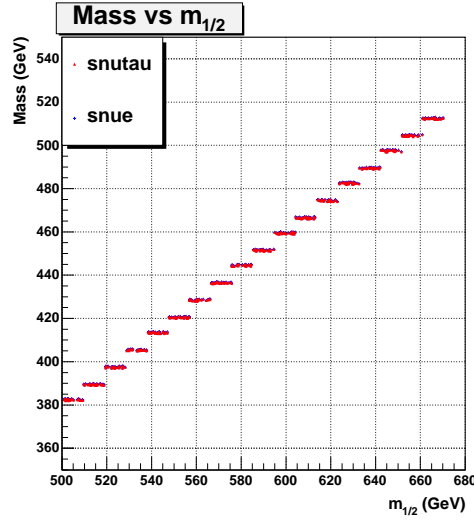


Figure 6.4. PYTHIA: *sneutrinos* mass vs  $m_{\frac{1}{2}}$

may be an underestimate. Fig. (6.5) and Fig. (6.6) compare the cross section for the associated production of  $\tilde{\chi}_1^\pm \tilde{\chi}_2^0$  to the  $\tilde{q}\tilde{q}$ ,  $\tilde{q}\tilde{q}'$  and  $\tilde{g}\tilde{g}$  cross sections. It is worth noticing that  $\sigma_{\tilde{\chi}_1^\pm \tilde{\chi}_2^0}$  is the highest production cross section in the region of investigation therefore enhancing the signal sensitivity. As expected,  $\sigma_{\tilde{\chi}_1^\pm \tilde{\chi}_2^0}$  decreases as  $m_{\frac{1}{2}}$  increases, being  $m_{\frac{1}{2}}$  proportional to both  $\tilde{\chi}_1^\pm$  and  $\tilde{\chi}_2^0$  mass. It would be the highest at the resonance, *via* real  $W$  and  $Z$ , but the corresponding regions have been already excluded by LEP; nevertheless,  $\sigma_{\tilde{\chi}_1^\pm \tilde{\chi}_2^0}$ , while suppressed from the resonant value, can still be  $\sim 1$  pb. In particular,  $\sigma_{\tilde{\chi}_1^\pm \tilde{\chi}_2^0}$  dominates over  $\tilde{\chi}_1^\pm \tilde{\chi}_1^0$  production cross section whereas, the  $\tilde{\chi}_1^\pm \tilde{\chi}_1^\pm$  process is discarded due to the high  $WW$  associated background.

Aside from the dependance on the  $\sigma_{\tilde{\chi}_1^\pm \tilde{\chi}_2^0}$ , the trilepton signal is determined by the branching ratio for chargino and neutralino into leptons,  $BR(\tilde{\chi}_1^\pm \tilde{\chi}_2^0 \rightarrow lll + \cancel{E}_T)$ . Once the *particles* are produced they decay through a cascade of decays that terminates with the production of the LSP (under the assumption of R-parity conservation). For any range of parameter, assuming the mSUGRA as a supersymmetry breaking mechanism, the Higgs parameter  $\mu$  is usually larger than the mass of the  $SU(2)_L$

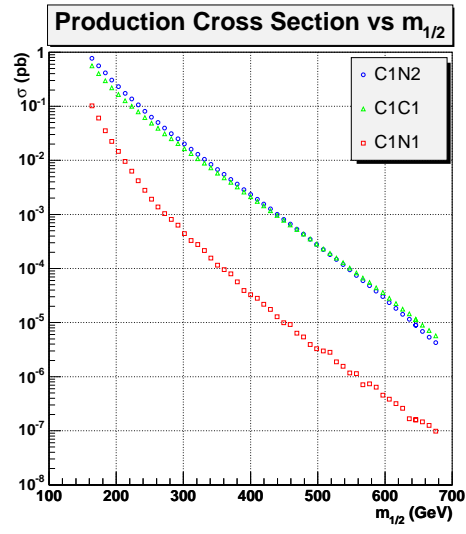


Figure 6.5. ISAJET: Production cross sections at  $E_{CDM} = 2$  TeV

gaugino,  $M_2$ ; this implies that the  $\tilde{\chi}_1^\pm$  and  $\tilde{\chi}_2^0$  are mainly gaugino like, being the higgsino component negligible. Therefore, the dynamical behavior is expected to be similar to the  $W$  and  $Z$  ones. In the low  $m_{1/2}$  region, the  $\tilde{\chi}_1^\pm$  branching ratio is

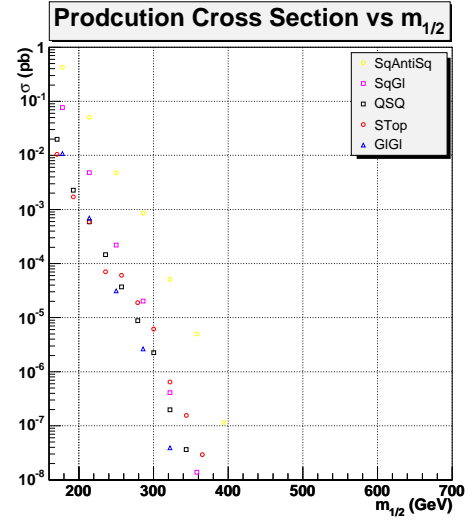


Figure 6.6. ISAJET: Production cross sections at  $E_{CDM} = 2$  TeV

dominated by the two body decay  $\tilde{\chi}_1^\pm \rightarrow \tilde{\tau}_1 \nu_\tau$ , associated to the left component of  $\tilde{\tau}_1$ , and the three body decay  $\tilde{\chi}_1^\pm \rightarrow f \bar{f}' \tilde{\chi}_1^0$  via  $W^*$ ,  $\tilde{l}^*$ ,  $\tilde{H}^*$ , as illustrated in Fig. 6.7, Fig. 6.8. The decay into left handed *slepton* is dynamically allowed but kinematically

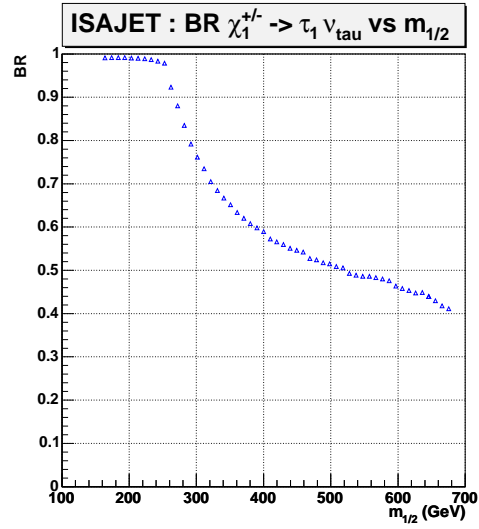


Figure 6.7. ISAJET: Decay channel  $\tilde{\chi}_1^\pm \rightarrow \tilde{\tau}_1 \nu_\tau$

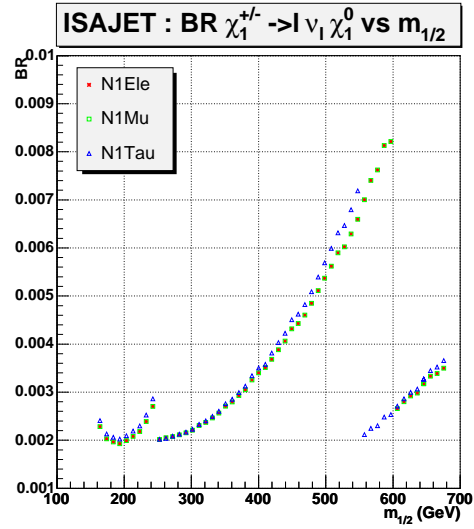


Figure 6.8. ISAJET: Decay channel  $\tilde{\chi}_1^\pm \rightarrow f \bar{f}' \tilde{\chi}_1^0$



forbidden for the first and second generation. As far as the three body decay is concerned, two discontinuities in the branching ratio are developed: at  $m_{\frac{1}{2}} \sim 240$  GeV, the channel  $\tilde{\chi}_1^\pm \rightarrow W \tilde{\chi}_1^0$  becomes kinematically allowed (Fig. (6.9)) and reduces both the three body mode and  $\tau_1$  decay; the lepton-*sneutrino* decay modes induce instead a drop in the branching ratio values at  $m_{\frac{1}{2}} \sim 600$  GeV depending on the *sneutrino* family. A slight difference between the values calculated by ISAJET and

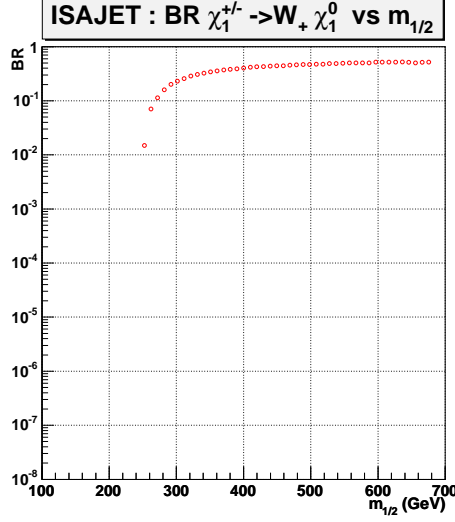


Figure 6.9. ISAJET: Decay channel  $\tilde{\chi}_1^\pm \rightarrow W \tilde{\chi}_1^0$

PYTHIA shows up in the branching ratio of chargino into *sneutrino*-lepton ( $e, \mu$ ) being the value higher when evaluated by PYTHIA due to the mentioned difference in the *sneutrino* mass.

Similarly to the  $\tilde{\chi}_1^\pm$  behavior, the branching ratio of the heavy neutralino  $\tilde{\chi}_2^0$  at low  $m_{\frac{1}{2}}$  is dominated by the two body mode  $\tilde{\chi}_2^0 \rightarrow l \tilde{l}$  and by three body decay. Actually, an enhancement in the branching ratio into different-sign leptons appears at  $m_{\frac{1}{2}} \sim 280$  GeV (Fig. (6.15)); this increase can be traced to the suppression of a negative interference between the exchange amplitudes for  $\tilde{\chi}_2^0 \rightarrow l^+ l^- \tilde{\chi}_1^0$  when the real  $Z$  mode opens. It might be expected that the neutralino decay is then dominated by

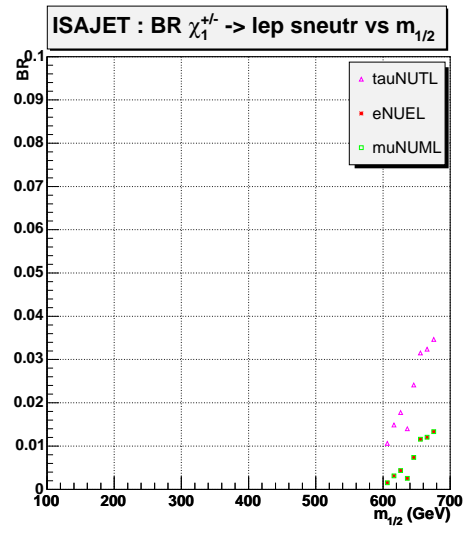


Figure 6.10. ISAJET: Decay channel  $\tilde{\chi}_1^{\pm} \rightarrow l \tilde{\nu}_l$

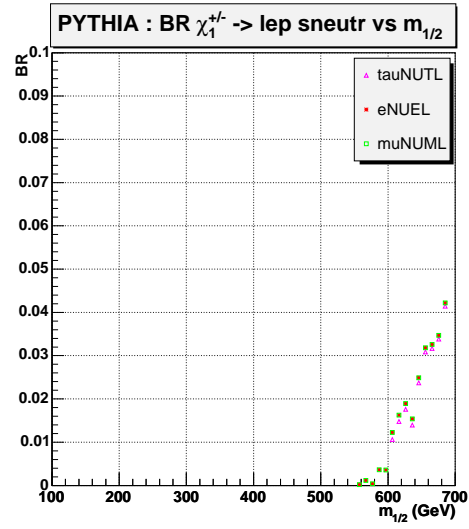


Figure 6.11. PYTHIA: Decay channel  $\tilde{\chi}_1^{\pm} \rightarrow l \tilde{\nu}_l$

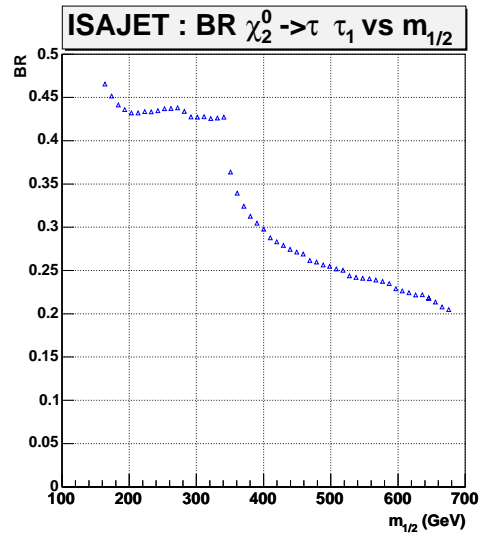


Figure 6.12. ISAJET: Decay channel  $\tilde{\chi}_2^0 \rightarrow \tilde{\tau}_1 \tau$

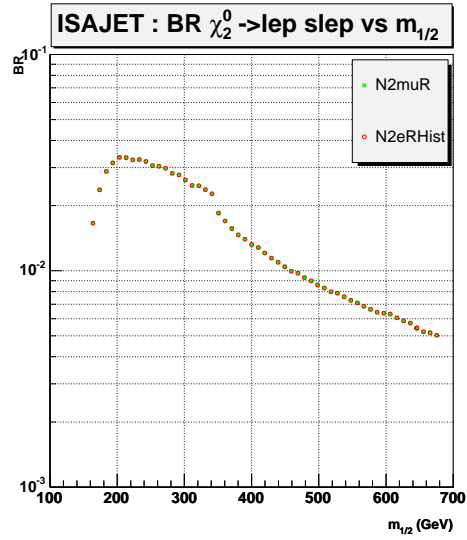


Figure 6.13. ISAJET: Decay channel  $\tilde{\chi}_2^0 \rightarrow l \tilde{l}$

the  $Z$  mode since the *sfermions* masses substantially exceed  $m_Z$ ; however, in contrast with the chargino, this does not occur since the Higgs parameter  $\mu$  is larger than  $M_2$

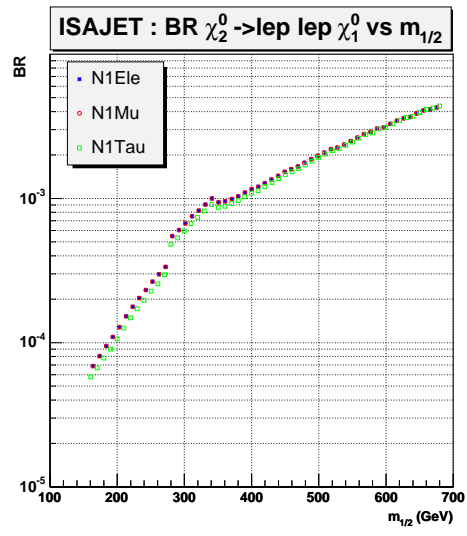


Figure 6.14. ISAJET: Decay channel  $\tilde{\chi}_2^0 \rightarrow l \tilde{\chi}_1^0$

and  $m_Z$  which implies a suppression of the coupling  $\tilde{\chi}_2^0 \tilde{\chi}_1^0 Z$  (both neutralinos have small higgsino components in the investigated range of parameters).

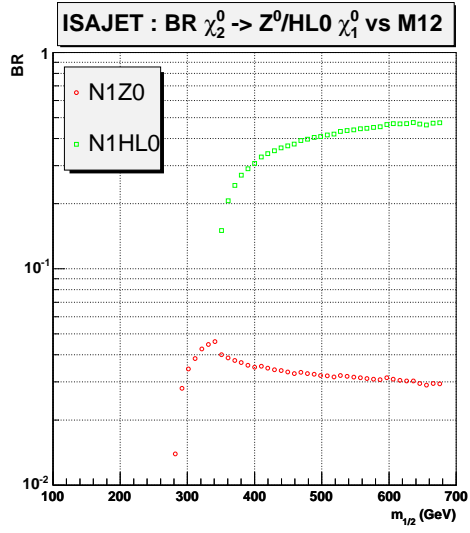


Figure 6.15. ISAJET: Decay channel  $\tilde{\chi}_2^0 \rightarrow W \tilde{\chi}_1^0$

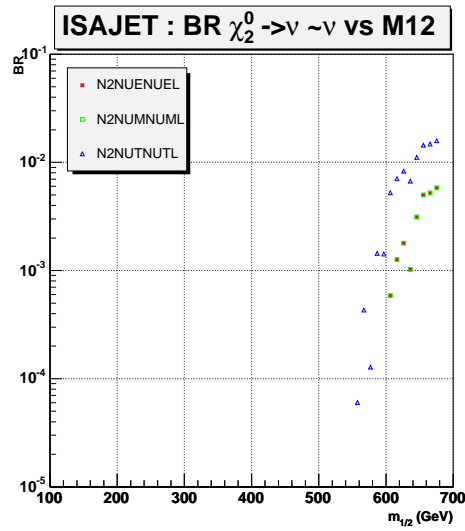


Figure 6.16. ISAJET: Decay channel  $\tilde{\chi}_2^0 \rightarrow \nu\tilde{\nu}$

Given the assumption of R-parity conservation, which is a feature of the mSUGRA model, any *sparticle* decays until the stable LSP is produced, as already mentioned. It is necessary thought to take into account the decay chain of *sleptons* and *sneutrinos* into lepton-LSP and neutrino-LSP respectively. These final products only have to be regarded as the observable objects at the experiment. Light *sfermions* decay into the LSP and the corresponding SM partner at almost 100%. If the *sfermions* are heavier such as *sneutrinos*, the decay mode *via*  $SU(2)_L$  coupling or *via* the smaller Y coupling might significantly affect the behavior. In this particular case, a family dependence appears: if ISAJET is actually adopted as generator, the first two families are degenerate while the third is lighter reducing the branching ratio to neutrino and LSP. For high values  $m_{1/2}$ , the branching ratio of  $\tilde{\nu}_\tau$  further decreases since the decay into  $\tilde{\chi}_1^\pm$  is enhanced (Fig. 6.17).

The expected rate for the production of hadronically clean trilepton event from the leptonic decay of  $\tilde{\chi}_1^\pm \tilde{\chi}_2^0$  pairs is presented in Fig. 6.18. There is no sum over the different configurations. For sake of simplicity, four cases are shown independently:

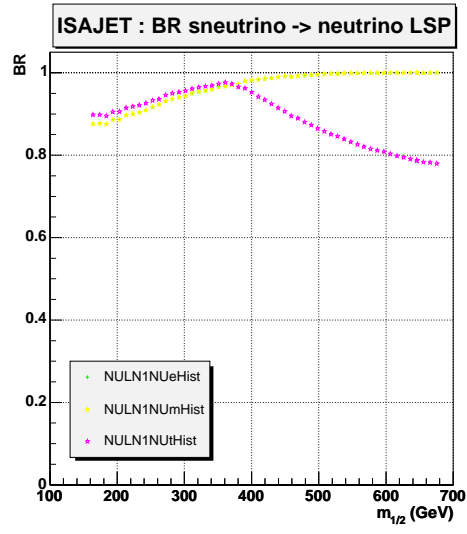


Figure 6.17. ISAJET: Decay channel  $\tilde{\nu} \rightarrow \nu \tilde{\chi}_1^0$

- $\tilde{\chi}_1^\pm \rightarrow l \tilde{\chi}_1^0$  and  $\tilde{\chi}_2^0 \rightarrow l^+ l^- \tilde{\chi}_1^0$
- $\tilde{\chi}_1^\pm \rightarrow l \tilde{\chi}_1^0$  and  $\tilde{\chi}_2^0 \rightarrow \tau^+ \tau^- \tilde{\chi}_1^0$
- $\tilde{\chi}_1^\pm \rightarrow \tau \tilde{\chi}_1^0$  and  $\tilde{\chi}_2^0 \rightarrow l^+ l^- \tilde{\chi}_1^0$
- $\tilde{\chi}_1^\pm \rightarrow \tau \tilde{\chi}_1^0$  and  $\tilde{\chi}_2^0 \rightarrow \tau^+ \tau^- \tilde{\chi}_1^0$

where  $l = e$  or  $l = \mu$ . The results calculated by ISAJET are in perfect agreement with the simulation performed by PYTHIA (Fig. 6.19). The accumulation of 500  $\text{pb}^{-1}$  of data by CDF at the current Tevatron run II yields an expected number of event shown in Figg. (6.20)-(6.23). These values have to be multiplied by the experimental efficiency to obtain the number of observable events at CDF. If referring to the exclusion limits derived from LEP2 results, the region which is still unexplored is associated to  $m_{\frac{1}{2}} > 270$  GeV, where the effective cross section dramatically drops with respect to the value at low  $m_{\frac{1}{2}}$  in case of leptons ( $e, \mu$ ). However the tri- $\tau$  signal is sizeable even at  $m_{\frac{1}{2}} > 270$  GeV, even taking into account a low experimental efficiency for detecting a  $\tau$  lepton.

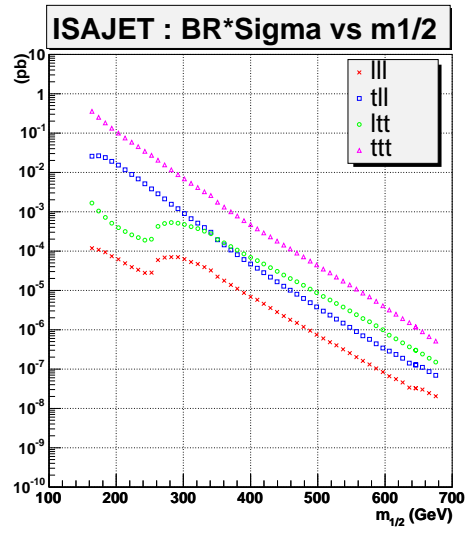


Figure 6.18. ISAJET: Effective production Cross section at  $\sqrt{s} = 2$  Gev

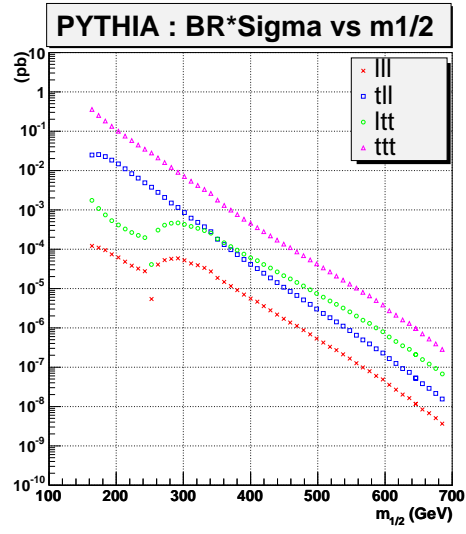


Figure 6.19. ISAJET: Effective production Cross section  $\sqrt{s} = 2$  Gev

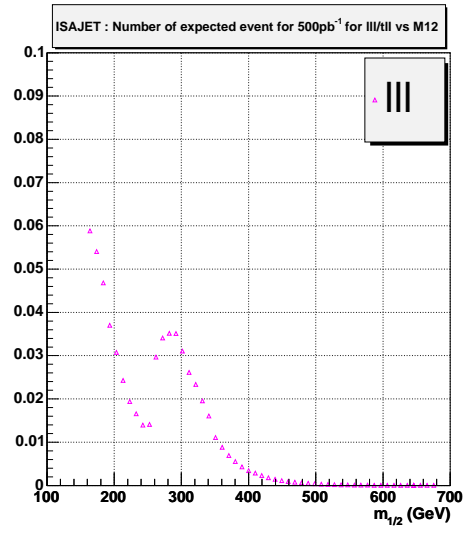


Figure 6.20. ISAJET: Number of generated tripleton events  $\sqrt{s} = 2$  GeV for 500 pb<sup>-1</sup>

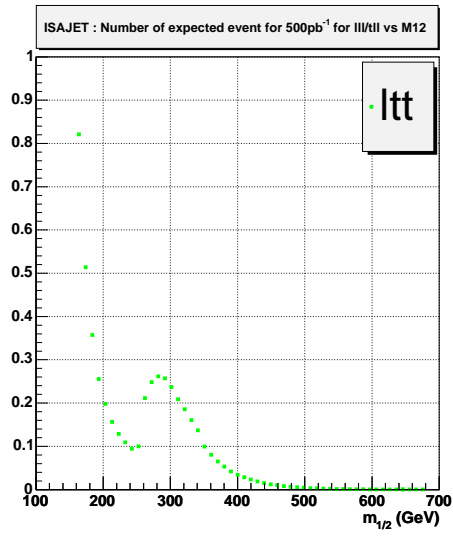


Figure 6.21. ISAJET: Number of generated lepton-ditau events  $\sqrt{s} = 2$  GeV for 500 pb<sup>-1</sup>



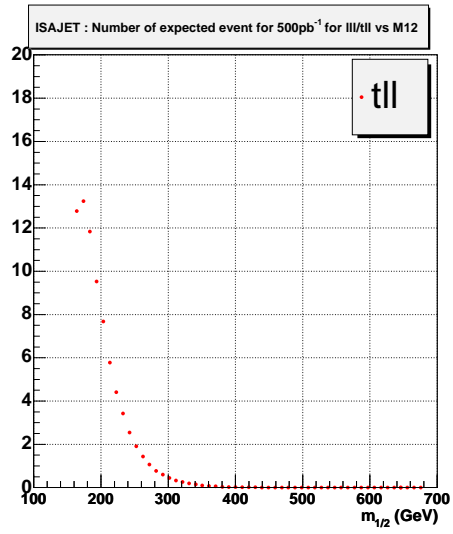


Figure 6.22. ISAJET: Number of generated dilepton-tau events  $\sqrt{s} = 2$  Gev for 500 pb<sup>-1</sup>

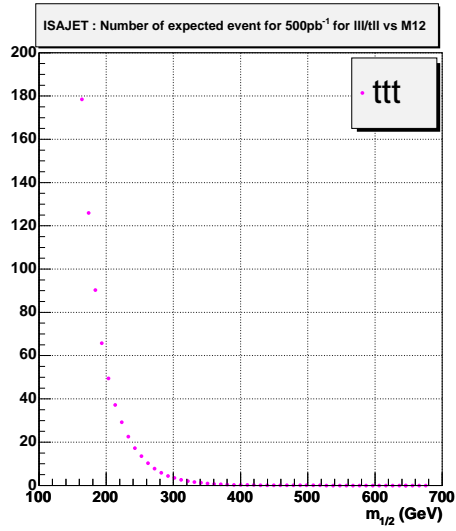


Figure 6.23. ISAJET: Number of generated tritau events  $\sqrt{s} = 2$  Gev for 500 pb<sup>-1</sup>



## 7. Trilepton Sensitivity at Tevatron Run II

The assessment of the Tevatron Run II sensitivity for supersymmetric matter is presented in the context of mSUGRA, by the evaluation of the trilepton rate, extended to the  $\tau$  signal. Aside from the increase of the mass range that may be investigated, the new large data sample should make it possible to search for processes with small cross sections; indeed, the associated production of chargino-neutralino with fully leptonic decay may provide a good signal at high  $m_0$  and  $m_{\frac{1}{2}} \simeq 220$  GeV. The regions of the parameter space characterized by best sensitivity are then compared to the values preferred by the low energy constraints and the new WMAP data [18].

### 7.1 Low energy constraints

Even though detection of any signal providing evidence for new physics could also be associated to models different from SUSY, still several low energy measurements have been adopted to indicate the preferred values of the mSUGRA parameters. Experimental checks for mSUGRA are provided by the decay rate of  $b \rightarrow s\gamma$ , the value of the anomalous magnetic moment of the muon  $a_\mu$ , the  $B_S \rightarrow \mu^+\mu^-$  branching ratio and the density of cold dark matter in the universe.

- $b \rightarrow s\gamma$  Branching Ratio.

The branching ratio, measured by BELL, CLEO and ALEPH is given by  $(3.25 \pm 0.37) \times 10^{-4}$  [3], corresponding to  $2.16 \times 10^{-4} < BR < 4.34 \times 10^{-4}$  at 95 % C.L whereas the SM prediction is  $(3.38 \pm 0.33) \times 10^{-4}$  [19]. In a SUSY framework, Higgs-top loops and chargino-*squark* terms could modify the SM value. In Fig. 7.4 and Fig. 7.5, contours of BR of  $2, 3, 4$  and  $5 \times 10^{-4}$  are shown for different set of parameters.

- Muon anomalous magnetic moment  $a_\mu$ .

The muon anomalous magnetic moment have been measured at the E821 experiment [20]:  $a_\mu = 11659204(7)(5) \times 10^{-10}$ . SUSY contributions, namely chargino-*sneutrino* and neutralino-*smuon* loops, may affect the SM value:  $a_\mu = 11659159 \pm 6.7 \times 10^{-10}$  [19].

- $B_S \rightarrow \mu^+ \mu^-$  Branching ratio.

The upper limit on  $B_S \rightarrow \mu^+ \mu^-$  branching ratio, as measured at CDF [21], is  $\text{BR}(B_S \rightarrow \mu^+ \mu^-) < 2.6 \times 10^{-6}$  whereas the SM prediction is  $\text{BR}(B_S \rightarrow \mu^+ \mu^-) \sim 3.4 \times 10^{-9}$ . In a SUSY context, the BR increases thanks to the amplitude of the Higgs mediated decay.

- Measured value of the cold dark matter density  $\Omega_{CDM} h^2$ .

The LSP, namely the lightest neutralino in the mSUGRA scenario, has to be regarded as a suitable candidate for the non baryonic cold dark matter of the universe; within this assumption, the latest results from the WMAP satellite are a new and crucial constraints on the  $\tilde{\chi}_1^0$  mass range. WMAP quotes a density of cold dark matter  $\Omega_{CDM} h^2 = 0.1126_{-0.0181}^{+0.0161}$ . From this, an upper limit on the  $\tilde{\chi}_1^0$  mass can be inferred:  $m_{\tilde{\chi}_1^0} \simeq 400 - 500$  GeV for  $\tan\beta \simeq 45$  and  $\mu > 0$ , corresponding to  $m_{\frac{1}{2}} \simeq 900-1200$  GeV. Aside from providing a mass range that improves the prospects of discovery at hadron colliders, the new measurements suggest also regions of the parameter space which are favoured and where the future searches should focus [1].

## 7.2 Collider phenomenology

Search for supersymmetric matter is one of the major goal of the current and future runs at the HEP experiments. As study of the parameter space within the mSUGRA scenario is given here with the aim of assessing the sensitivity at Tevatron Run II. This analysis is performed mainly *via* the clean trilepton channel associated to the chargino-neutralino production with a fully leptonic decay, extended to *tau*

events. The results are presented in the  $m_0$ - $m_{\frac{1}{2}}$  plane, being the SUSY masses mainly dependent on these two parameters, for various choices of the other parameters:

- $m_0$  in  $[0,1000]$  GeV ( $\Delta = 20$  GeV)
- $m_{\frac{1}{2}}$  in  $[100,1000]$  GeV ( $\Delta = 20$  GeV)
- $\tan\beta$  in  $[2,50]$  ( $\tan\beta=2,5,10,20,30,40,50$ )
- $A_0$  in  $[0,250]$  ( $A_0=0,20,50,100,150,200,250$ )
- $\mu > 0$

Regardless of the channel under investigation, the maximum sensitivity in  $m_0$  is reached for  $m_{\frac{1}{2}} < 250$  GeV since the production cross section  $\sigma_{\tilde{\chi}_1^\pm \tilde{\chi}_2^0}$  decreases with  $m_{\frac{1}{2}}$ , which is, in turn, proportional to the chargino and neutralino mass.

In particular, the trilepton ( $e,\mu$ ) rate changes with  $\tan\beta$  for a given value of the trilinear coupling  $A_0$ : at low  $m_0$  and low  $m_{\frac{1}{2}}$ , in the so called 'bulk' region, the effective cross section decreases with  $\tan\beta$  whereas the tail at high  $m_0$  and low  $m_{\frac{1}{2}}$  slightly increases in size and its maximum occurs at lower  $m_0$ . Moreover, the signal region at high  $m_0$  becomes wider with respect to  $m_{\frac{1}{2}}$  (Fig. 7.1 and Fig. 7.2). The suppression of sensitivity at low  $m_0$  for high value of  $\tan\beta$  is due to the decay of  $\tilde{\chi}_1^\pm$  into  $\tilde{\tau}_1 \nu_\tau$  which dominates over the  $\tilde{\chi}_1^0 W$  mode likewise  $\tilde{\chi}_2^0$  into  $\tilde{\tau}_1 \tau$  is preferred rather than  $\tilde{\chi}_1^0 h$  or  $\tilde{\chi}_1^0 Z$ . The branching ratio into third generation *sfermions* is indeed enhanced at the expense of the first and second generation. However, as  $m_0$  increases, *stau* mass increases and the corresponding decay mode is reduced.

For low  $\tan\beta$ , all signals but the tritau one increase with  $A_0$ , whereas for  $\tan\beta > 30$  the lepton decay modes are almost completely suppressed and the  $\tau$  signal dominates when  $A_0$  becomes larger, as expected. A sample set of results is presented in the appendices.

The results of the scan are now compared to the constraints with the aim of determining the mSUGRA parameter space region consistent with the laboratory measurements and the newest dark matter density data. Fig. 7.4 and Fig. 7.5

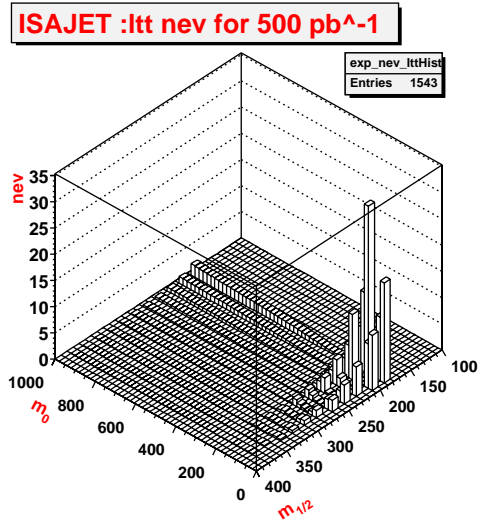
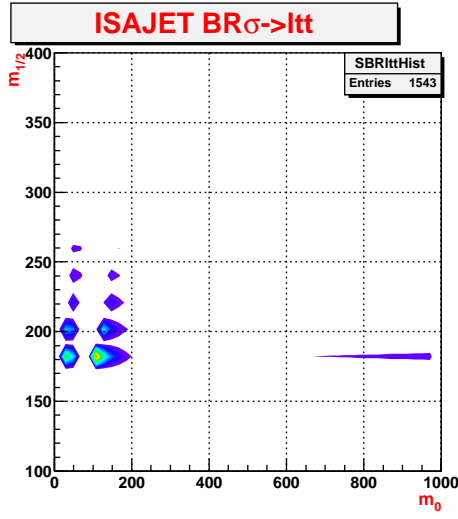
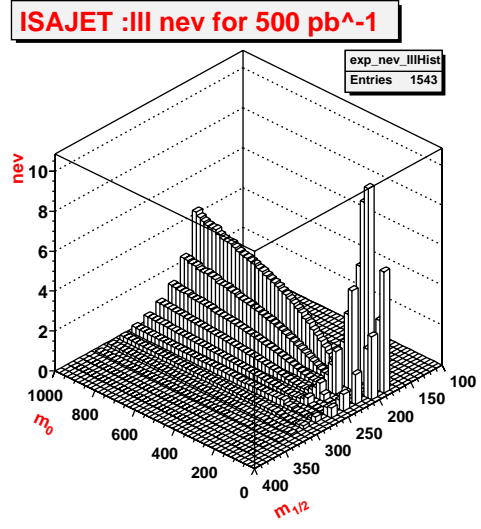
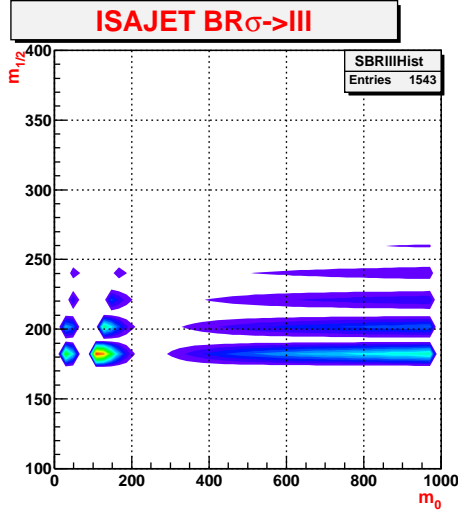


Figure 7.1.  $A_0 = 0$ ,  $\mu > 0$ ,  $\tan\beta = 10$

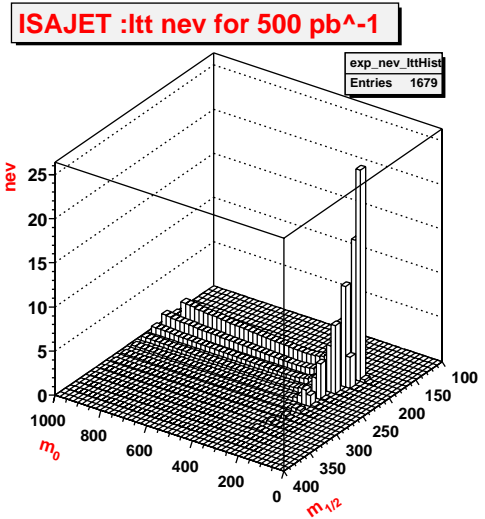
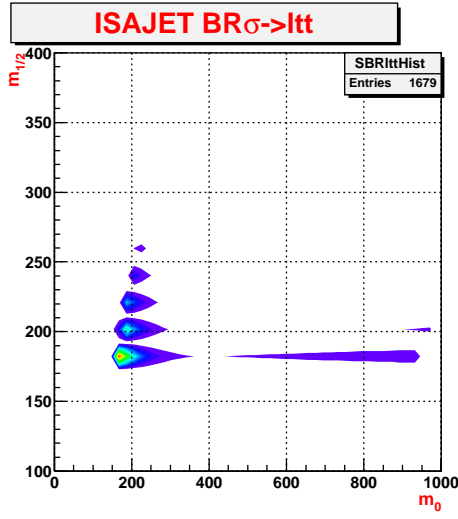
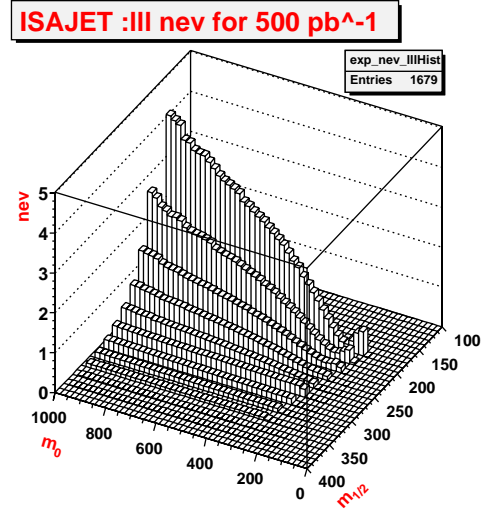
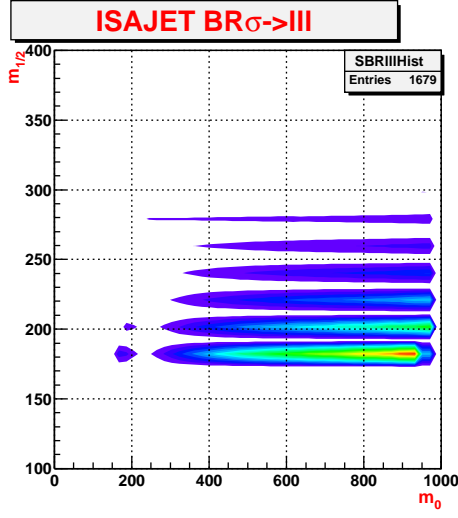


Figure 7.2.  $A_0 = 0$ ,  $\mu > 0$ ,  $\tan\beta = 30$

display the allowed regions for  $\tan\beta=10$  and  $\tan\beta=30$  at  $A_0=0$  and  $\mu > 0$  [3]. As mentioned in Sec. 5.1, the red shaded regions are excluded because the REWSB does not occur (right side) or because the lightest *stau* is the LSP (left side); the magenta region is excluded by search for chargino and *sleptons* at LEP2. The red contour is the border for the region excluded by Higgs search. As far as the  $B_S$  decay rate is concerned, the constraint has no effect at low  $\tan\beta$  whereas it might become crucial as  $\tan\beta$  increases. However, the BR is always below  $10^{-7}$  and could not be detected at the Tevatron Run II. On the other hand, the whole  $m_0$ - $m_{\frac{1}{2}}$  plane satisfies the value of  $b \rightarrow s\gamma$  branching fraction at low  $\tan\beta$  (blue lines), whereas much of the region with  $m_{\frac{1}{2}} < 400$  GeV is disfavoured at high  $\tan\beta$ , being the BR below  $2 \times 10^{-4}$ . The new cosmological constraint is shown in Fig. 7.3 which displays the strips of the  $m_0$ - $m_{\frac{1}{2}}$  plane allowed by measured value of cold dark matter density [1]<sup>1</sup>.

In order to set a limit at 95% C.L (Feldman and Cousins table), at least 7 SUSY events are needed with a background  $\simeq 8$  events from  $WW$ ,  $WZ$  and  $ZZ$  [22]. Under this assumption, the sensitivity predictions are compared to the constraints and the first conclusions are drawn: the 'bulk' region where the trilepton channel shows the highest sensitivity has already been excluded by LEP2 measurements. However, as mentioned earlier, the exclusion limits in the  $m_0$ - $m_{\frac{1}{2}}$  plane are model dependent and have to be regarded only as determining disfavoured regions; for this reason, a point sitting in the excluded region might correspond to an un-excluded mass range and therefore must be investigated. This is the case of the parameter point  $A_0=0$ ,  $\tan\beta=10$ ,  $m_0=120$  GeV and  $m_{\frac{1}{2}}=200$  GeV (Fig. 7.1) which corresponds to an allowed mass range and where 4 pure trilepton events are expected (the number of expected events is the number of events at generation level). This sample point highlights a feature of the trilepton signal: over most of the parameter space it is severely rate limited and a luminosity greater than  $500 \text{ pb}^{-1}$  is needed for setting a limit at 95 %. For the point mentioned above, an integrated luminosity of  $\sim 2$

---

<sup>1</sup>The strips are the preferred values of the parameters  $m_{\frac{1}{2}}, m_0$  with  $\tan\beta$  in  $[5, 55]$ : since  $\Delta(\tan\beta) = 5$ , any intermediate point in the plane would be compatible with some intermediate value of  $\tan\beta$ .



$\text{fb}^{-1}$  is required: actually, this is the base goal of Run II at the Tevatron collider. The parameter area where the tail is located, high  $m_0$  and  $m_{\frac{1}{2}} > 150$  GeV, merits further investigation. In particular, for  $A_0=0$  and  $\tan\beta=10$ ,  $\simeq 7$  chargino-neutralino trilepton events are expected at  $m_0 > 880$  GeV and  $m_{\frac{1}{2}} = 220$  GeV for a luminosity of  $2.4 \text{ fb}^{-1}$ . This region is preferred by the low energy constraint  $b \rightarrow s\gamma$  BR and the value of  $\delta a_\mu$  is in the range  $10 - 40 \times 10^{-10}$  which agrees with the E821 measurements. When the cosmological constraint is imposed, these results are also compatible to the WMAP data: the range under investigation belongs to the strips favoured by the new limits of cold dark matter density. This area of the parameter space hasn't been explored by LEP2 and it is observable at the Tevatron Run II. As a further step towards the evaluation of the reach at the Tevatron, the SM background has to be taken into account using montecarlo simulation methods. SM events must

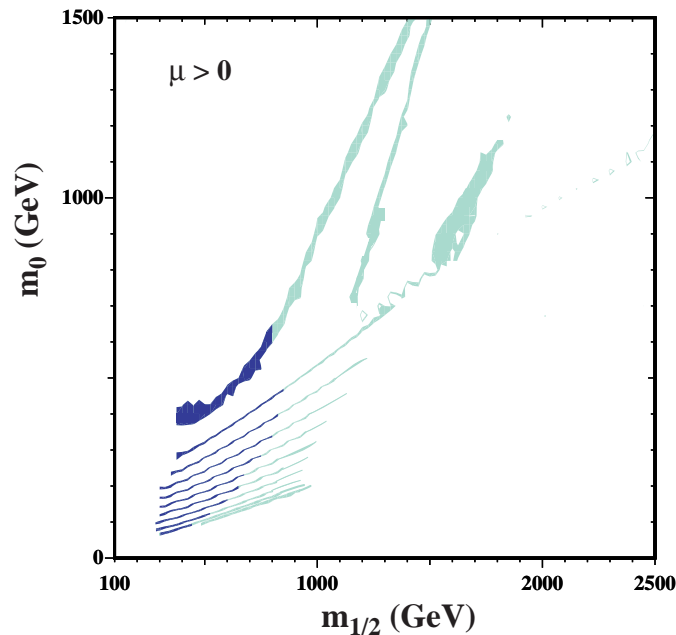


Figure 7.3. J.Ellis *et al.*, hep-ph/0303043; The strips display the regions of the  $m_0$ - $m_{\frac{1}{2}}$  plane that are compatible with the  $0.094 < \Omega_\chi h^2 < 0.129$  and the laboratory constraints for  $\mu > 0$  and different values of  $\tan\beta$

be simulated through the detector to determine the trigger requirements and the detector acceptance.

For low values of  $\tan\beta$ , the  $\tau$  signature does not differ substantially from the

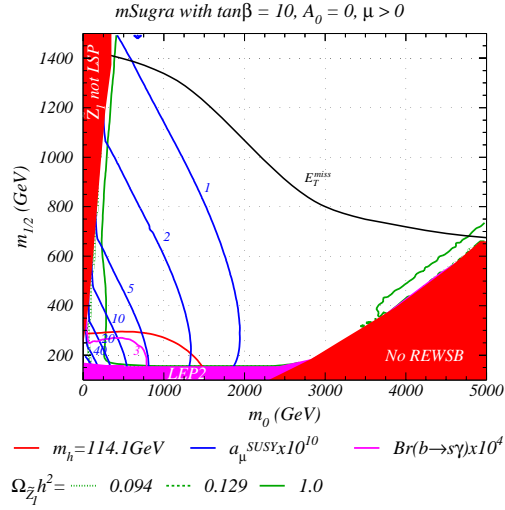


Figure 7.4. H.Baer *et al.*, hep-ph/0304303; reach of LHC assuming 100  $\text{fb}^{-1}$  of integrated luminosity and excluded regions

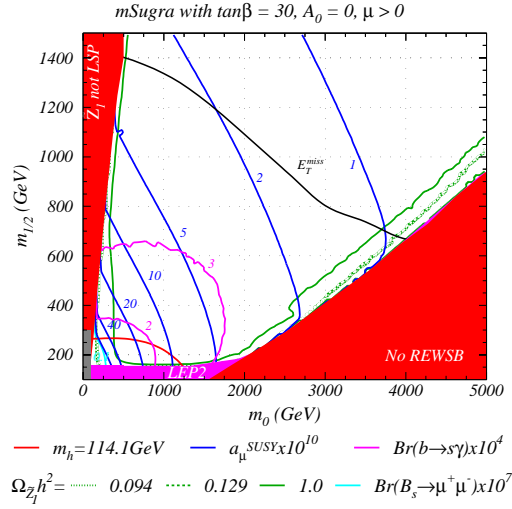


Figure 7.5. H.Baer *et al.*, hep-ph/0304303; reach of LHC assuming 100  $\text{fb}^{-1}$  of integrated luminosity and excluded regions

leptonic one, actually 12 ditau events are expected for  $m_0=120$  GeV and  $m_{\frac{1}{2}}=200$  GeV whereas the dilepton signal reaches 9 events at  $m_0=80$  GeV and  $m_{\frac{1}{2}}=200$  GeV. The tritau decay mode is dominant in the region  $m_0 > 80$   $m_{\frac{1}{2}} > 200$  GeV yielding 10-50 events. Notice that, for low value of both  $\tan\beta$  and  $A_0$  the trilepton signal should be larger than the dilepton one while the tritau dominates the ditau on the basis of simple combinatorial. As  $\tan\beta$  becomes larger than 20, the fully leptonic signal is suppressed whereas the size of the ditau and tritau signals increase due to  $\tan\beta$  dependancy of the third generation mass; however, the region excluded by the  $b \rightarrow s\gamma$  constraint extends correspondingly. Therefore, in order to fully exploit the increase in signal, a medium value of  $\tan\beta$ , for example  $\tan\beta=30$ , has to be investigated. From the results presented in Fig. 7.6, it is clear that the presence of  $\tau$  in the SUSY event leads to an enhancement in comparison to the clean trilepton events. So far, Run I searches for SUSY have been mainly performed in channels involving leptons, photons and  $\cancel{E}_T$  due to a low  $\tau$  efficiency; nevertheless, at Run II, the detection efficiency is expected to improve so that the tritau signature won't be severely efficiency limited. This event topology differs from the trilepton one and a detailed analysis of both background and efficiency is needed to understand the feasibility of the analysis. This study is performed elsewhere [19]. On the other hand, the tau-dilepton channel may be regarded as the best compromise between expected number of events and detection efficiency. Actually, the behavior of the sensitivity is almost the same as the trilepton events in that the high rate regions are found in the same range of the mSUGRA parameters; but the signal size is similar to the more experimentally challenging tritau events since the rate is dominated by the neutralino decay rather than the lepton decays.

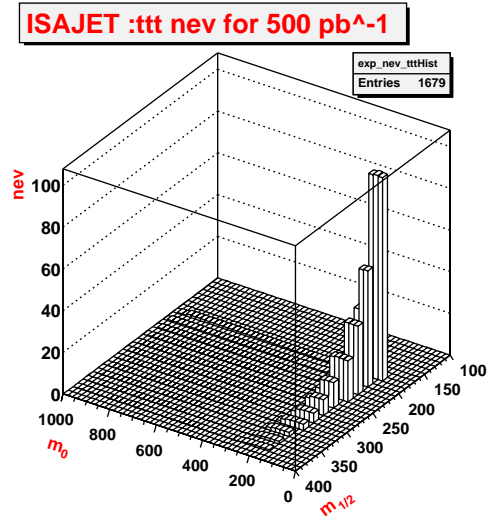
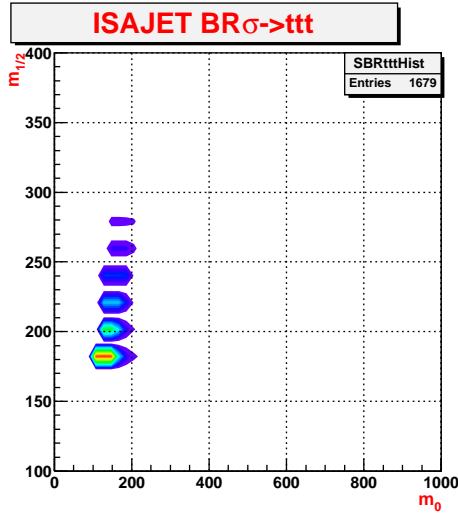
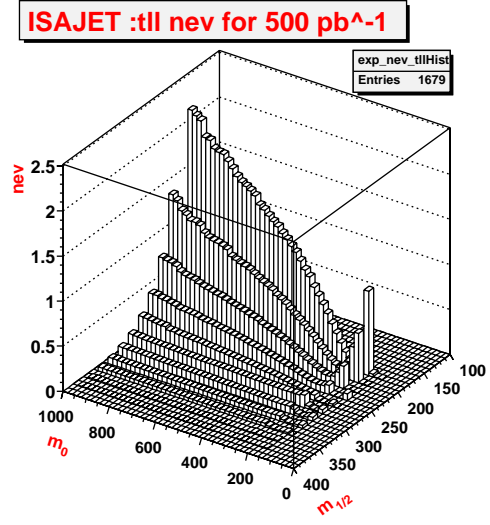
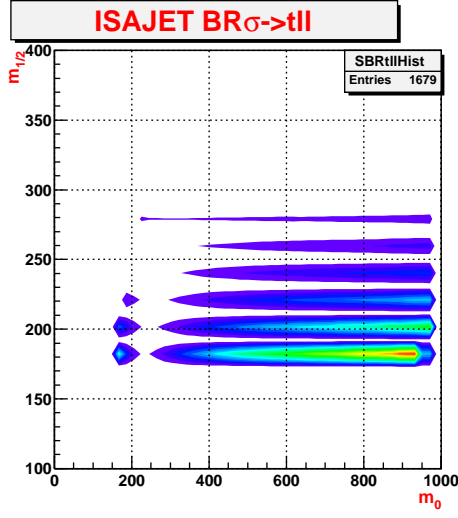


Figure 7.6.  $A_0 = 0$ ,  $\mu > 0$ ,  $\tan\beta = 30$

## 8. Conclusion

The classic signature for SUSY at hadron collider is the 'jet clean' trilepton channel associated to the chargino-neutralino production: this channel has been investigated to assess the sensitivity at the current Run II of the Tevatron in the context of mSUGRA. In the mSUGRA model, a universal scalar mass  $m_0$ , a unified gaugino mass,  $m_{\frac{1}{2}}$ , and a unified coupling  $A_0$  are assumed; aside for these parameters, the theory is determined also by the higgsino term  $\mu$  (which mainly weighs the higgsino component and the gaugino component of chargino and neutralino) and the ratio of the Higgs expectation values,  $\tan\beta$ . From a detailed scan of the parameter space, we determine that the sensitivity is mainly affected by the the two mass parameters and by  $\tan\beta$ , which dramatically affects the spectrum of the third generation *sfermion*, whereas it turns out to be almost insensitive to  $A_0$ . To summarize the results extensively shown in the appendices, the region at  $m_{\frac{1}{2}} \simeq 220$  GeV and high  $m_0$ , can be regarded as the most promising area of the parameter space being beyond the reach of LEP2 and in agreement with the low energy constraints. This set of parameters is also favoured by the new data concerning the density of cold dark matter in the universe collected by the WMAP satellite. However, in the region that have been mapped out, the trilepton channel is severely rate limited; on the other hand the dilepton-tau channel rate is dramatically enhanced thanks to the  $\tan\beta$  dependency of the third generation mass. We have to further study the background and efficiency to determine which experimental signature to exploit the full potential of the data collected by the CDF experiment.



## 9. AppendixA

### 9.1 Scan: $A_0=0$ $\mu > 0$

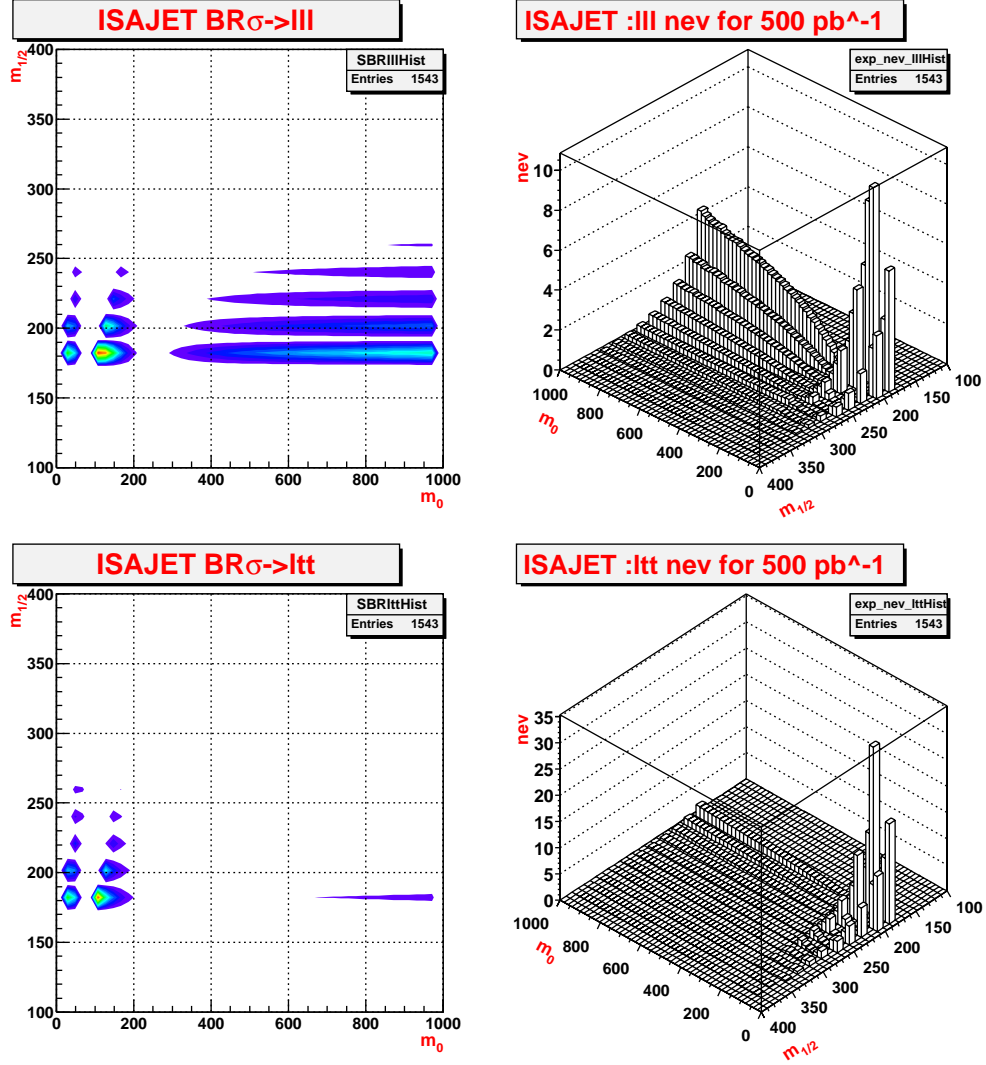


Figure 9.1.  $A_0=0$ ,  $\mu > 0$ ,  $\tan\beta=10$

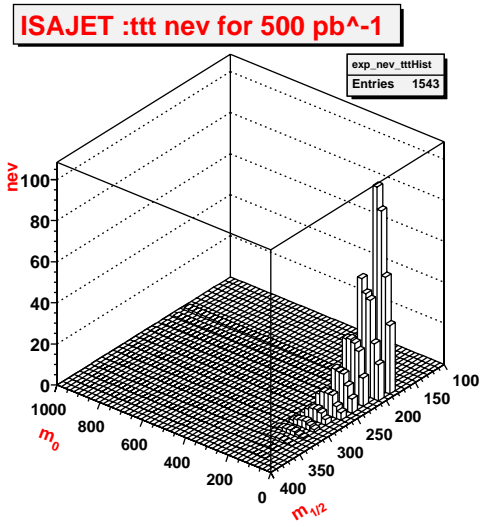
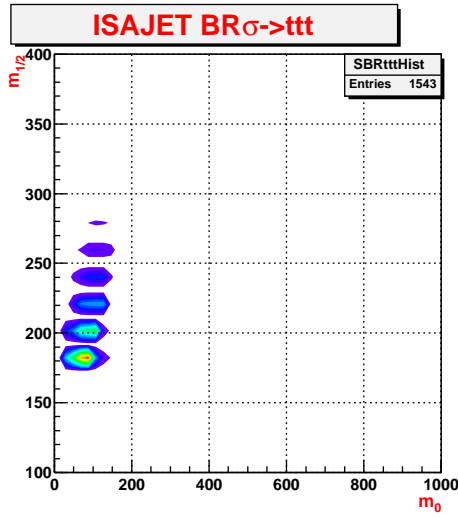
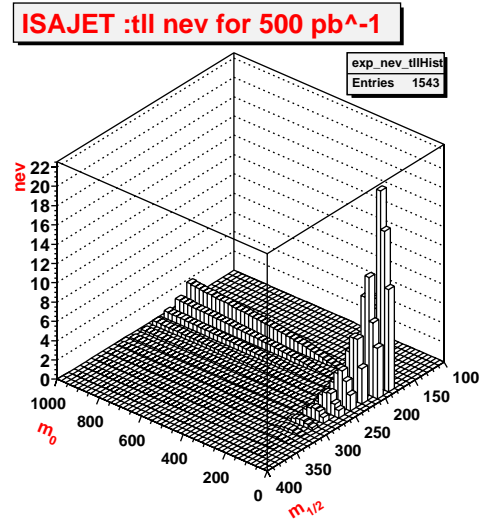
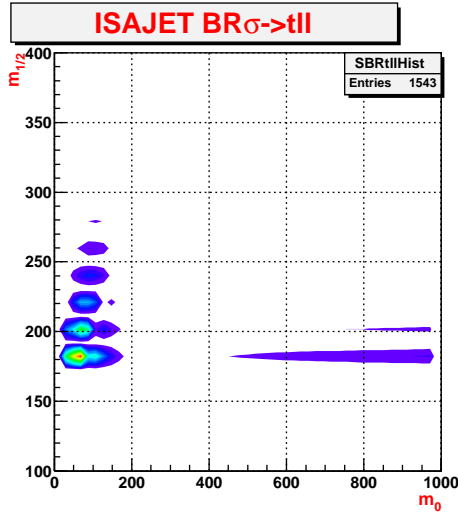


Figure 9.2.  $A_0 = 0$ ,  $\mu > 0$ ,  $\tan\beta = 10$



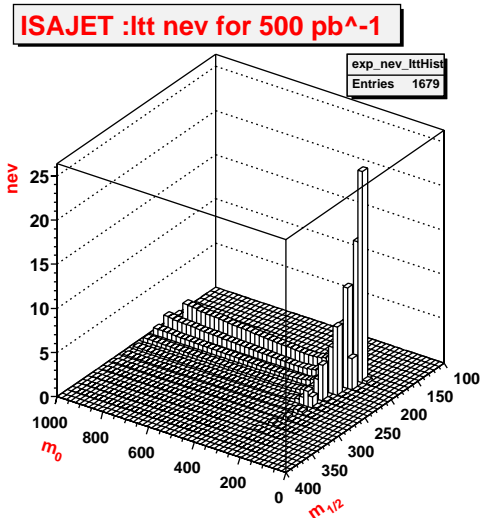
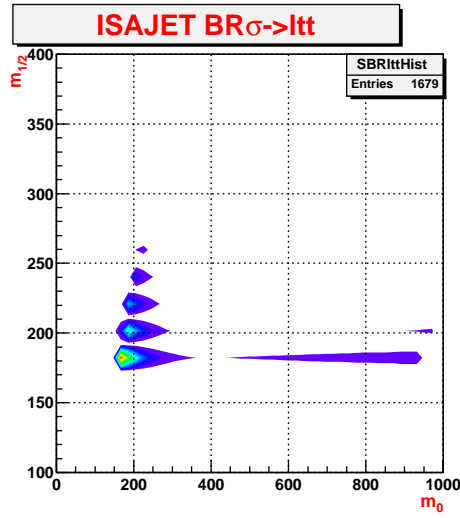
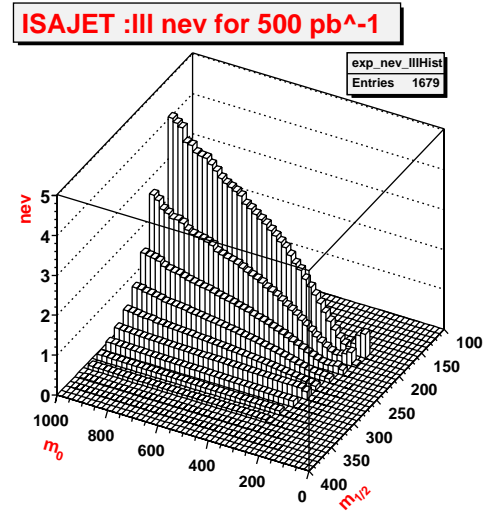
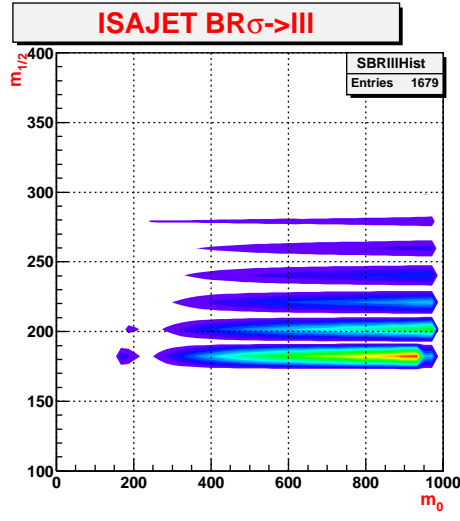


Figure 9.3.  $A_0 = 0$ ,  $\mu > 0$ ,  $\tan\beta = 30$

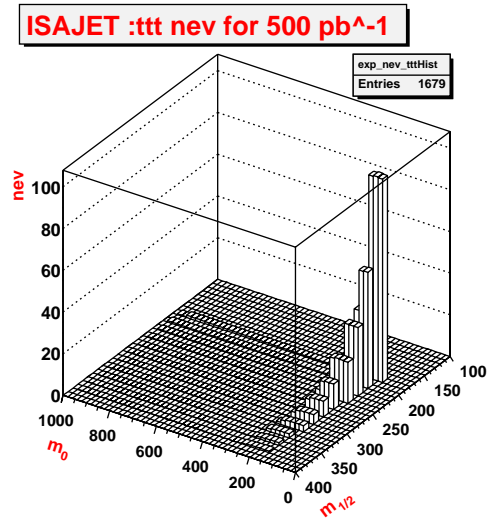
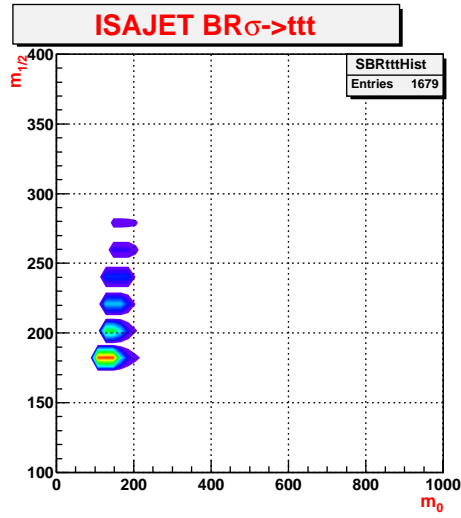
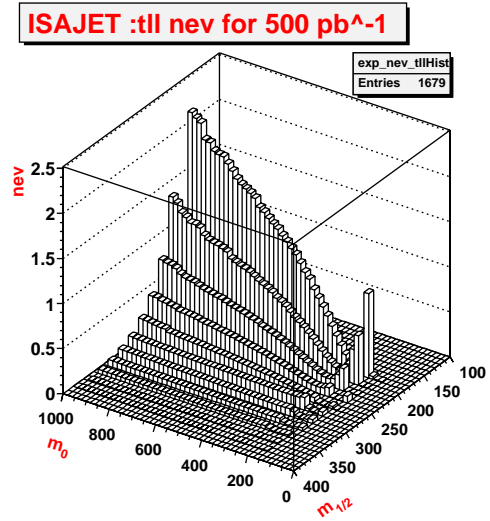
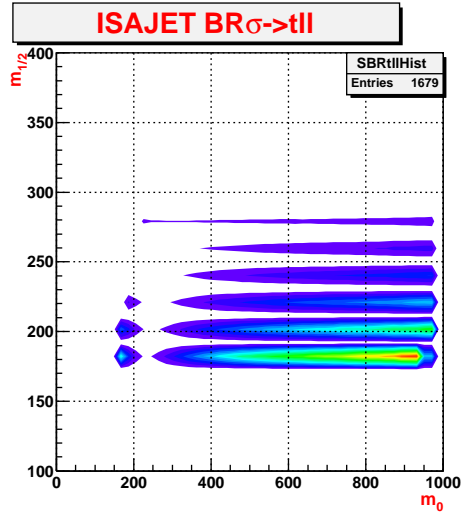


Figure 9.4.  $A_0 = 0$ ,  $\mu > 0$ ,  $\tan\beta = 30$

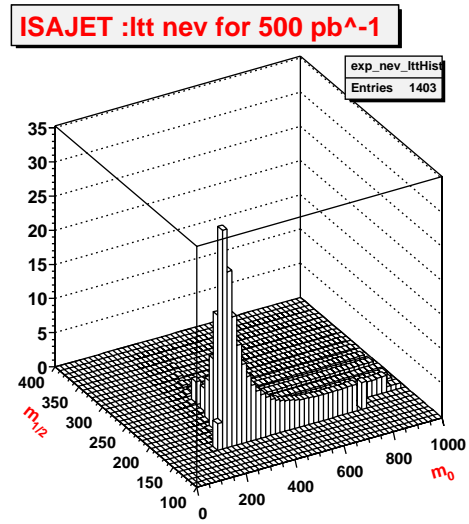
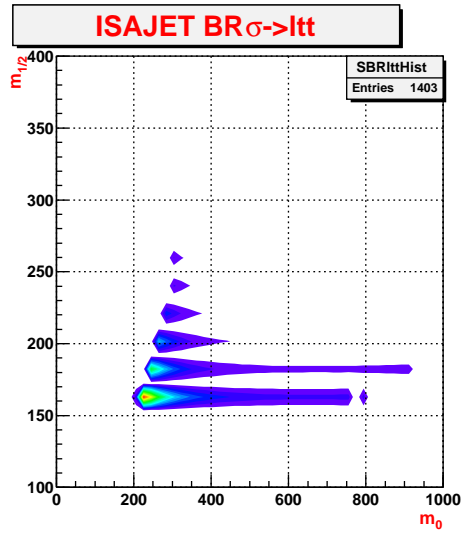
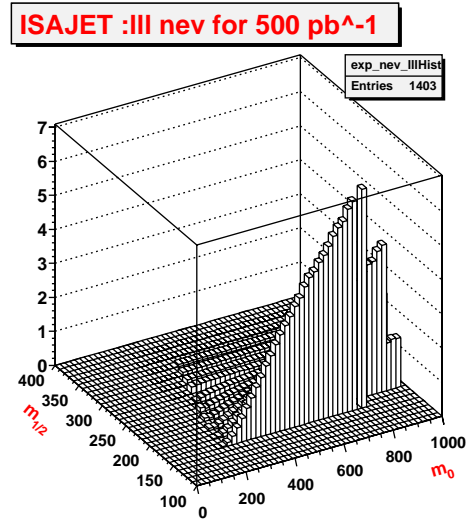
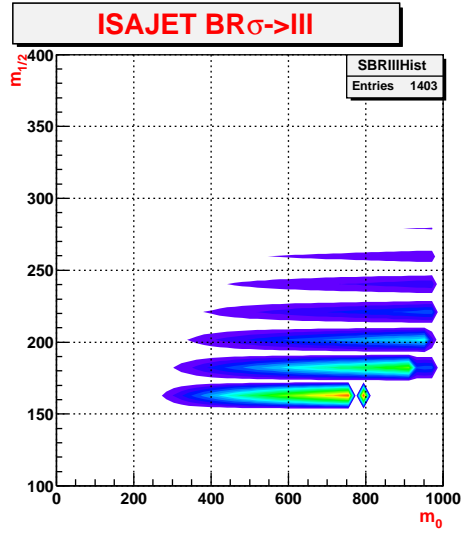


Figure 9.5.  $A_0 = 0$ ,  $\mu > 0$ ,  $\tan\beta = 50$

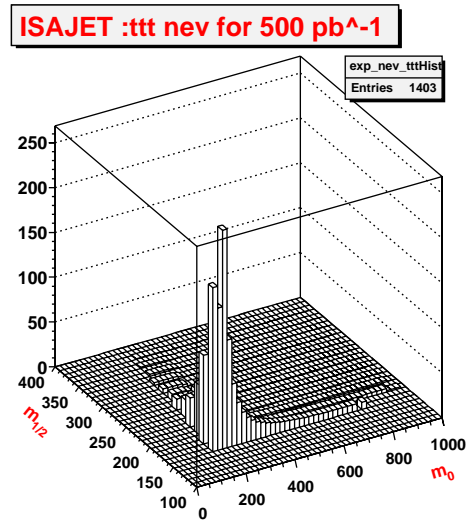
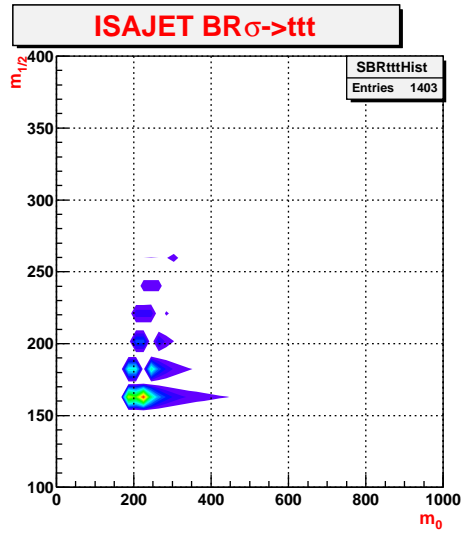
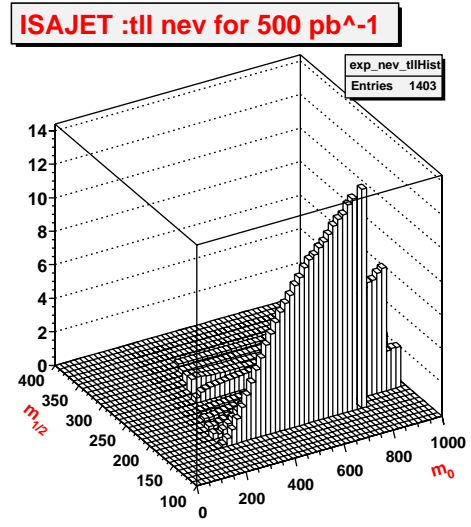
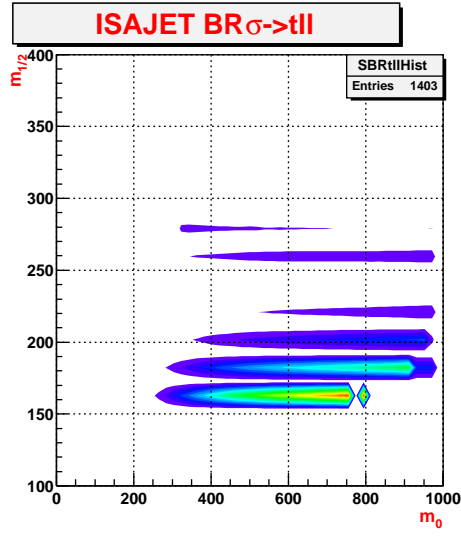


Figure 9.6.  $A_0 = 0$ ,  $\mu > 0$ ,  $\tan\beta = 50$

## 10. AppendixB

### 10.1 Scan: $A_0=250$ $\mu > 0$

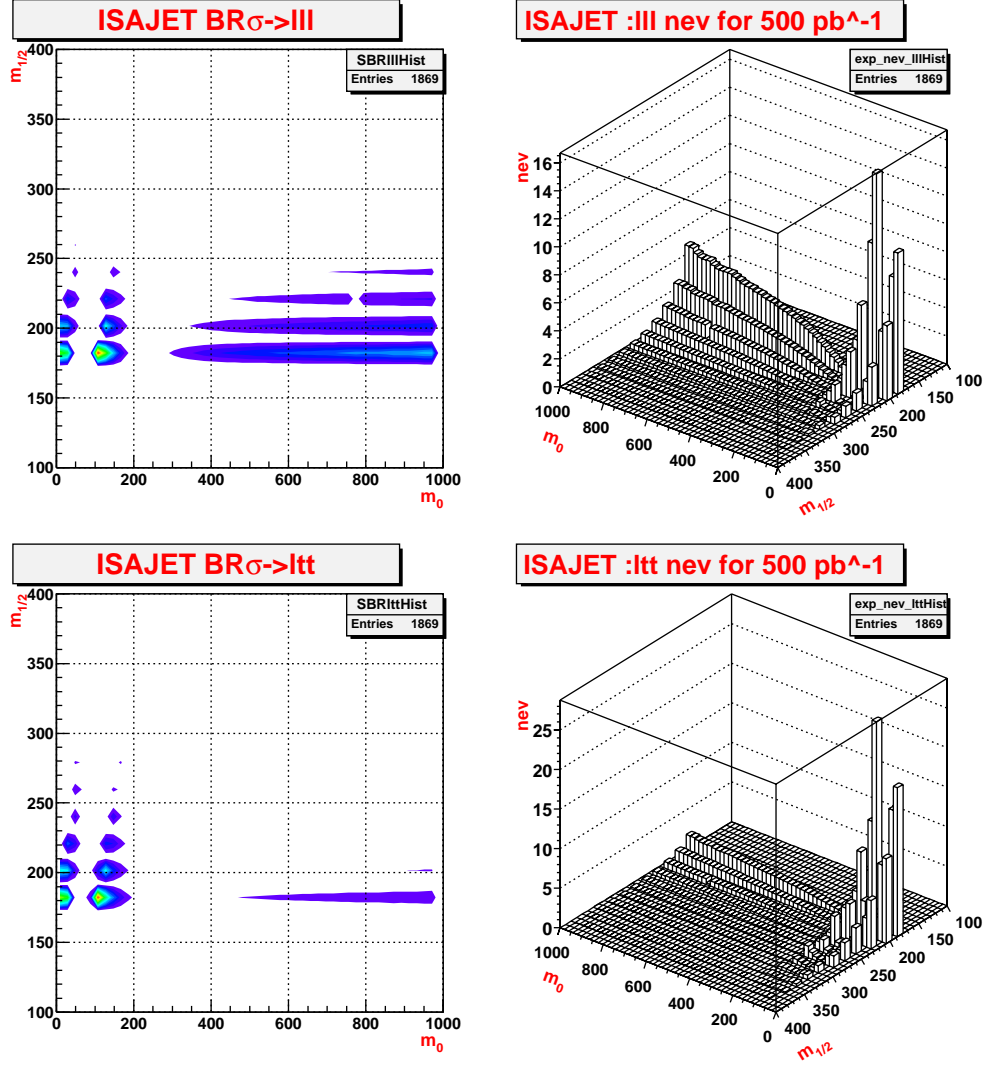


Figure 10.1.  $A_0=20$ ,  $\mu > 0$ ,  $\tan\beta=10$

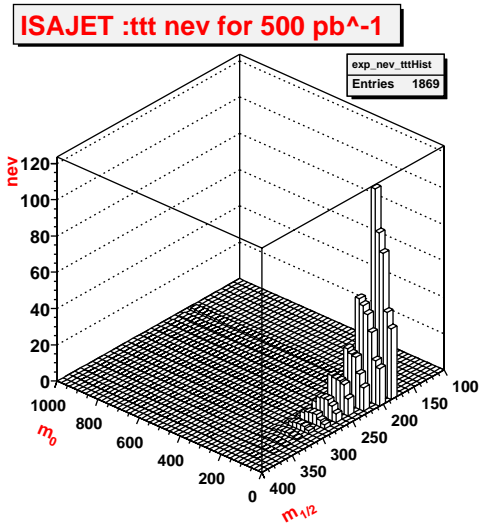
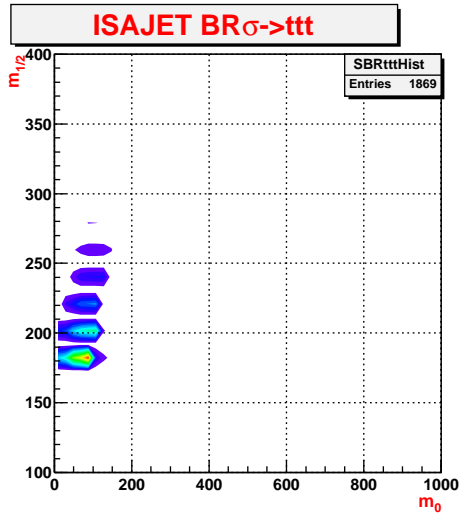
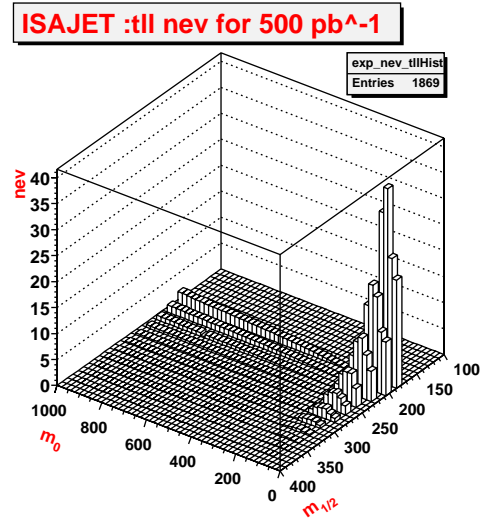
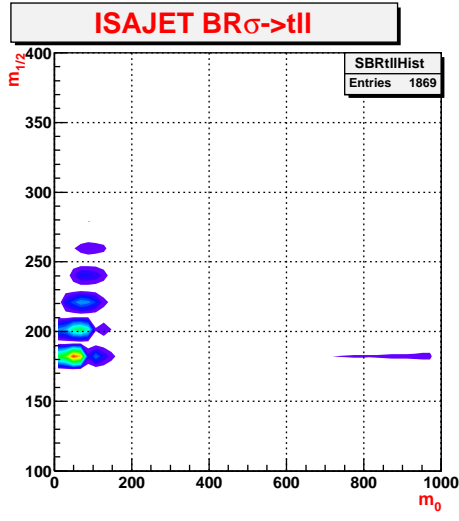


Figure 10.2.  $A_0=20$ ,  $\mu > 0$ ,  $\tan\beta=10$

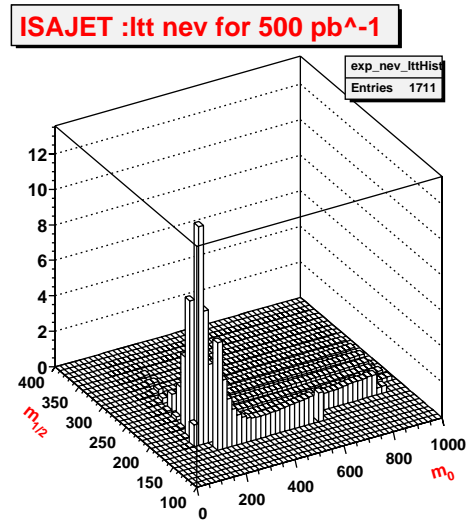
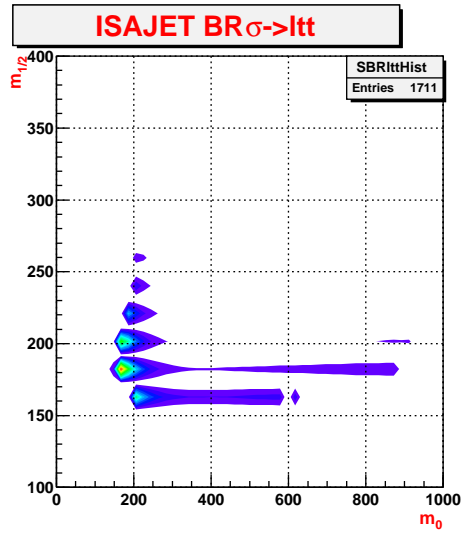
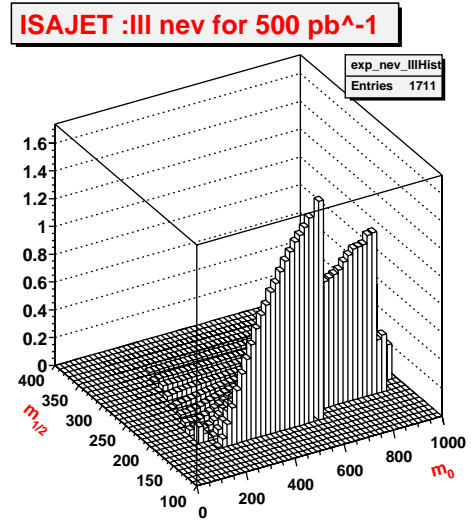
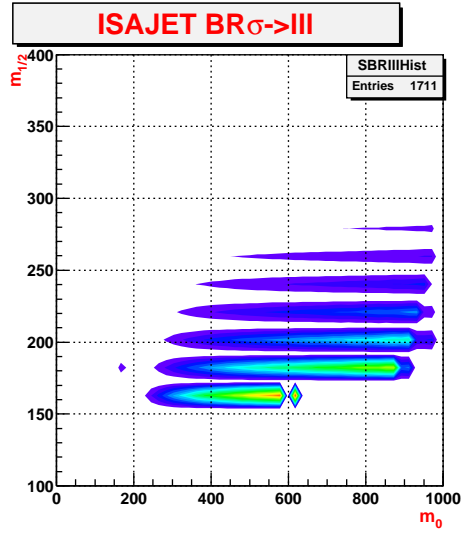


Figure 10.3.  $A_0 = 20$ ,  $\mu > 0$ ,  $\tan\beta = 30$

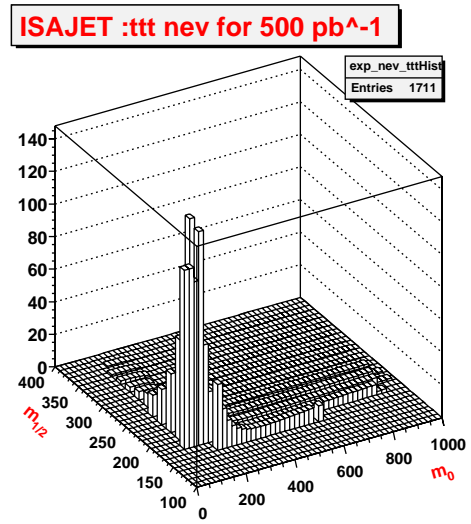
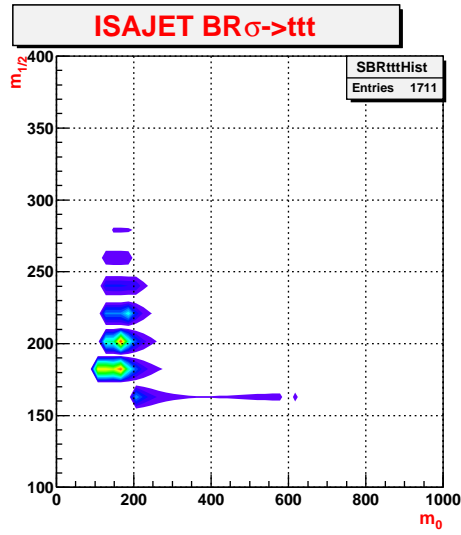
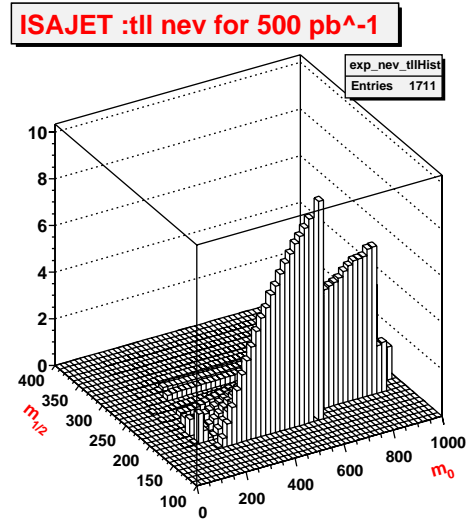
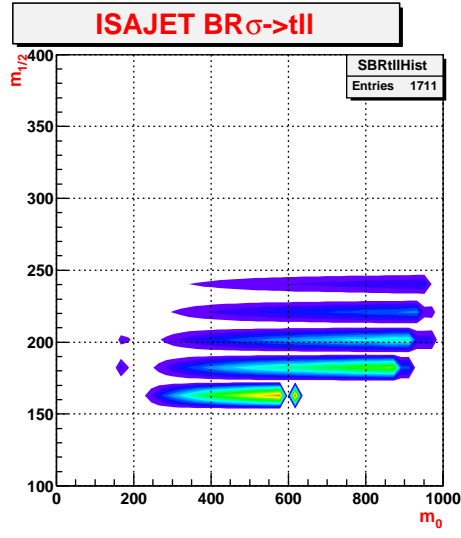


Figure 10.4.  $A_0 = 20$ ,  $\mu > 0$ ,  $\tan\beta = 30$



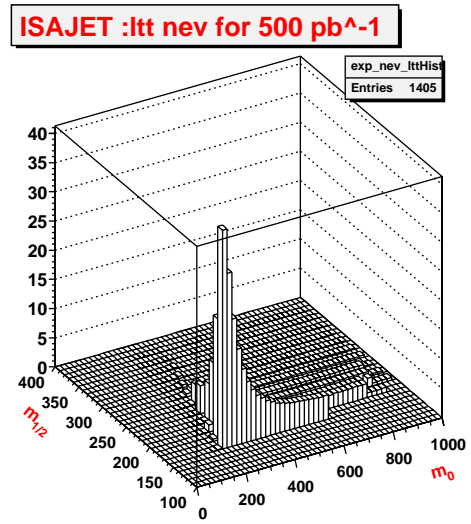
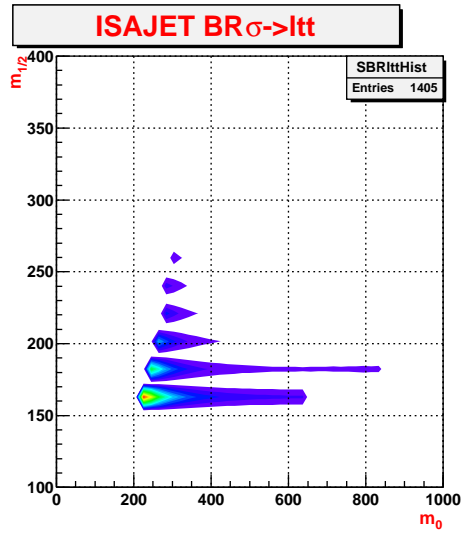
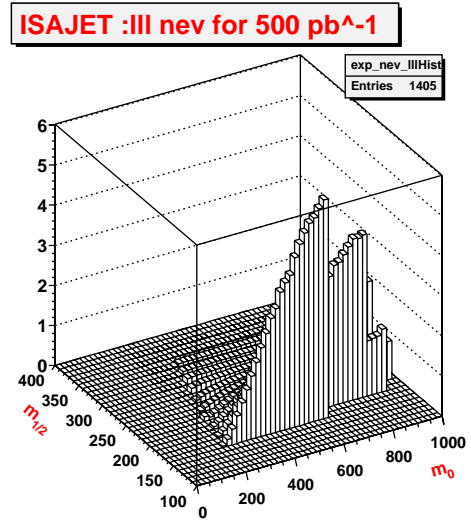
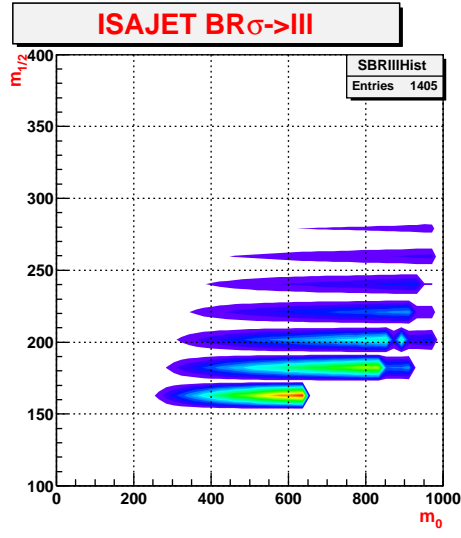


Figure 10.5.  $A_0 = 20$ ,  $\mu > 0$ ,  $\tan\beta = 50$

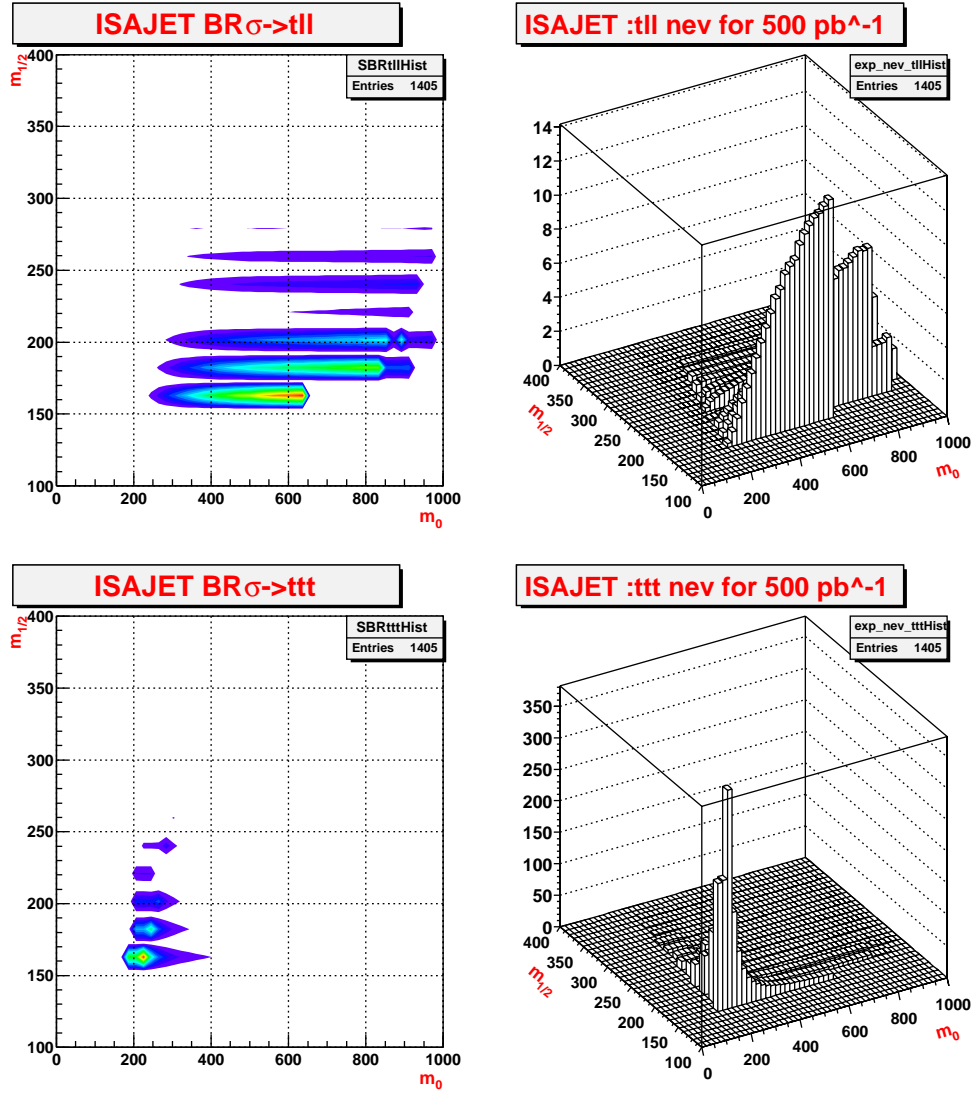


Figure 10.6.  $A_0 = 20$ ,  $\mu > 0$ ,  $\tan\beta = 50$

## LIST OF REFERENCES

- [1] J. Ellis and other. Supersymmetric dark matter in light of wmap. *hep-ph/0303043*, 2003.
- [2] M. Peskin. Beyond the standard model. *hep-ph/9705479*, 2002.
- [3] H.Baer et al. Updated reach of cern lhc and constraints from relic density,  $b \rightarrow s\gamma$  and  $a_\mu$  in the msugra model. *hep-ph/0304303*, 2003.
- [4] J. Ellis. Beyond the standard model for hillwalkers. *hep-ph/9812235*, 1998.
- [5] J. Ellis. Limits of the standard model. *hep-ph/0211168*, 2002.
- [6] M. Drees. An introduction to supersymmetry. *hep-ph/9611409*, 1996.
- [7] X. Tata. What is supersymmetry and how do we find it? *UH-511-872-97, hep-ph/9706307*, 1997.
- [8] H. Murayama. Supersymmetry phenomenology. *hep-ph/0002232*, 2000.
- [9] M. Carena et al. The search for supersymmetry at the tevatron collides. *hep-ph/9712022*, 2002.
- [10] S. P. Martin. A supersymmetry primer. *hep-ph/9709356*, 1997.
- [11] H.Baer et al. Relic density of neutralinos in minimal supergravity. *hep-ph/0211213*, 2002.
- [12] J.Edsjo and other. Accurate relic densities with neutralino, chargino and sfermion coannihilations in msugra. *hep-ph/0301106*, 2003.
- [13] The CDF Collaboration. The cdf ii detector. technical design report. 1996.
- [14] H. Baer and X.Tata. Probing charginos and neutralinos beyond the reach of the cern  $e^+e^-$  collider lep at the fermilab tevatron collider. *Physical Review D*, 47:2739, April 1993.
- [15] LEP-SUSY Group. Interpretation of the results in minimal sugra. *LEPSUSYWG/02-06.2*, 2002.
- [16] B.C.Allanach et al. The snowmass points and slopes: Benchmarks for susy searches. *hep-ph/0202233*, 2002.
- [17] M. Spira. Higgs and susy particle production at hadron collider. *hep-ph/0211145*, 2002.
- [18] A.B.Lahanas et al. Wmapping the universe: Supersymmetry, dark matter, dark energy, protono decay and collider physics. *hep-ph/0308251*, 2003.

- [19] S.Abel et al. Report of sugra working group for run ii of the tevatron. *hep-ph/0003154*, 2000.
- [20] G.W.Bennett et al. *Phys.Rev.Lett*, 89:101804, 2002.
- [21] F.Abe et al. *Phy. Rev*, D57:181, 1998.
- [22] D.Glenzinski et al. Results from the analysis pf the tight-tight subset of the tight lepton + isolated track sample. *CDF internal note, 6790*, 2003.